UNIVERSITAT POLITÈCNICA DE VALÈNCIA

Doctoral Thesis

Characterization of dedicated PET equipment with non-conventional geometry

Gabriel Cañizares Ledo

Under the supervision of:

Antonio J. González Martínez, PhD

Valencia, June 2022

SUMMARY

Since their introduction in the 1950-decade, tomographic images have become very valuable in the medical field helping both in diagnostics and in a variety of illnesses treatment. In the molecular imaging field, Positron Emission Tomography (PET) provides accurate information of the radio-tracers interactions with the patient tissue. Moreover, it is possible to combine this information with anatomical images provided by CT (Computed Tomography) or MR (Magnetic Resonance) scanners. With the aim to improve PET systems performance, such as the spatial resolution and the sensitivity, whole body (WB) PET scanners with large axial coverage are recently proposed. However, the system cost increases and, thus, makes difficult their installation in many hospitals or research centers. Organ-dedicated PET scanners, as an alternative to such large systems, use a lower number of detectors, so their price is considerably more economical. The goal of this kind of systems is to boost PET performance by placing the detectors as close as possible to the patient, optimizing the design for a specific organ instead of a large volume. Other advantage of these scanners is their portability. In this thesis we have worked in the design and validation of two organ-dedicated PET scanners with different geometries and technologies, as well as in a novel pre-clinical PET.

The first scanner was the result from a national project called PROSPET. A PET system was designed and optimized to image the prostate area. Notice there is a high incidence rate of prostate cancer in the male population. 17% of male population will suffer prostate cancer. For this scanner, the detector modules were composed by a monolithic LYSO scintillation block coupled to a photosensor array based on silicon photomultipliers (SiPM). The first design configuration was made by two panels. However, patient results were not satisfactory due to the lack of angular information and the poor detector time resolution. Therefore, it was rebuilt in a ring configuration with a reduced diameter in comparison with WB-PET scanners. A high sensitivity and spatial resolution were found, as well as a good image quality using phantoms.

The second PET scanner, called CardioPET, also arose from a national grant, and it was implemented to visualize the heart area when the patient is under stress condition. The two panels geometry was also implemented for this system, but using pixelated crystals, therefore improving the detector time resolution and allowing to use time of flight (TOF) reconstruction algorithms. Two panels were mounted and tested with both simulation and experimental data with good results. Furthermore, the patient motion was registered applying movement correction techniques with the help of an external optical camera device and ARUCO markers. These algorithms were tested showing a good performance.

The last device that we worked within this PhD thesis was designed to optimize the classical ring PET configuration as much as possible. To do so, the gaps between the detector modules in a small animal PET were eliminated by building a single detector with a cylindrical scintillator shape. The goal is to improve the sensitivity, given that there are no event losses in the gaps and to also boost the spatial resolution since there are not edges. Two prototypes were tested with simulations, and experimentally validated as well. The first of them was built with planar outer faces whereas the second was fully cylindrical. In both designs some effects originated from the detector curvature were observed and successfully corrected during the calibration.

RESUMEN

Desde su creación en la década de 1950, las imágenes tomográficas han resultado muy valiosas en el ámbito médico ayudando tanto en el diagnóstico como en el tratamiento de múltiples enfermedades. Dentro de la imagen molecular, los escáneres PET (Tomografía por Emisión de Positrones) generan información detallada de la interacción de los radio-trazadores con el tejido de estudio, pudiendo combinar dicha información con imagen anatómica de escáneres TC (Tomografía Computarizada) o RM (Resonancia Magnética). Con el fin de aumentar las prestaciones de estos equipos, como la sensibilidad y la resolución espacial, los PET de cuerpo completo recientemente aumentan su cobertura axial. Sin embargo, el precio de estos dispositivos se multiplica, dificultando su compra en muchos hospitales y centros de investigación. Como alternativa, los escáneres PET específicos de órganos manejan un menor número de detectores haciéndolos más económicos. El objetivo de este tipo de escáneres es mejorar el rendimiento de los dispositivos acercando los detectores al paciente lo máximo posible, optimizando su diseño para un órgano en específico. Otra ventaja es la posible portabilidad de los aparatos. En esta tesis introducimos dos posibles diseños de PET específicos orientados a distintos órganos y con diferente tecnología y geometría y además un escáner preclínico con una geometría novedosa.

El primer escáner fue construido de un proyecto nacional llamado PROSPET, fue diseñado y optimizado para hacer imagen de la próstata, debido a la conocida elevada tasa de cáncer de próstata en hombres. El 17% de la población masculina sufrirá cáncer de próstata. El detector escogido para este diseño está compuesto por cristales centelladores monolíticos acoplados a una matriz de fotomultiplicadores de silicio. Inicialmente se pensó en crear un escáner compuesto por dos palas. Sin embargo, los resultados con pacientes no fueron satisfactorios debido a la falta de información angular y la ausencia de información temporal precisa en los detectores. Por tanto, se construyó una configuración de anillo con un diámetro reducido en comparación con escáneres de cuerpo completo. Se apreció un aumento en la sensibilidad y la resolución espacial, así como una buena calidad de imagen utilizando fantomas.

El segundo escáner, llamado proyecto CardioPET, está orientado a visualizar el corazón cuando el paciente está sometido a condiciones de estrés farmacológico. Para este dispositivo se utilizó el diseño de dos palas, pero usando cristales pixelados, mejorando la resolución temporal, permitiendo implantar algoritmos de tiempo de vuelo. Se han montado y testeado dos palas tanto con simulaciones como experimentalmente con buenas prestaciones. Además, se procedió a registrar el movimiento de las fuentes de radiación con el fin de aplicar

correcciones de movimiento con la ayuda de una cámara externa y unos marcadores ARUCO. Los algoritmos de corrección de movimiento fueron testeados, demostrando un buen funcionamiento.

El último dispositivo fue diseñado para optimizar la configuración PET de anillo lo máximo posible. Para ello, se eliminaron los espaciados entre detectores en un escáner pequeño de animales, creando un único detector centellador de forma cilíndrica. Con esto se busca aumentar la sensibilidad, pues ya no se pierden interacciones en los huecos, y también la resolución espacial. Dos prototipos fueron testeados con simulaciones, y validados experimentalmente. El primero con caras de salida planas y el segundo totalmente cilíndrico. En ambos diseños se observaron efectos debidos a la curvatura del detector que necesariamente han de ser compensados con una calibración.

RESUM

Des de la seua creació en la dècada de 1950, les imatges tomogràfiques hi han resultat molt valuoses en àmbit mèdic ajudant tant en el diagnòstic com en el tractament de moltes malalties. Dins de la imatge molecular, els escàners PET (Tomografia per Emissió de Positrons) generen informació detallada de la interacció dels traçadors amb el teixit del pacient, podent combinar aquesta informació amb imatge anatòmica d'escàners TC (Tomografia Axial Automatitzada) o RM (Ressonancia Magnètica). Amb el fi d'augmentar les prestacions d´aquests equips, els PET de cos complet augmenten la seua cobertura axial, multiplicant el preu dels dispositius i dificultant la seua compra en hospitals i centres d´investigació. Com a alternativa, els escàners PET específics d'òrgans utilitzen un menor nombre de detectors resultant així un preu més econòmic. Un altre avantatge és la possible portabilitat dels aparells. En aquesta tesi abordem tres possibles dissenys de PET específics orientats a diferents òrgans i amb diferent tecnologia i geometria.

El primer de tots, un projecte nacional denominat PROSPET, ha sigut dissenyat i optimitzat per a fer imatge de la pròstata, ja que és molt coneguda l'elevada taxa de càncer de pròstata en homes. El 17% de población masculina patirà càncer de pròstata. El detector escollit per a aquest disseny està format per cristals centellejadors monolítics acoblats a una matriu de fotomultiplicadors de silici. De primeres es va pensar a crear un escàner compost per dues pales, ja que permetria disposar els detectors molt a prop del pacient. El resultat no va ser molt satisfactori a causa de la falta d'informació angular i l'absència d'informació temporal precisa. Per tant, l'última iteració va consistir en una configuració d'anell amb un diàmetre reduït en comparació amb els escàners de cos complet. Es va observar una millora en la sensibilitat i la resolució espacial, així com una qualitat d'imatge acceptable.

El segon dispositiu va ser dissenyat per a optimitzar la configuració d'anell el màxim possible. Per això es van llevar els espaiats entre detectors, creant un únic detector de forma cilíndrica. Amb aquest disseny es busca augmentar la sensibilitat, ja que no es perden interaccions en els espaiats, i també la resolució espacial. Dos prototips van ser testejats amb simulacions i validats experimentalment. El primer amb cares d'eixida planars i el segon totalment cilíndric. En els dos dissenys es va observar efectes deguts a la curvatura del detector que necessàriament ha de ser compensat amb una calibració.

L´últim escàner, denominat projecte CardioPET, està orientat a visualitzar el cor durant el pacient quan és sotmés a condicions d'estrés farmacologic. escàner, denominat projecte CardioPET, està orientat a visualitzar el cor durant el pacient quan és sotmés a condicions d'estrés. Es va recuperar el disseny de les pales per aquest dispositiu, però utilitzant cristals

pixelats, millorant la resolució temporal, permetent implantar algoritmes de temps de vol. Dues pales van ser muntades i testejades tant amb simulacions com experimentalment amb bones prestacions. A més, es va registrar el moviment de les fonts de radiació amb la fi d'aplicar correcció de moviment amb l'ajuda d'una càmera externa i uns marcadors ARUCO. Els algoritmes de correcció de moviment també van ser testejats, demostrant un bon funcionament.

L'últim dispositiu va ser dissenyat per a optimitzar la configuració d'anell el màxim possible. Per això es van llevar els espaiats entre detectors, creant un únic detector de forma cilíndrica. Amb aquest disseny es busca augmentar la sensibilitat, ja que no es perden interaccions en els espaiats, i també la resolució espacial. Dos prototips van ser testejats amb simulacions i validats experimentalment. El primer amb cares d'eixida planars i el segon totalment cilíndric. En els dos dissenys es va observar efectes deguts a la curvatura del detector que necessàriament ha de ser compensat amb una calibració.

ACKNOWLEDGMENTS

This thesis was possible thanks to the hard work of several researchers and colleagues that have helped me during these last years. First of all, I want to genuinely appreciate the effort and wisdom of my director Antonio J. González, who gave me this opportunity and tutorized me all the time with patience, demonstrating not only a high knowledge in the Molecular Imaging field, but also the importance of being a nice person. I also want to thank the two senior scientists José María Benlloch and Filomeno Sánchez for the advices they gave to me and the leadership they have demonstrated during this time.

I cannot forget the importance of my teammates, given that they were capital in my growth as a scientist. I want to thank Andrea González for accompanying me all the process with friendship and enthusiasm. Moreover, I really appreciate Sebastián Sánchez by recommending me at the beginning. Amadeo Iborra assisted me a lot with the image reconstruction and with the code processing, being always of really valuable help. Of course, I want to also acknowledge the help of Efthymios, Marta, Koldo, Liczandro, Albert, Héctor, John, Celia, Sara, David, Laura, Neus, Sofía and the rest of the group people which have worked with me across the years. They are all excellent people and I wish everyone a good future in the science field.

I want to appreciate also my family support because they always believed in my work and supported me at any time. First, I want to mention my mother María Jesús, to whom is dedicated this thesis, my father Benito, my brother Emmanuel and the rest. Also, a special mention to my cousin Pascual. Finally, to all my friends, even those who I have lost the contact.

Index

ACRONYMS

APD	Avalanche Photodiode
BGO	$Bi_4Ge_3O_{12}$
CASTOR	Customizable and Advanced Software for Tomographic Reconstruction
CNR	Contrast to Noise Ratio
CoG	Center of Gravity
CPU	Central Processing Unity
CT	Computed Tomography
CTR	Coincidence Time Resolution
CZT	Cadmium Zinc Telluride
DOI	Depth of Interaction
ESR	Enhanced Specular Reflectors
FBP	Filtered Backprojection
FWHM	Full Width Half Maximum
GATE	Geant4 Application for Tomography Emission
keV	kiloelectronvolt
LAT	Limited Angle Tomography
LD	Light Distribution
LM	List Mode
LOR	Line of Response
LSO	Lutetium Oxyorthoscilicate
LYSO	$Lu_{1.8}Y_2SiO_5Ce$
MAF	Multiple Acquisition Frames
MI	Molecular Imaging
ML	Maximum Likelihood
MLEM	Maximum Likelihood Estimation Method
MR	Magnetic Resonance
MRI	Magnetic Resonance Imaging
NECR	Noise Equivalent Count Rate
NEMA	National Electrical Manufacturers Association

OP	Optical Photons
OSEM	Ordered Subsets Expectation Maximization
PCa	Prostate cancer
PDE	Photon Detection Efficiency
PET	Positron Emission Tomography
PMMA	Polymethyl Methacrylate
PMT	Photomultiplier Tube
PSF	Point Spread Function
RF	Radiofrequency
RTP	Rise to Power
SiPM	Silicon Photomultipliers
SNR	Signal to Noise Ratio
SPECT	Single Photon Emission Computed Tomography
TOF	Time of Flight
TOR	Tube of Response
TTL	Transistor-transistor Logic
US	Ultrasounds
USI	Ultrasound Imaging
VOI	Volume of Interest
WB-PET	Whole-Body PET

1. INTRODUCTION

1.1. Introduction

Since the introduction of Medical Imaging, its relevance has been growing to the point that it is very difficult to imagine many diagnoses and therapy treatments without the contribution of specific and accurate images. In the Medical Imaging field there are several techniques, with different output images. Molecular Imaging (MI) is a branch of Medical Imaging focusing on molecular processes occurring within the patient body, such as for example physiology changes. MI is different from other techniques that precisely return a visualization of the organs and bones structures [1]. MI has the potential to significantly increase the accuracy of diagnosis. Moreover, MI provides *in vivo* biological information of multiple pharmacotherapies and medical drugs, due to its ability to discern different physiological changes in the tissues. Currently, with the design and development of MI systems, and the research of molecular specific interactions of the tissue with certain substances, this field is rapidly expanding to many clinical applications. Just to mention some of them, MI is extensively applied in oncology, cardiology, and neurology [2].

The interest in MI has been increasing over the years. Many specialists consider MI as one of the most important instruments in both clinical and preclinical studies [3]. In order to design a study or treatment using MI techniques, it is important to start by identifying the molecular process to be tracked. For example, there is an increased glucose consumption of most cancerous tumors [4]. Thus, radiotracers based on glucose are used for cancer diagnosis and therapy treatment assessment [5]. Finding a distinct target that identifies a specific molecular process is challenging, and it represents one of the difficulties of this discipline. MI can provide reliable information of molecular processes if appropriated markers are used. These are

molecules that focus on a specific process. With the use of radiotracers, the number of molecular targets increases, and, at the same time, they provide information on the biological pathways. Currently, investigations based on nanoparticles make it possible to combine both. For instance, in Luque-Michel et al. [6] it is suggested the use of Doxorubicin (a drug compound) encapsulated using superparamagnetic nanoparticles, to be applied to tumor angiogenic vessels. In the future, MI techniques would allow one for a personalized medicine, and thus to design a specific treatment for every patient [7].

Historically, we can establish that the first attempts in Medical Imaging were performed by Wilhelm Roentgen in 1895. By using an unknown kind of energy at this moment, called later as X-Rays, together with photo-plates he was able to generate the first radiography ever. Later, some transcendental discoveries, such as for instance the natural radioactivity by Henri Becquerel, or the synchrotron radiation which was used to produce radioisotopes, helped to understand this promising field [8]. Over the years, the scientific community has put a lot of effort to increase the benefits and reduce the disadvantages of ionization radiation in MI [3]. In Figure 1, a comparison between the first medical image and a clinical treatment using multiple Medical Imaging techniques is presented, showing how the technology evolved over the years to provide more reliable information.

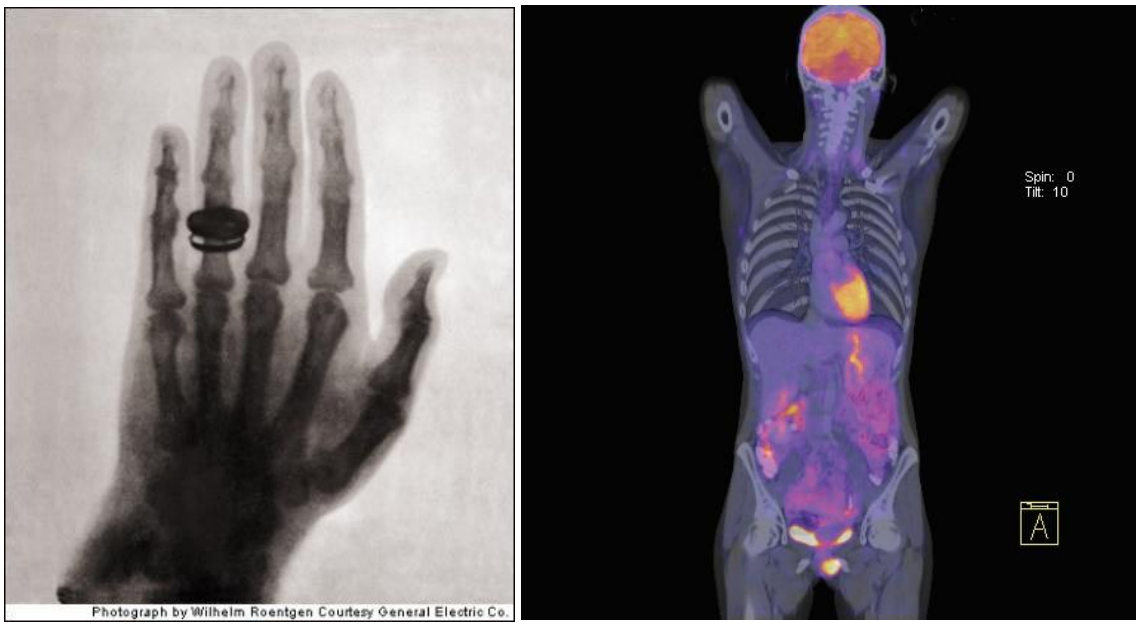

Figure 1. Left: First X-ray image performed by Roentgen in 1895 (www.revistamedica.com). Right: Multimodal PET/CT images from a conventional scanner (www.diagnosticomaipu.com).

As introduced above, MI techniques generate an image of a radiotracer concentration [5]. The most known MI techniques are Positron Emission Tomography (PET) and Single Photon Emission Computed Tomography. These techniques are combined with other Medical Imaging techniques that provide anatomical information. In the sections below, some of these Medical

Imaging techniques such as Computed Tomography (CT), Magnetic Resonance and Ultrasounds (US), are briefly introduced, together with SPECT. The PET technique will be described in more detail later since this PhD work is based on the performance of this scanners.

1.1.1. Computed Tomography

One of the most classical Medical Imaging techniques is radiography [9]. Here, X-rays are produced when accelerated electrons, due to an electric field produced by the anode and the cathode, interact with a target that stop them, typically a Tungsten material. These X-rays are directed to the patient body, so most of them pass through, but others interact with the bones and tissues. Those that manage to escape produce a planar image with anatomical information. X-rays interact more with bones, due to their higher density than the rest of surrounding tissues. X-ray energies are typically in the range of few tens of kilo-electronvolt (keV), so they are considered low energy processes. Figure 2 shows an X-ray tube scheme in detail (left) and a 2D radiography of a hand (right).

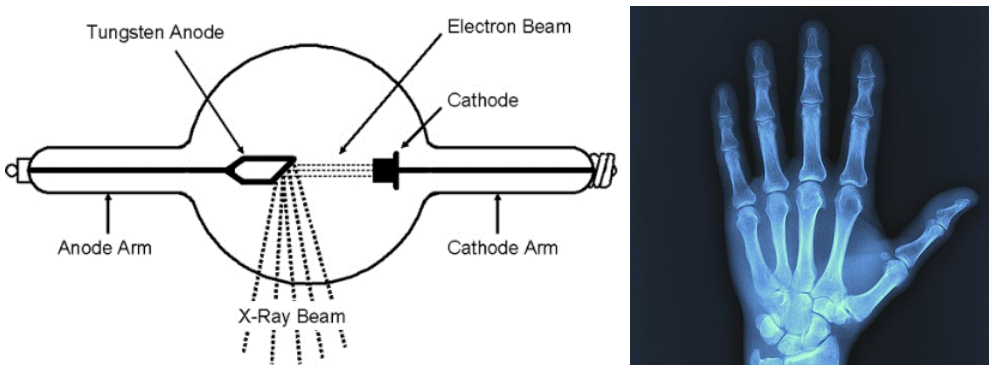

Figure 2. Left: Sketch of an X-ray tube design (www.excillum.com). Right: Conventional X-ray planar image (www.imaginghealthcare.com).

CT combines the information of several radiographies [10], taken at different angles (also called projections), allowing to generate a tomographic 3D image [11], after the complex process of image reconstruction. Herein, the meaning of tomography is related to the generation of a 3D image with the combination of multiple 2D projections. However, despite having access to a full 3D anatomical image, the total dose to the patient is rather high. For a chest CT, as more as 400 to 600 radiographies are carried out to generate the 3D image. For a chest CT examination, the radiation dose is equivalent to more than 2 years of natural background radiation. Therefore, CT scans of the whole patient are minimized unless necessary [12]. Nevertheless, radiography is one of the most used techniques in the hospital services, since it is simple and relatively cheap, providing first insights for bone injury and tissue deformations. Moreover, CT is reliable in other cases such as in the search for tumoral structures [13]. The 3D anatomical information is also linked to several Medical Imaging applications, as for instance to enable corrections and the co-

registration of other modalities. Figure 3 left shows several anatomical views of a patient, and on the right a photograph of a CT scanner. It is important to remark that, with tomographic images, there is no superimposition of structures like in the planar images because we can locate them in different planes. Nowadays, several techniques have been proposed to reduce the total amount of dose, including Iterative Mode Reconstruction or Dose Modulation to name a few [14].

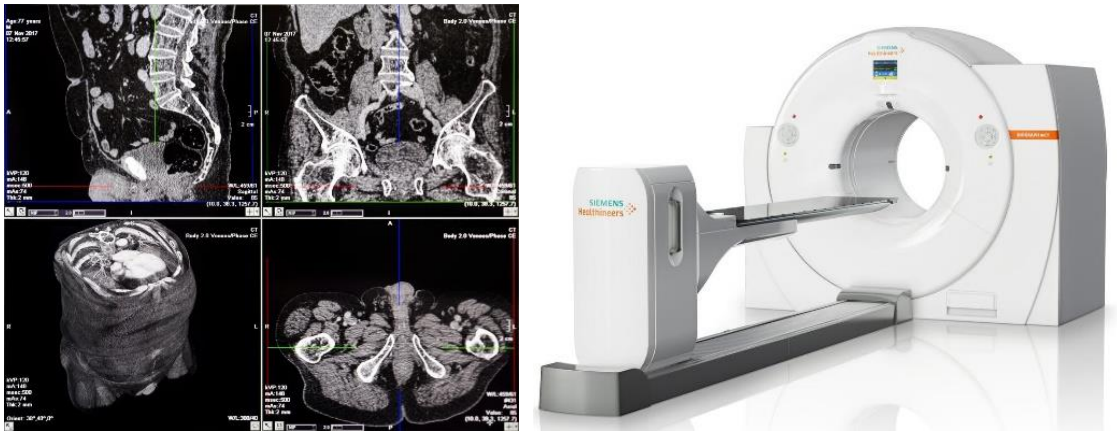

Figure 3. Left: Examples of anatomical CT images showing different slices (www.medicalnewstoday.com). Right: Photograph of a commercial CT scanner (www.siemens-healthineers.com).

1.1.2. Magnetic Resonance Imaging

Magnetic Resonance (MR), unlike Molecular Imaging techniques and CT scanners, does not employ any kind of ionizing radiation [15]. The image is produced by the interaction of typically the hydrogen atoms of the body with magnetic fields (see more details below). It is best suitable for soft tissue such as muscles and tendons; however, it exhibits some challenges for hard tissues (bones for instance) [16]. Moreover, it is more expensive than radiographs or CT. One of the reasons is the use of superconductive magnetic coils that need significant cooling [17]. In Figure 4 two different MR images are shown, a human brain on the left and the prostate/hip area on the right.

MR works with a main static magnetic field that aligns the hydrogen atoms along its direction. To do so, it requires coils that produce a high magnetic field of several Tesla (1.5 to 7 T in human studies) [18]. This is an extraordinarily strong magnetic field considering that the Earth one is just around 40×10^{-6} Tesla. Therefore, metal artifacts or implants are not allowed during an MR examination. At the same time, a pulsed radiofrequency (RF) signal excites the protons creating a misalignment between their spin direction and the main magnetic field and, when these signals are turned off, they return to the equilibrium stage releasing energy. This specific energy, and the relaxing time of the protons, is characteristic at the emission position and also of the different tissues, so reconstruction algorithms use this information to return a tomographic

image. MR has shown to be significantly useful in brain studies given that we can appreciate the differences between the grey and the white matter. There exist some substances that are used as contrast agents to improve the image signal-to-noise ratio (SNR) [19], such as gadolinium [20].

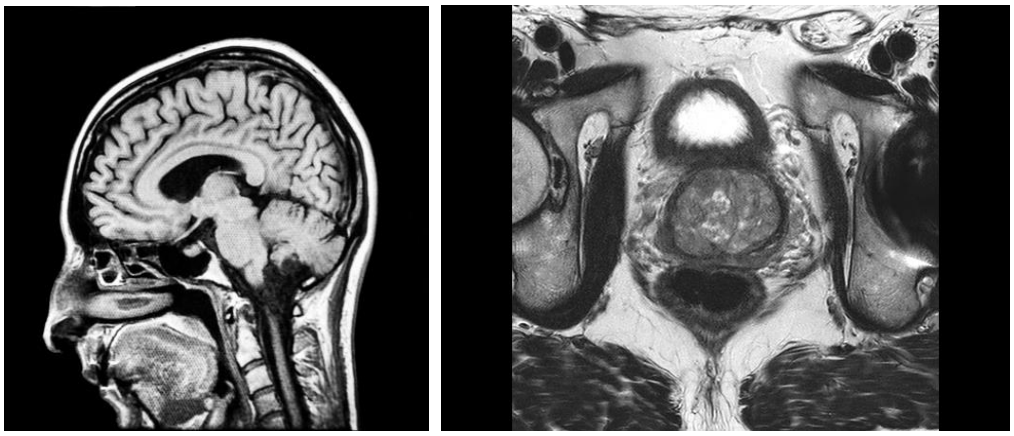

Figure 4. Left: MR view of a human head (www.istockphoto.com). Right: Axial view of an MR image of a prostate area (www.mriclinicalcasemap.philips.com).

1.1.3. Single Photon Emission Computed Tomography

Single Photon Emission Computed Tomography (SPECT) is based on the detection of gamma rays. These gamma rays can have energies in a wide range from about 30 to 400 keV depending on the selected radiotracer [21][22]. The patient is injected with a radiotracer in micromolar concentrations, in which one or few of its atoms have been replaced with a radioactive element that, for SPECT imaging, is a gamma ray emitter [23][24]. Some gamma rays pass through the body and are detected in the so-called gamma cameras. There is a variety of available radiotracers, depending on the kind of study or tissue to be examined. The most used in SPECT is the ^{99m}Tc, which emits a very characteristic 140 keV gamma ray. However, others such as ^{201}Tl or ^{67}Ga are for instance used for brain studies. SPECT detectors are usually composed by a scintillation crystal and a photosensor device. Scintillation crystals convert the gamma rays into low energy photons, typically in the visible range, whereas photosensors produce a measurable electric signal of such visible photons. Associated electronics allow one to estimate the gamma ray interaction position within the crystal as well as its deposited energy. Scintillator crystals, such as NaI or CsI, are the most used for gamma cameras designs. Since the gamma rays in SPECT have an energy typically below 350 keV, these crystals are able to stop enough gamma rays. For instance, for a gamma ray beam of 140 keV, a 10 mm CsI block stops around 96% of the total incident particles [25]. An alternative to these scintillators-photosensor devices are the detectors based on semiconductor structures such as cadmium zinc telluride (CZT). CZT detectors exhibit advantages such as a higher extrinsic spatial resolution and a superior sensitivity, but lower stopping power [26].

Gamma cameras use collimators to determine the emission source [27], see Figure 5. All the gamma rays travel through the collimator to form a planar 2D image. Collimators are typically made of Tungsten or Lead. When using collimators, many gamma rays do not reach the gamma camera, and that means a loss of sensitivity. A parallel hole collimator example can be found in Figure 5 left, as well as a SPECT image for a brain study on the right.

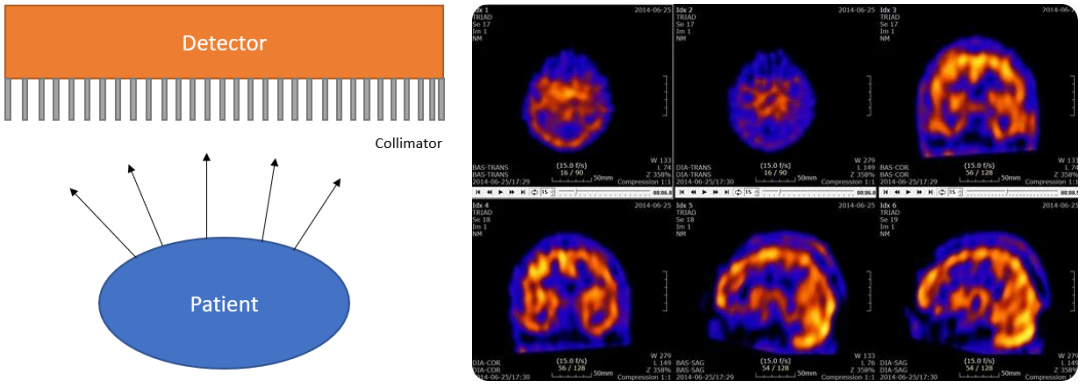

Figure 5. Left: Sketch of a gamma camera. Right: 3D views of a brain study using SPECT (www.news-medical.net).

SPECT scanners are composed by several gamma cameras, or by a single rotating gamma camera, covering projections for all 360 degrees and, therefore, allowing one to also retrieve a 3D tomographic image. The first SPECT designs date from the 1950s decade. However, until the 1980s they were not really extended in diagnosis processes [28]. SPECT systems require longer scanning times when compared with other MI modalities such as PET systems, because of that lower efficiency. Moreover, the dispersion of gamma rays produced within the patient body or in the tungsten collimator, also reduce the system sensitivity.

SPECT is highly extended in cardiovascular research, particularly for lesions related to myocardium tissue abnormalities. Furthermore, it is also very reliable in brain imaging [29]. Blood perfusion, and other injuries such as signs of dementia, can be explored with the inclusion of specific biomarkers such as ^{18}F-FDG [30].

1.1.4. Ultrasound Imaging

There exist other medical imaging technologies that use different physical processes for the diagnosis or therapy assessments of a variety of diseases. For instance, using ultrasound (US) waves with transducer probes, non-invasive anatomical images can be provided [31]. These probes are made with piezoelectric materials. Waves with frequencies larger than 20 kHz interact with the human body structure and detected after they rebound in the tissue. A known application of US is the study of the blood flow by means of the Doppler Effect. Another application is imaging and analyzing the fetus in pregnant women, see Figure 6.

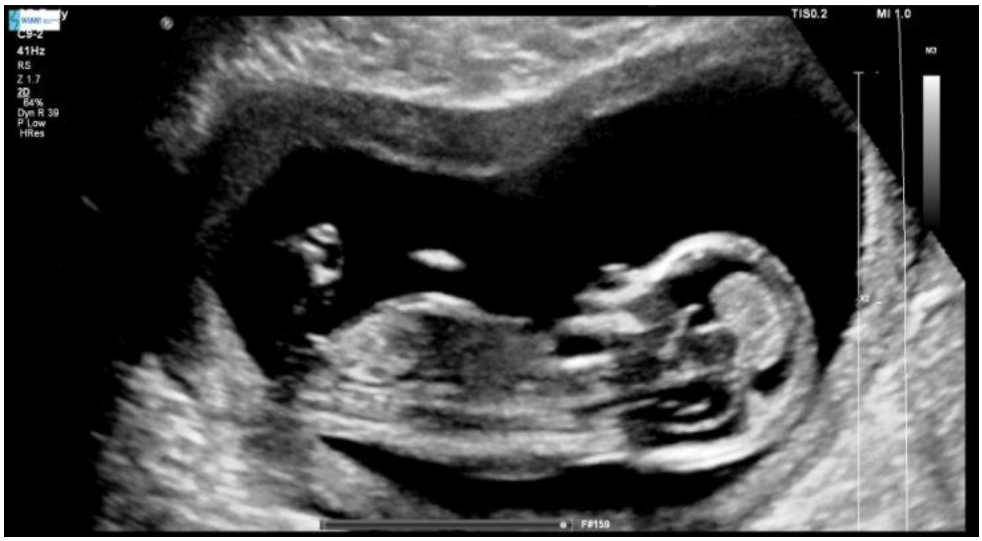

Figure 6. Ultrasound image of a pregnant patient (www.babycenter.com.au).

1.2. Positron Emission Tomography

This thesis is focused on the design of different Positron Emission Tomography (PET) systems, as well as their performance and capabilities. Therefore, the properties and characteristics of the PET modality will be explained with more detail [32]. PET exhibits similarities with the SPECT modality in the sense that it uses a radiotracer that is injected to the patient with the objective to interact with the cells where the disease is dominant. In the PET modality, isotopes that are positron emitter are injected to the patient, such as ^{18}F [33] or ^{11}C [34], for instance.

The emitted positrons move erratically around the source, inelastically interacting with cortical electrons of the surrounding atoms, before they annihilate with the electrons of the atom cortex. The distance that positron travels before its annihilation with an electron is called positron range and depends on the medium and the kinetic energy of the positron (e+). For example, the positron emitted from a ^{18}F nucleus in water, can travel as more as 2.4 mm before annihilates, but just 0.6 mm on average, whereas for ^{68}Ga this range increases to 3.5 mm on average [35]. After the positron-electron annihilation, two 511 keV photons are produced travelling in opposite directions, almost collinearly, see PET based principle in Figure 7.

As we can appreciate in Figure 7, conventional PET systems included multiple gamma detectors arranged in a ring configuration, so benefitting the collection of both annihilation photons. There are other PET configurations different from rings that will be introduced below. One of the advantages of PET in comparison to SPECT is that there is no need for collimators to know the source of the radiation and, thus, their sensitivity is much higher, up to two orders of

magnitude [36]. However, SPECT systems are usually more economical since their isotopes are easier to be produced and they have longer lifetimes [37].

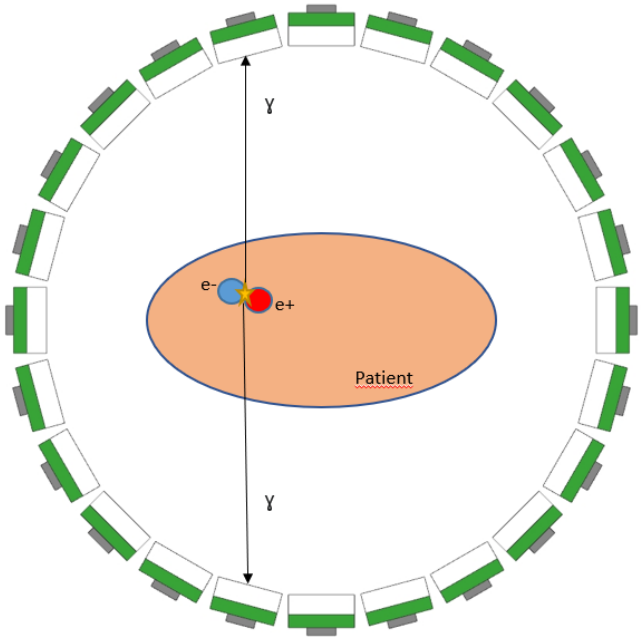

Figure 7. Sketch of a PET scanner with a ring configuration. Positron (red) and electron (blue) annihilate, producing two almost colinear annihilation photons (black arrows), that are registered as a coincidence event.

When two 511 keV annihilation photons are registered within a time window (typically of just few nanoseconds), a Line of Response (LOR) is traced between the two detectors that are involved. Ideally, only true LORs should be accepted during the reconstruction process, this means LORs that come from the same positron-electron annihilation and not gamma rays that are scattered within the patient or detectors. Unfortunately, this is not the case because the system cannot distinguish between scattered and true coincidences [38]. Furthermore, when the injected activities are high, random coincidences increase becoming predominant over the trues and scatter coincidences. In Figure 8, random, scatter and true events are depicted. Random coincidences are most likely originated from different annihilation processes. There exist some methods to reduce these events, such as decreasing the coincidence time window [39][40]. However, we should be careful when we establish the coincidence time window, it must be adequately wide to accept the major number of true events, and this depends on the scanner geometry.

The two annihilation photons detected in PET scanners have the characteristic energy of 511 keV, usually more energetic than in SPECT systems. Thus, it is necessary to design a detector block capable of stopping a high number of these photons. Inorganic scintillation crystals are good candidates [41]. In contrast to SPECT where NaI or CsI crystals are often used ($\rho \simeq 3$ g/cm^3), PET designs make use of denser scintillators. Herein, crystals such as $Lu_{1.8}Y_2SiO_5Ce$, commonly

known as LYSO, or $Bi_4Ge_3O_{12}$, known as BGO, both with densities around 7 g/cm^3, are suitable to stop high energy gamma rays. Nowadays, Silicon Photomultipliers (SiPMs) are the preferred choice for photosensors to transform the scintillation light into an electrical signal. SiPMs are composed of many active microcells disposed in an array [42]. Every time an optical photon (OP) generated from a scintillation process reaches one of the microcells, there is a Photon Detection Efficiency (PDE) probability of this being activated and to produce the electrical signal. In the case of an activation, the microcell requires some time for processing, generating a deadtime when other optical photon would not be registered in that particular cell.

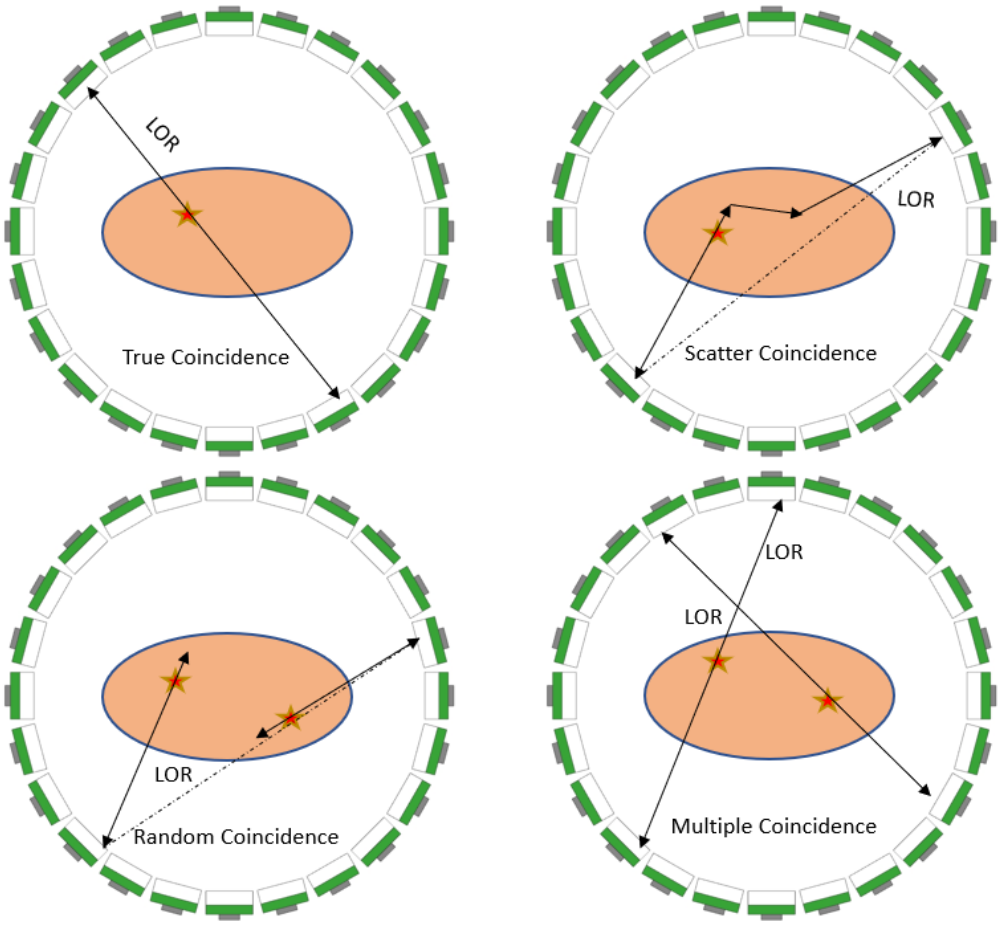

Figure 8. Definition of true, scatter, random and multiple coincidences.

According to the energy of the incident annihilation photon, combined to the density of the scintillator crystals, two important radiation-matter interactions may happen within the material:

a) Compton scattering. An inelastic collision of the annihilation photon with an electron that deviates the incoming particle. This effect produces a wrong determination of the true incoming annihilation photon scintillation coordinates, and it is typically predominant (70% for 20 mm thick LYSO crystals) [25].

b) Photoelectric effect. The gamma ray is totally absorbed in the material depositing the whole amount of its energy so non blurring is produced.

Due to the absence of the blurring caused by the multiple interactions that suffers the gamma ray, Photoelectric events are suitable for the coordinates position. Regarding crystal geometries, there are mainly two implemented detector configurations in PET systems: pixelated and monolithic, both illustrated in Figure 9 (top left and top right, respectively). Each one has its advantages and disadvantages, and they are explained below.

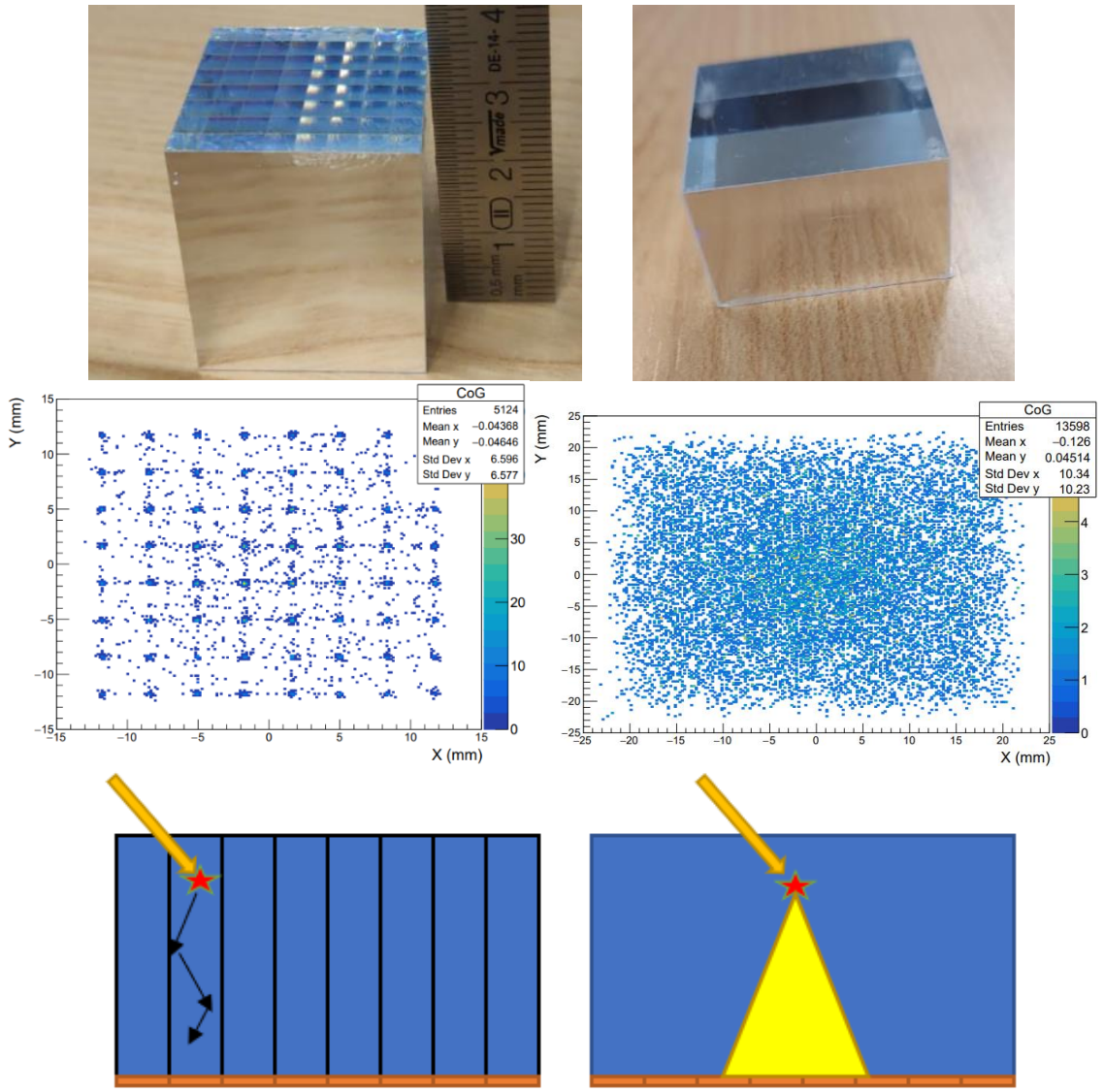

Figure 9. Top Left: Photograph of a pixelated crystal. Top Right: Photograph of a monolithic crystal. Center Left: Flood map of an 8 × 8 pixelated crystal array. Center Right: Flood map of a 50 × 50 × 15 mm³ monolithic block. Bottom Left: Sketch of a pixelated scintillator array coupled 1 to 1 with a photosensor array. Bottom Right: Monolithic scintillator block coupled to a photosensor array.

1.2.1. Crystal configurations

Pixelated crystals are the most extended type of configurations in scintillators-based detectors, see Figure 9. Crystals are cut in individual pixels and later arranged in arrays [43]. The entrance and lateral surfaces of these pixels are often covered with a reflective material to increase the light collection into the photosensors coupled at the exit face of the crystals. Among others, Enhanced Specular Reflectors (ESR) are perhaps the preferred choice for reflectors. The intrinsic spatial resolution in this configuration strongly depends on the pixel size [44]. A flood map of an array of 8 × 8 LYSO crystals is introduced in Figure 9. One way to improve the intrinsic spatial resolution is to reduce the pixel size but this increases the cost of the detector since smaller pixels are more expensive to produce. Reducing the pixel size also impacts the energy performance and increases the inter-crystal-scattering. Nowadays, we can find PET systems (pre-clinical imaging) with pixels sizes in the range of 1 mm. Detectors based on pixelated crystals do not intrinsically provide depth of interaction (DOI) information of the gamma ray within the pixel. However, such DOI can also be estimated with some methods, for instance using a double side readout [45]. DOI will be introduced later in section 3.3.3. If proper readout electronics are employed, configurations based on small pixels result in high performance timing capabilities reaching 200 picoseconds (ps) or better [46].

Monolithic crystals are based on a single scintillation block that is also coupled to a photosensor array [47]. In such crystals, scintillation light spreads isotropically from the gamma ray interaction position inside the crystal. Most of this light reaches the photosensor array, however the amount will depend on the crystal geometry and treatment applied to crystal walls. Figure 9 shows a photograph of these crystals, and the expected light collected by the photosensors for the case of having black paint in the surfaces. In contrast to pixelated configurations where just one or few photosensor collects most of the scintillation light, in the case of monolithic crystals several photosensors are illuminated with such light. On the one hand it is possible to reproduce the light distribution (will depend on the readout) so the planar XY coordinates can be estimated with for instance a Center of Gravity (CoG) algorithm or others. Notice there are several types of readout schemes with pros and cons [48]. The impact DOI can be approximated using the width of the Light Distribution (LD). Herein, there is a narrow width when the interaction is closer to the photosensor surface and wider if the interaction happens at the entrance surface. On the other hand, providing an accurate estimation of the interaction time is more challenging than in pixelated configurations because there are more photosensor elements involved simultaneously, reducing the SNR of each one and, thus, its precise time determination [49].

The intrinsic spatial resolution depends on many factors such as the crystal surfaces treatment or the crystal thickness [50]. PET scanners based on monolithic crystals are typically more economical than the pixelated, especially when compared with pixelated crystals with small pixels (<1.5 mm). Moreover, for the same detector module dimensions, monolithic based detectors achieve a higher sensitivity since they avoid the dead areas in between pixels. In this PhD work we have worked with both crystal configurations, but the choice of preference are monolithic crystals due to their enhanced DOI capabilities, which will be explained later, that become very important for PET scanners with small apertures [51].

1.2.2. Intrinsic spatial resolution

The spatial resolution in a PET system is related to the intrinsic resolution of the individual detectors, therefore an optimization of the detector resolution is required to ensure good scanner performance. In monolithic crystals, the intrinsic detector resolution depends on the optimization or knowledge of the LD that reaches the photosensor elements. For instance, by covering the lateral surfaces of the scintillator with Teflon, the Lambert diffusion is maximized, and the total number of collected optical photons increases, improving the energy resolution [52]. A similar energy resolution enhancement can be observed with an ESR material covering the detector surfaces. However, these two treatments break the LD, and the spatial resolution deteriorates [53]. Introducing a retroreflector material (RR) at the entrance surface permits to increase the total number of optical photons collected preserving the light distribution, so both the spatial and energy resolutions improve [54]. RR films bounce back the scintillation light to the emission point. This detector configuration will be introduced in one of the prototypes developed in this thesis. A good example of a PET scanner that employs monolithic detectors is the Albira PET system [55]. All their monolithic blocks are fully black painted so only direct light reaches the SiPM array. A recent study carried out with this system, but already in the form of a PET insert compatible with high-field MRI, results in a system spatial resolution at the center of the Field of View (FOV) of 0.68 mm in the radial component, with a small spherical ^{18}F source a sensitivity of 11% is found [56].

In pixelated crystals the trend to improve the spatial resolution of the detectors is to reduce the pixel size. For instance, the pre-clinical PET scanner LABPET II uses pixels of $1.12 \times 1.12 \times 10.6$ mm^3 coupled to the photosensors, therefore they can achieve a very good system spatial resolution below 1 mm [57].

Nowadays, many PET scanners are found with different geometries and technologies. The performance of the detector modules directly affects to the capabilities of the scanners, which

will be introduced in section 3.3. Regarding the scanner performance the National Electrical Manufacturers Association (NEMA) developed some procedures to fairly compare different scanners. NEMA protocols explain how to evaluate parameters such as the spatial resolution or sensitivity accurately [58]. There exist different versions of NEMA protocols that will be introduced later.

1.3. Hybrid imaging

Most of the advantages and disadvantages of the medical imaging modalities have been explained above. While MR and CT provide anatomical information for soft and hard tissues, PET and SPECT return functional information of molecular processes. In the last years, there is a trend to simultaneously obtain functional and anatomical information [59]. It must be mentioned that the combination of PET and CT is well stablished since few decades, and there are not new installations of PET without a CT scanner in a tandem configuration: PET/CT [60]. In addition to other applications, the anatomical 3D images produced by the CT are employed in the attenuation correction of PET data [61].

PET and CT cannot run simultaneously, due to detector design constrains. An alternative approach is to merge PET and MR. As it was explained above, MR works with very intense magnetic fields. PET electronics are sensible to the magnetic fields present in MR systems (radiofrequency, switching gradient and main fields). Moreover, PET systems based on Photomultipliers tubes (PMT) photosensors cannot be immersed in high magnetic fields, since the working principle of PMTs is based on the acceleration and multiplication of electrons, and MR highly deteriorates the PMT signals. PET/MR was feasible with other approximations. One way to proceed is to first acquire the data with the MR system and then move the patient bed to the PET scanner (tandem approach) [62], so with a translational movement one can sequentially acquire both images. This solution can exhibit problems with possible misalignments and also a large patient scanning time (low patient throughput). An approach to merge PET and MR that also was investigated in the past was the use of optical guides to extract the scintillation light from the scintillators to the PMT, which are placed far from the magnetic field center. This method was employed in 2006 in the microPET-MR system [63], but the results showed some signal degradation.

In recent years, PMTs have been successfully replaced by SiPMs [64]. Since SiPMs are based on semiconductor technology, they are rather immune to magnetic fields. In the 1950 decade, the first functional SiPM were developed and known as avalanche photodiodes (APD), but later

they were improved to Geiger-mode avalanche photodiodes, also knowns as single photon avalanche diode (SPAD). SiPM presents also other advantages such as compactness. These days is very usual the design and building of PET scanners that fit inside the MR scanner with no signal degradation and with excellent performances. One of the first scanners that employed APD (similar to SiPM) instead of PMT was the Siemens Biograph mMR [65]. The mMR is composed of 8 rings with 56 detector blocks employing Lutetium Oxyorthoscilicate (LSO) pixel crystals of 4 $\times$ 4 $\times$ 20 mm^3 dimensions.

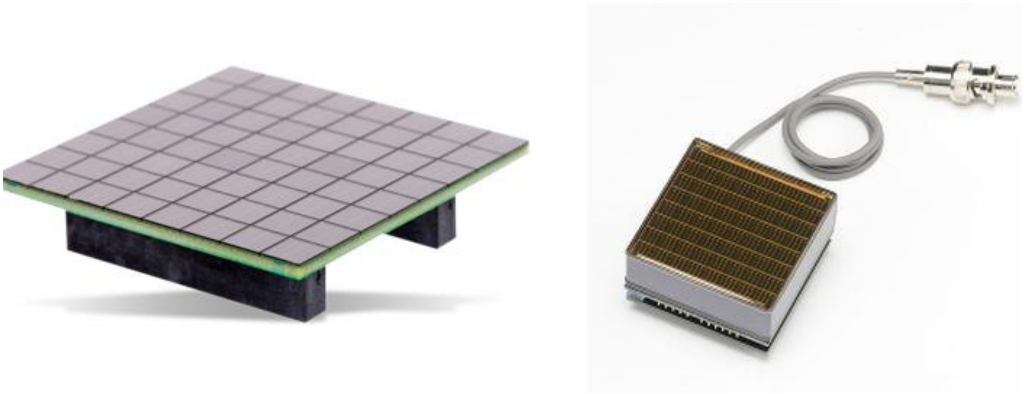

Figure 10. Left: SiPM array (www.mouser.es). Right: PMT tube (www.directindustry.es).

Hybrid imaging is not exclusive of whole-body PET (WB-PET) scanners. Hybrid pre-clinical systems are also found. They present a reduced size so only mice or a rat imaging is carried out. These kinds of systems are very useful in medical research. For instance, the PET insert commercialized by Bruker [56], exhibits the same performance independently of the MR sequence. This scanner is composed by 3 rings of 8 monolithic LYSO crystals with 10 mm thickness, allowing to estimate the DOI with 2 mm accuracy. In Figure 11, an example of 2D slices of simultaneous PET and CT images of a mouse are depicted.

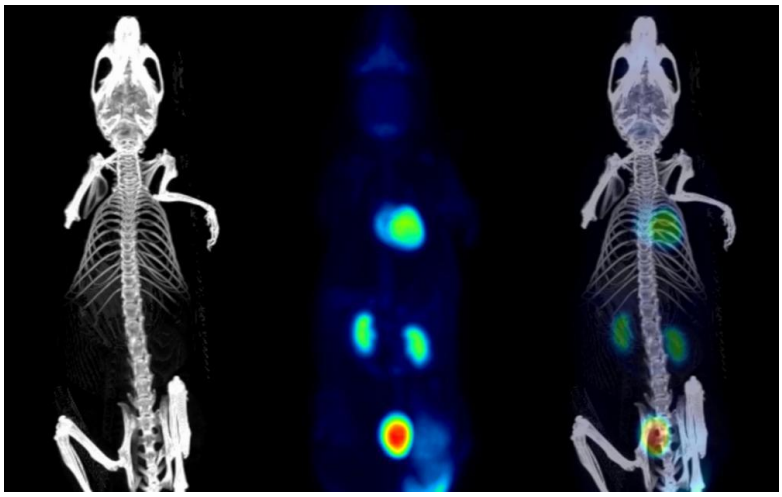

Figure 11. Hybrid PET – CT image slices. CT image (grey) provides an anatomical image whereas PET one (color) reveals the biomarker concentration (www.bruker.com).

1.4. Dedicated systems, novel geometries

Improving PET imaging performance, such as the spatial resolution or sensitivity, without increasing the system cost, can be achieved by considering smaller design apertures, specific to a single organ target [66]. Notice that conventional WB-PET scanners transaxially cover the patient size and make use of a movable bed to scan the axial length. Specific systems exist and are optimized for brain, heart, breast, or other organs. By placing the detectors closer to the tissue or organ, dedicated systems manage to improve sensitivity since more gamma rays are stopped and registered. Typically, detectors with high intrinsic resolutions are also used, so a better image-quality can be obtained. When using such PET scanners, research centers and hospitals reduce instrumentation costs with no degradation in their imaging capabilities. This approach, combined with the development of new and more specific radiotracers, represent one of the main research lines in MI techniques [66].

As an example for dedicated clinical PET systems, the MINDView PET scanner was developed at the *"Instituto de Instrumentación para Imagen Molecular"* in Valencia, see Figure 12. This project was a proposal FP7, with a grant agreement ID: 603002, with almost 7 M€ of budget. MINDView is a brain PET insert compatible with MR scanners with magnetic fields as high as 3 Tesla. Detector modules are composed of monolithic LYSO scintillator crystals of 50 × 50 × 20 mm^3, with all lateral surfaces black painted to avoid as much as possible all the light dispersion, and a RR layer at the entrance face. They were coupled to a 12×12 SiPM arrays of 3 × 3 mm^2 area (a special MINDView-series type was used) [47]. 3 rings of 20 detector modules were mounted with an inner diameter of 33 cm. The insert operated well independently of the MR sequence employed for brain imaging. The system achieved a sensitivity of 7% and its spatial resolution, at the FOV center, was 1.7 mm. For comparison purposes, the PET scanner in the mMR system exhibits 1.33% sensitivity, and the spatial resolution at the FOV center is around 4 mm [65].

Li et al., have proposed an alternative of the classical ring configuration for PET systems for neck tumors [67]. The PET system is based on two panels. This is a design that we will also describe below as part of this thesis. Two detector materials were employed: LYSO or CZT. Pixel sizes is 1× 1 × 20 mm^3 were distributed in a 150×200 mm^2 panel reaching an 86% fill factor. Two panels of this characteristics were built and separated by 200 mm. The LYSO configuration reached 0.7% sensitivity. This dual panel PET scanner approach has also been tested with Monte Carlo simulation for breast cancer imaging [68]. One of the advantages of this system is that the two-panel separation is adjustable depending on the breast size. With a 4 cm panel separation, the spatial resolution remains at 1 mm within the entire FOV. These systems lack some angular

information resulting in the appearance of a very characteristic artefacts in the reconstructed image. Such PET geometry is named limited angle tomography (LAT). For illustration, in the case of a spherical source, the artefact is observed as an elongation in the panel-to-panel direction. One way to reduce this effect consists in placing the panels closer but this depends on the acquisition or organ under study. If the time resolution of the scanner is good enough, then alternatives reconstruction algorithms can be applied, partially mitigating these artefacts, but especially improving the image SNR [69] These algorithms will be explained later.

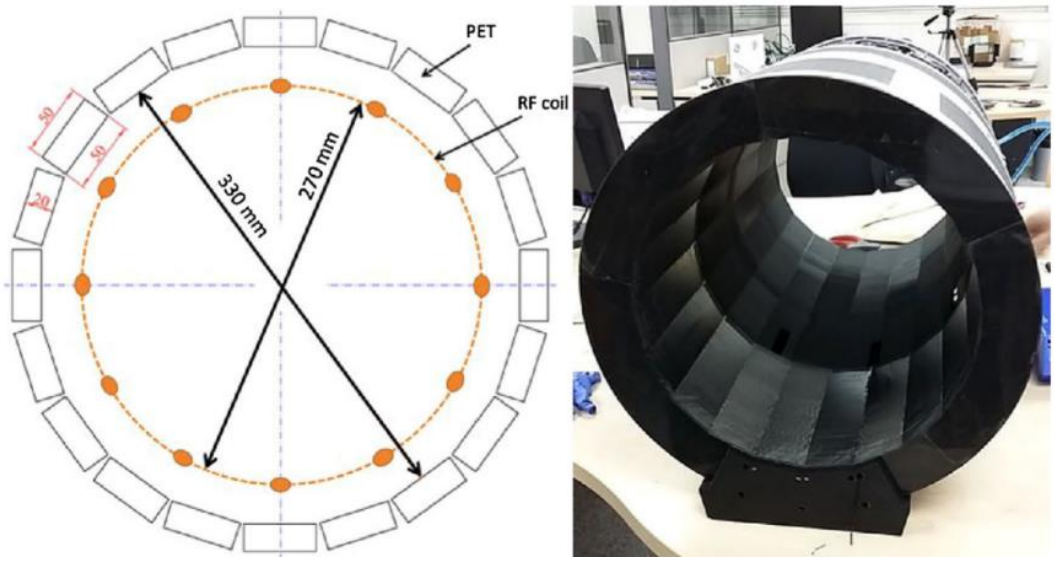

Figure 12. Left: Sketch of the MINDView PET scanner showing the position of the RF coil and rungs. Right: Photograph of the scanner.

An important drawback of organ dedicated PET scanners is that despite the improvement in system sensitivity and spatial resolution, their uncommon geometry can make the reconstruction process complex. Another possible disadvantage is the radiation that comes from outside the FOV that can deteriorate the image and produce additional artifacts, but the use of external shielding can reduce this effect.

In the diagnosis and treatment follow-up of prostate cancer (PCa), an alternative novel PET design makes use of a rectal PET probe working in coincidences with an external detector, see Figure 13 left. The probe combines information from an ultrasound sensor together with a very small PET detector. Approaching the probe close to the lesion assure a sensitivity improvement. The reconstruction process is complex, requiring synchronization of the probe position relative to the external PET detectors. Referring to the brain, a novel design has been simulated and constructed that combines a semi-spherical PET structure with detectors at the chin area, see Figure 13 right [70][71]. With this novel PET configuration, authors are able to obtain a sensitivity

close to 10% at the FOV center, and a spatial resolution of 2 mm. Moreover, the parallax error is corrected since detectors account for DOI capabilities.

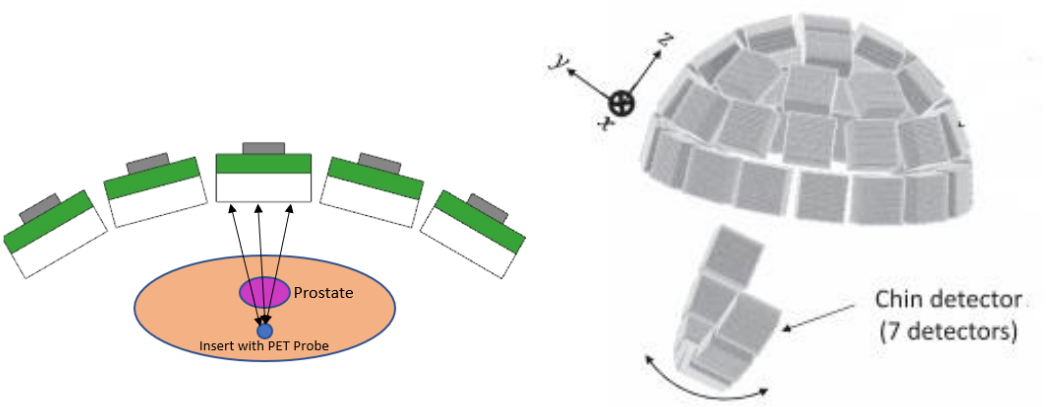

Figure 13. Left: Scheme of a PET based on a rectal detector probe and detectors panels external to the patient. Right: Helmet PET brain scanner with the addition of chin detectors to enhance the sensitivity [71].

In Figure 14 the aspects of organ-dedicated PET scanners and WB-PET systems are depicted, showing in green the advantages and in red the disadvantages.

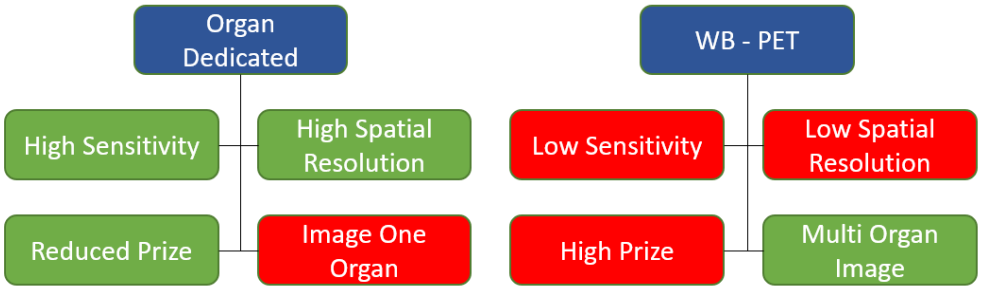

Figure 14. Main capabilities of organ-dedicated and WB-PET systems.

1.5. Future trends

PET systems, both clinical and pre-clinical, with novel geometries have been presented and briefly discussed above. These systems would improve their performance if the detectors time resolution is improved, such as in the case of the two-panels configuration, as we will explain later. LYSO scintillation crystals are efficient stopping the 511 keV gamma rays but exhibit limit timing characteristics since their pulses have a rise time of 70 ps and a decay time of 45 ns [72]. BGO crystals are even slower, with a 20 ns rise time and above 300 ns decay time. It is necessary to reduce these times to further enhance current detectors time resolution [73]. Nevertheless, notice that the commercially available Siemens Vision already reaches a timing resolution of the whole system of 214 ps using LSO pixels.

Reaching Coincidence Time Resolution (CTR) values below 100 ps will significantly improve the PET performance [73]. Scintillation plastics, such as EJ–232, are much faster than inorganic materials, with a rise time of 0.35 ns and a decay time of just 1.6 ns [74]. This property makes them good candidates for timing applications. However, they are not dense materials. EJ–232 has a density of 1.032 g/cm^3, 7 times lower than inorganic scintillators. A meta-scintillator formed by layers of LYSO and EJ–232 might be capable to still stop a significant number of gamma rays, enhancing timing capabilities by means of energy sharing processes. That is electrons that comes from a LYSO layer can get to the plastic ones and scintillate producing light that arrive faster to the photosensors [75].

2. OBJECTIVES/GOALS

1. Characterization of a prostate PET system based on monolithic scintillators. Study the best geometry that optimizes the final image quality. For this purpose, both point and extensive sources will be used.

2. Characterization of a cardiac PET system, suitable for measurement with patients under stress conditions. Determination of the optimal geometry of the detector module, and implementation of an optical system for monitoring the movement of the patient with high precision.

3. Characterization of a preclinical PET system composed of a single cylindrical scintillation crystal. The characterization will be carried out both by Monte Carlo simulation and experimental data.

3. TECHNICAL DEVELOPMENT

3.1. Simulation

A considerable part of this thesis is based on simulated data. Nowadays, simulation toolkits have become crucial in the design of experiments not only for Medical Imaging, but also in nuclear or particle physics, space engineering and others. Back in 1998, two independent groups, at CERN and KEK, also known as the Japanese organization “High Energy Accelerator Research Organization”, were interested in applying current computing algorithms and techniques to predict the performance of High Energy Physics detectors [76]. Geant4 (for Geometry and Tracking) simulation toolkit was born as a collaboration of many experts when searching for a software that permitted including new physical processes to previous toolkits. They were able to include characteristics such as:

4. System geometry: Shape and size of the detectors, including spherical shapes, cubes, cylinders and other possible configurations.
5. Fundamental particles and their interactions with the matter: electrons, protons, positrons, and many other particles. It included cross section tables of each particle for wide energy windows, from few eV to TeV. It also accounted for the generation of primary particles resulting from particle-matter interactions.
6. Precise particle tracking within the materials, including in the presence of magnetic fields.

7. Geometry visualization of volumes and particles.

Geant4 is a robust and compact platform that can handle several simulation architectures. Notice that for medical application there is no need of employing all the libraries and tools as in PET the energies are around 511 keV. Geant4 Application for Tomography Emission (GATE) is a Geant4 interface, made by an internal association called OpenGATE collaboration, that compiles all the necessary libraries for the field of molecular imaging [77]. By the time this thesis was developed, there existed until 9 versions of this platform. GATE makes use of ASCII scripts that are later transcribed as an input for the Geant4 core, generating lists of data that can be processed for imaging or other applications such as dosimetry. Depending on the scanner geometry or the type of particles, different macros have to be developed with its corresponding architecture. These systems are indeed templates of predefined geometries designed to facilitate the simulation structure.

In this work, through the use of the GATE platform, a complete study of the scintillation light dispersion and collection has been carried out for several detector configurations. Optical simulations of scintillation processes were also performed for diverse detector configurations, types and treatments. A different number of full PET scanners, including pre-clinical and organ-specific systems, have been characterized. We have studied the multiple interactions and energy depositions that occur in PET detectors. Nuclear and optical simulations present some particularities in terms of the geometry and the material properties that must be defined. Also, the simulation output data is different and should be processed in a different way. These will be discussed in the next sections. For illustration, Figure 15 left shows the nuclear simulation of a PET systems based on monolithic crystals and, on the right side, the optical tracing taking place in one of these detectors.

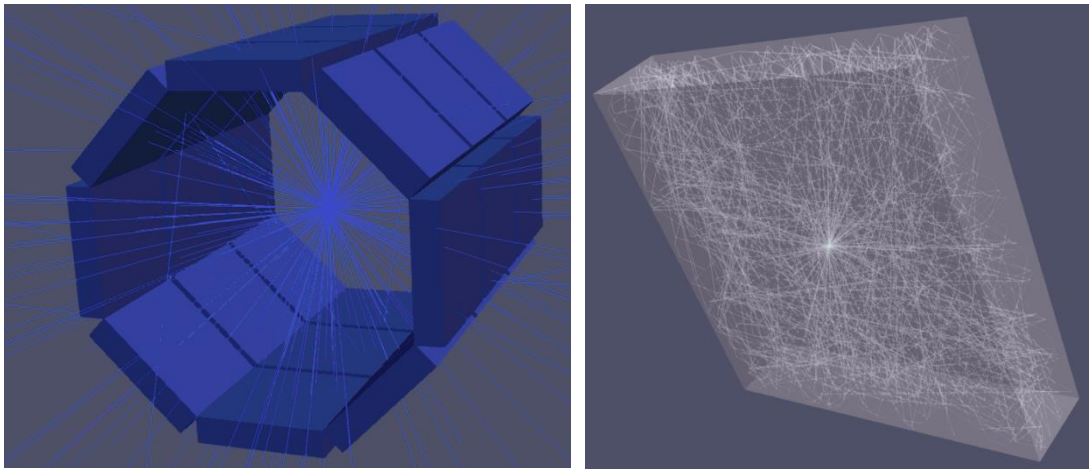

Figure 15. Left: Sketch of a nuclear simulation for the Albira PET system showing 3 rings of 8 detector blocks each one. Right: Optical simulation of a single LYSO monolithic block.

3.1.1. Nuclear simulation structure

MI systems, such as PET or SPECT, collect a high number of gamma rays in the detectors. Once enough data have been recorded, events are listed and can be used to extract relevant information as an input for the reconstruction process. The aim of nuclear simulations is to generate data of the interactions of the gamma rays with the sensitive volume of the detectors. Prior information of the detector blocks must be known or experimentally estimated, such as the energy and time capabilities. Materials must be specified as a function of elemental atoms, either specifying the molar fraction *f* or the number of atoms of each element. As an example, LYSO and BGO can be introduced as follows:

```
BGO: d=7.13 g/cm3; n= 3 ; state=solid
        +el: name=Bismuth    ; n=4
        +el: name=Germanium  ; n=3
        +el: name=Oxygen     ; n=12

LYSO:   d=7.15 g/cm3; n=4 ; state=Solid
        +el: name=Lutetium   ; f=0.674
        +el: name=Yttrium    ; f=0.041
        +el: name=Silicon    ; f=0.074
        +el: name=Oxygen     ; f=0.211
```

Given the material properties and the energies of the particles, GATE can calculate the energy deposition within the material by using libraries of cross sections. Due to the nature of the high energy of annihilation photons (511 keV) and the effective atomic number of the typical scintillation crystals, it is expected to register a significant amount of Compton (inelastic dispersion) interactions compared to pure photoelectric cases. In PET imaging, this causes a non-negligible image blurring if not properly addressed [78].

The geometry of the detectors plays an important role for the GATE hierarchies. Besides of an accurate description of the detector modules, the shape, localization, and material of all the other structures, as the patient bed or possible shielding, would affect the result of the simulation. Thus, it is important to accurately define all the volumes. In this thesis, according to the kind of scanner to be studied, two crystal arrangements were employed, one follows the ring configuration and the second the panels system, see Figure 16.

Each interaction of the annihilation photons within the detection area is an elemental piece of simulation information and it is called hit. One hit contains multiple information, such as the track event number, the total energy deposited in the volume, the timestamp and the global coordinates. With the event number, it is possible to establish if two different gamma rays come from the same positron-electron annihilation or if they suffered Compton scattering before

Photoelectric. In the case that our detector presents an ideal performance, with no uncertainty in the energy nor the time and position, the registered position would match with the hit. Unfortunately, this situation does not happen in real experiments since detectors exhibit some limitations and trade-offs. Thus, GATE employs the digitizer module that allows blurring the hit information becoming more realistic [79].

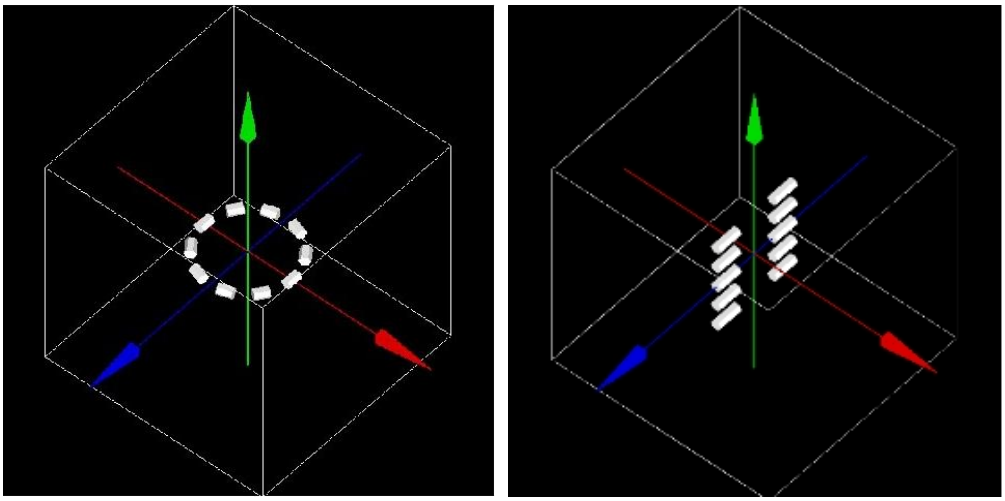

Figure 16. Left: Example of a ring with the GATE simulation platform. Right: Same for a panel system

All the hits that are marked by the same event tracker are grouped in a single event. The coordinates of a single event can be calculated with a CoG of all the positions of the hit weighted for instance with each energy deposition. The total energy of a single event would be the sum of all hits. A gaussian blurring can also be added to the energy and timing information, if desired. Coincidence events are generated when two singles have occurred within a time window defined by the user, typically of some nanoseconds. The time window should not be lower than the expected time resolution. Ideally, coincidence events should belong to the same annihilation process, however there might occur random and multiple coincidences, especially for large activities.

Aside from the energy, spatial and time resolutions, GATE allows to introduce other parameters to make a more realistic modelling of all processes, such as the system deadtime or pile-up capabilities. These effects play an important role for high activity sources [80][81]. Detector deadtime depends on the electronics performance and the gamma ray flux that interact within the scintillator volume. Notice that the scanners need a determined time to process the data, making the detector blind to collect other particles arriving in this interval. The deadtime can be characterized using two models; the non-paralyzable, where the processing time is constant and does not extend with other hits, and the paralyzable where the time delay concatenates multiple processing times. If during the processing time, some pulses (new interactions) form different events enter in the same integration window, the system can

account for pile-up effects. Here, the resulting pulse would be the sum of both events, not allowing one to properly distinguish among them and, thus, producing an additional sensitivity loss. Deadtime and pile-up definitions are exemplified in Figure 17.

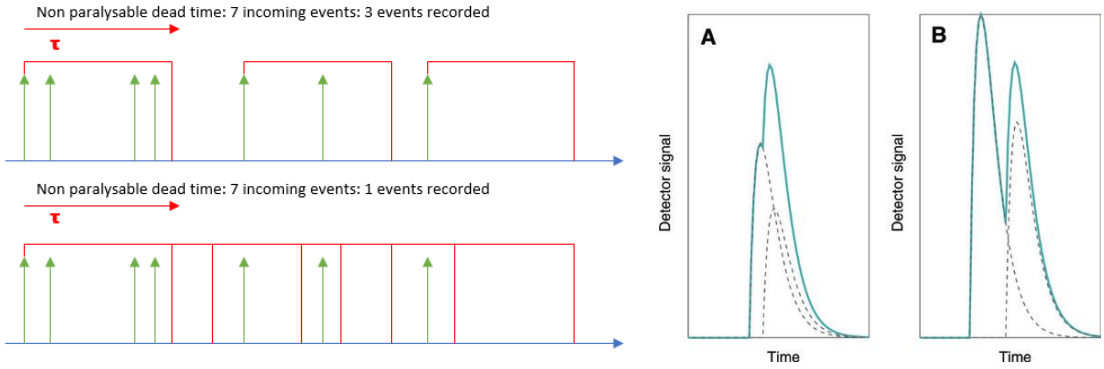

Figure 17. Left: Deadtime schemes for paralyzable and non-paralyzable electronics. Right: Example of pile-up events.

3.1.2. Optical simulation structure

In a detector module mainly defined as a scintillation block and a photosensor array, many factors can be optimized to achieve accurate performance capabilities. GATE employs Geant4 optical libraries reproducing the scintillation light spreading properties with high precision. Material and surfaces properties must be specified with details. For materials different from scintillators, the most important parameter is the Refractive Index (*n)* which defines the optical photon speed within the material as a function of its energy, typically some eV. Each time the photon reaches the surface that separates two different materials, with different *n* value, light propagation, transmittance, and reflections will be determined following the Snell law [74][82][83][84]. Some refractive indexes for different materials used for simulations are shown in the Table 1 below.

Material	Refractive Index
LYSO	1.81
BGO	2.15
EJ-232	1.58
Optical Grease	1.50
Air	1.00

Table 1. Refractive index for different materials.

There are several parameters one must introduce regarding the scintillator definition. The Light Yield (LY) is the average number of OP generated as a function of the deposited energy of the particle. The LY of LYSO is about 32000 OP/MeV, whereas for BGO or plastic scintillators is around 8400 OP/MeV. GATE models the scintillation pulses as the sum of two exponential distributions, a fast-rising component plus a slow decay one. A further step is the definition of

optical surfaces such as the detector treatment or the geometry and type of the photosensor device [79].

The scintillation light collected at the different photosensor elements helps to characterize the LD, especially for monolithic blocks. As introduced before, the preservation of the LD allows one to estimate the 3D coordinates namely planar XY and DOI. If the defined surface separates two dielectric materials, such as the air and the scintillator block, OP will undergo total internal reflections. Notice that reflection and refraction properties depend on the energies of the OP and incidence angles, among other factors. GATE models the reflection type with a proportion of Lambertian diffusion. Teflon coverage, specular reflection for ESR materials and other combinations can be modelled by changing these properties. It is also possible to define surfaces that bounce back the light into the emission point, already introduced as RR.

In order to emulate the SiPM performance, an important parameter is the so-called *Efficiency* referred to the PDE, which is also a function of the OP energy [86]. This gives the probability of detecting an OP that reaches the SiPM. In Table 2, PDE values are shown together with the emission spectrum of LYSO and BGO [85].

Energy OP (nm)	LYSO Emission (%)	BGO Emission (%)	SIPM PDE (%)
609	0.000000	0.078	0.25
550	0.062500	0.230	0.32
480	0.265625	0.385	0.40
430	0.390625	0.230	0.37
400	0.234375	0.077	0.35
370	0.046875	0.000	0.30
350	0.000000	0.000	0.10

Table 2. Optical properties for different materials.

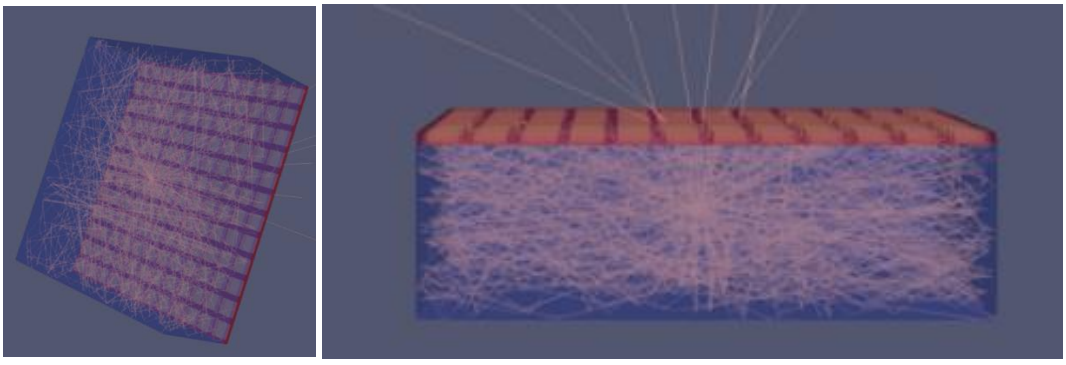

Figure 18. Left: View of a monolithic block coupled to a SiPM array. Right: Same but showing the XZ plane.

For illustration, we show examples of optical simulations (GATE) based on a monolithic scintillator block made by own group, sketched in Figure 18, where a photoelectric event has occurred at the center of the crystal, producing OP. The block is of LYSO type and has dimensions of 50 × 50 × 10 mm^3, coupled to a 12 × 12 SiPM array in the XY plane. The photosensors have a

pitch of 4.2 mm and an individual active area of 3 × 3 mm^2. First tests considered all surfaces black painted, except the one in contact to the photosensors. For these black surfaces, the 95% of the impinging OP are absorbed, and the rest are randomly reflected. Additional tests using Teflon wrapping around the scintillator laterals were carried out, where all the Ops are reflected following Lambertian diffusion. In a third test we considered lateral surfaces black painted, but the entrance surface included a RR layer. A source of 16000 OP (LYSO emission for an impact with 511 keV energy) has been placed at the center of the crystal volume, isotropically emitting scintillation light. The scintillation light was projected onto one axis, to study the light distribution performance. For the case where all walls were black painted (labelled as Black) there is no light reflected in the scintillator surfaces and, thus, just the light directly coming from the emission point reaches the SiPM array. A total of 672 optical photons were registered in the photosensor surface. For the Teflon case, the total counts increase to 2040 but a background pedestal appears. Finally, the combined choice of RR and lateral black paint preserves the distribution shape but with a higher light collection registering 1428 counts. Different DOI positions were simulated to observe how the LD would vary. These light distributions can be observed in Figure 19. The aim of these simulations was to compare the light collection and the shape of the distribution for all situations, which will be very important in order to select a kind of detector. Even when the black surface situation preserves the LD, light collection is poor in comparison with other situations

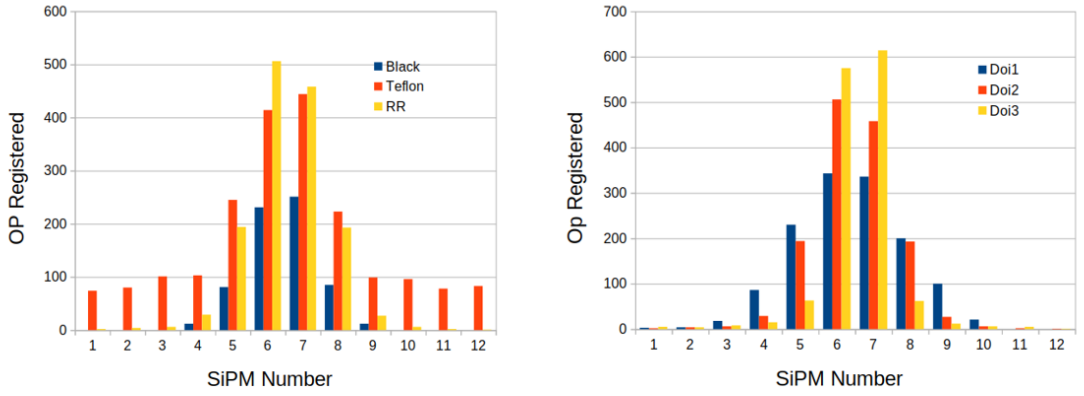

Figure 19. Left: LD projections in the X plane for different crystal treatments. Right: LD projections for the RR case but for events at different depth of interactions.

The difference of light collection for Black and Teflon is more evident when both energy spectra are compared, as shown in Figure 20 left. The difference is due to the Lambertian diffusion in the Teflon situation, which leads to a major number of OP registered for a same scintillation process. Once each LD is properly stored, the impact coordinates in the XY plane can

be estimated. Analytically one can make use of the CoG or Rise to Power (RTP) algorithm [54], among others. The mathematical expressions for CoG and RTP, are as follow:

$$X_{COG} = \frac{\sum_i^n n_i X_i}{\sum_i^n n_i} \quad (1)$$

$$X_{RTP} = \frac{\sum_i^n n_i^j X_i}{\sum_i^n n_i^j} \quad (2)$$

Here, n is the number of rows or columns, X_i their position, n_i the registered counts for this position and j the rising power. There are other methods, out of the scope of this thesis, that can also be applied such as Maximum Likelihood Estimation Maximization (MLEM) or Machine Learning, to name but a few [87]. Since the scintillation block is not an infinite object, for impacts closer to the crystal edge the LD truncates and, therefore, the impact position estimation (CoG or RTP) will be biased. This effect becomes worse for impacts occurring at the crystal entrance due to the wider LD.

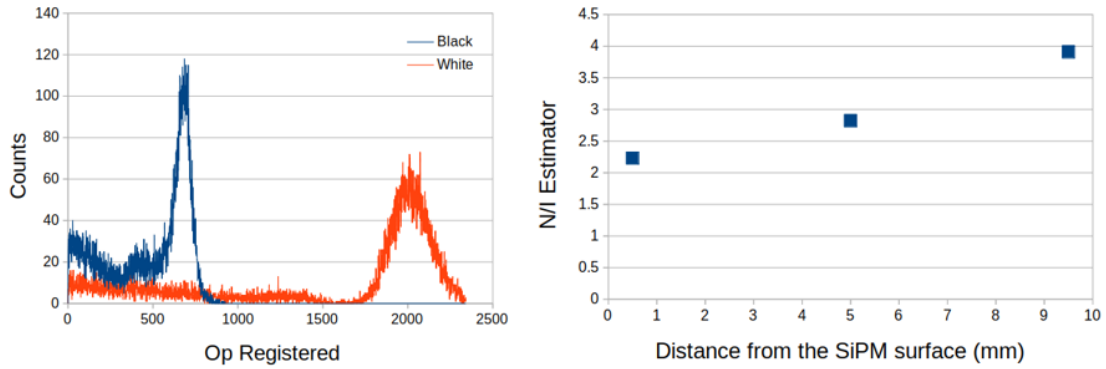

Figure 20. Left: Energy profiles according to the surface treatment applied to the crystals, black surface (blue) and Teflon (orange). Right: N/I dependence with the distance from the impact to the SiPM, for three DOI cases when using black paint.

The LD width is a good estimator for the depth of interaction coordinate. The ratio between the total OP registered (N) and the maximum value of the projected LD (I) is considered as a good estimator of the LD width and, therefore, it can be used to estimate the DOI, which its relevancy will be explained in section 3.3.3. Figure 21 right shows the N/I dependence with the distance from the photosensor plane for the aforementioned simulated crystal with all surfaces black painted. In Figure 21 left, the data compression of the black crystal case is shown for different DOI positions (Z axis). This example is for a LYSO crystal block with 50 × 50 × 20 mm^3 dimensions. This effect increases for a Teflon surface case due to the high light dispersion and the tails of the LD, see Figure 21 right. RTP partially mitigates this effect.

One of the handicaps of optical simulation is the processing time in comparison with the nuclear. For each nuclear interaction that deposits some energy in the volume, a high number

of OP photons are generated and tracked (about 16000 for a 511 keV gamma ray). Such a computational cost must be considered when designing an optical simulation. The general method usually consists in a previous optical study of one or few detector modules, extract parameters such as the energy or spatial resolution, and then extrapolate to a nuclear system simulation adding blurring parameters. Nevertheless, during this thesis a complete optical and nuclear simulation study of novel PET system geometries has been carried out.

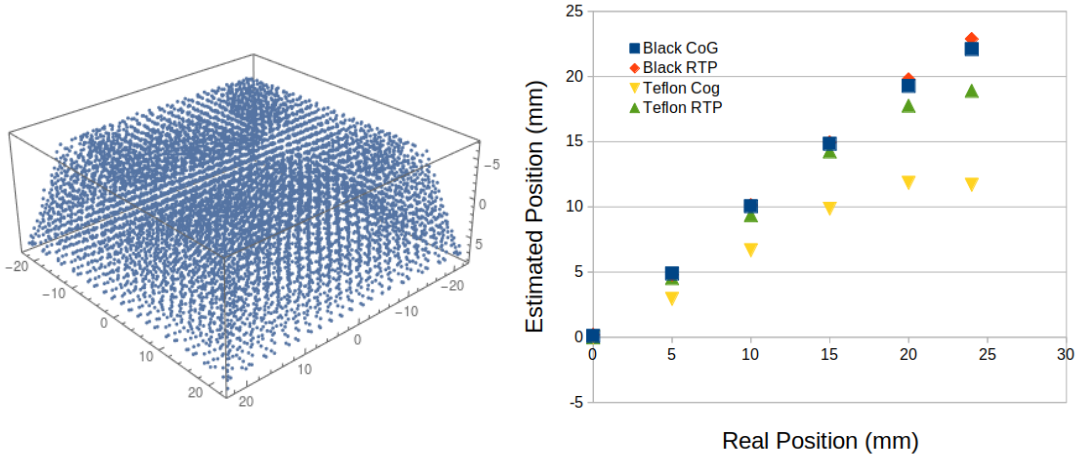

Figure 21.Left: Calculated positions applying CoG for different DOIs in a 50 × 50 × 15 mm³ block. Right: Light compression according to the surface treatment and the employed algorithm.

3.2. Reconstruction

When the first PET systems were developed, several analytical and iterative algorithms were implemented and tested to enhance an accurate quantification of the imaged molecular processes [88]. As earlier introduced, the PET image is generated by all LORs that pass through the FOV. Notice the term LOR is an especial case the so-called Tube of Response (TOR), a more general concept, where instead of a simple line, both events that form a coincidence are connected with a parallelepiped which base is related with the detector spatial resolution [89]. The intersection of the LOR (or TOR) with an image voxel is calculated with a projector. For instance, the Siddon projector directly computes the length of the LOR that passes through a voxel. Other types of projectors use interpolation techniques [90].

There are mainly two ways of storing the data depending on the reconstruction algorithm, namely sinograms or List-Mode (LM). A sinogram is a representation where the information is reduced to the distance between the LOR and the FOV center, and the orientation angle respect to the axial axis [91]. In Figure 22, a sinogram representation is showed where the LORs, labeled as A, B, C and D are represented and transformed. This is useful to identify possible image

artifacts. In the LM storing, the coincidence events are listed, typically sorted with their timestamp (time information of the arrival event).

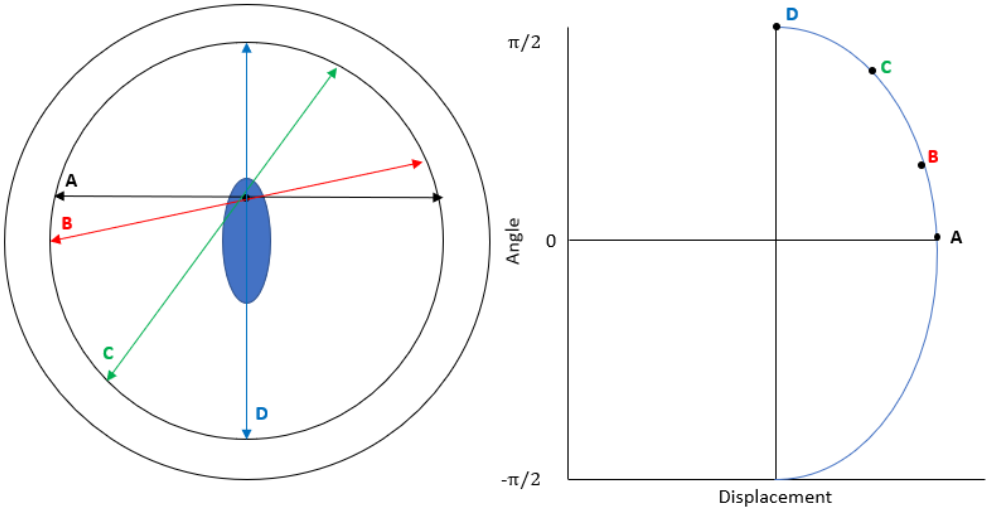

Figure 22. LOR characterization in a PET scanner (Left) and corresponding sinogram points (Right).

Two examples of sinograms have been calculated for the small animal PET Albira [55] for a spherical source at the FOV center and for the same source but shifted 10 mm in the radial position, see Figure 23 top and bottom panels, respectively.

The reconstruction algorithms for PET are typically divided in two groups: analytical and iterative [92]. Analytical methods presume that PET data is not stochastic: it does not account for phenomenon such as statistical noise, non-collinearity of gamma rays, positron range, etc. A projection is defined as the line integral along all parallel LORs at a certain angle. If we define the final image as a matrix *f*, the relation between this and the set of projections *p* is established as the imaging system *H*, defined by the projector.

$$p = Hf \tag{3}$$

The most common analytical algorithm is called filtered backprojection (FBP) [88]. NEMA protocol requires its use to compare different PET scanners performance, due to its analytical approach. FBP is a fast algorithm and rather easy to implement. FBP collects all the projections, of each pair of detectors, to the image space and then integrates all the contributions. This is the reversal process of the forward projection. Due to the stochastic nature of PET data, the produced images are typically noisy and, thus, some filters such as a smoothing must be applied. Figure 24 shows, step by step, how the total combination of projections leads to a tomographic 2D image of a spherical source. Furthermore, this method is not accurate for PET geometries different than standard ring configurations.

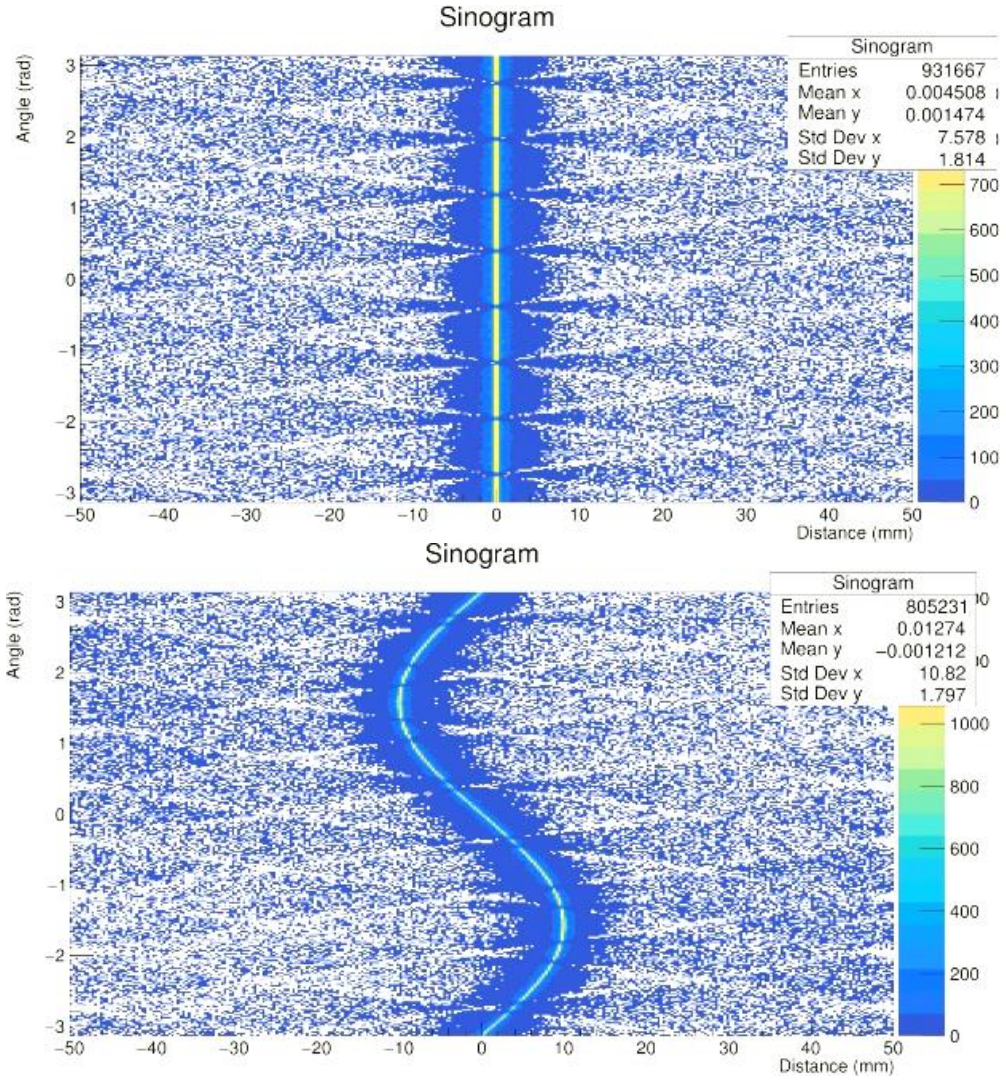

Figure 23. Top: Calculated sinogram for a centered FOV source, in the Albira pre-clinical PET system. Bottom: Sinogram for a source shifted 10 mm in the radial direction.

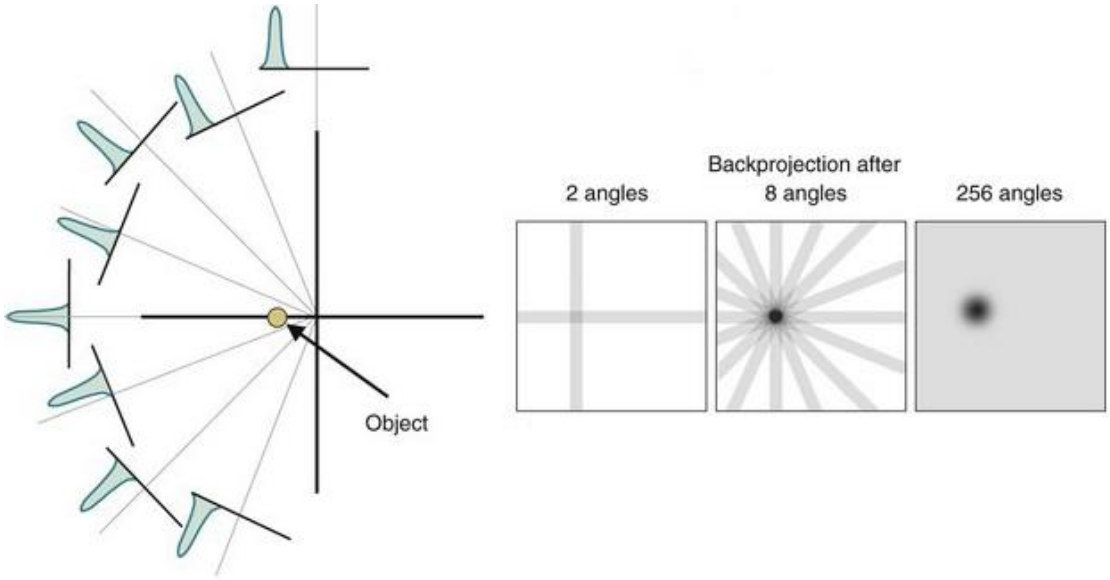

Figure 24. Forward projection scheme. When all the projections are considered, the spherical source is recovered (www.radiologykey.com).

In contrast to analytical methods, iterative approaches consider the non-deterministic nature of PET data [93]. Including all the physical processes in the reconstruction deals with very complex, and memory demanding, algorithms which cannot provide a direct analytical solution. This kind of reconstruction begins with an initial approximation of the expected final image, typically a matrix with all zeros or a uniform distribution. First it compares this initial approximation with the measured projections. If the results do not match inside an acceptable error, this process iterates until the solution is optimized within a criterion. Least square (LS) principles that consider the results-projection difference using the Euclidean distance is one of the possible criteria. Nevertheless, the most extended criteria these days is the Maximum Likelihood (ML) that maximizes the likelihood function. On the other hand, EM algorithm is a classical algorithm to work out a non-complete data problem. The combination of EM with a Poisson type ML results in the equation below, known as MLEM [94].

$$H = H_{sensitivity} H_{blur} H_{attenuation} H_{geometry} H_{positron} \tag{4}$$

$$\hat{f}_j^{(n+1)} = \frac{\hat{f}_j^n}{\sum_{i''} H_{i'j}} \sum_i H_{ij} \frac{p_i}{\sum_k H_{ik} \hat{f}_k^{(n)}} \tag{5}$$

Starting with the initial estimation f_0, MLEM uses the ratio of the estimated and measured projections. This process iterates with the help of some weight factors until it converges to the ML solution. While this method is robust, it also presents some drawbacks. It often requires the use of a filter in order to smooth the noise produced in the reconstruction algorithm. Due to the produced noise, the convergence is typically slow. It usually demands more than 30 iterations to obtain an optimal image. An alternative reconstruction method that reduces the processing time and memory consumption is the Ordered Subsets Expectation Maximization (OSEM) [95]. This method splits the data into subsets, or partitions, and then applies the MLEM approach. The MLEM approach is sketched in Figure 25.

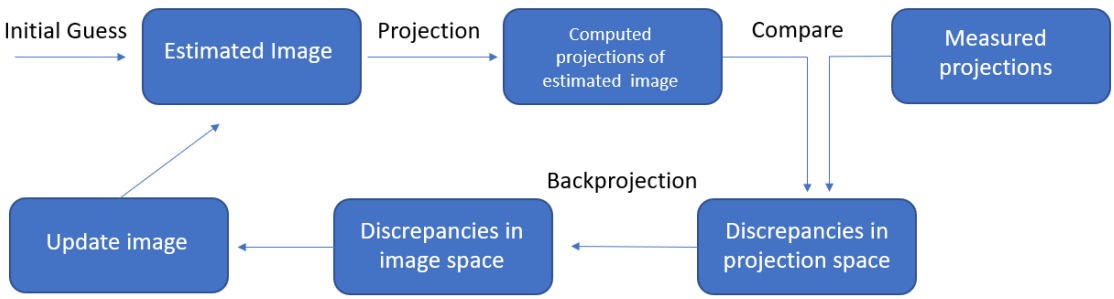

Figure 25. Principle of an iterative reconstruction method. The loop will run until it converges to the ML solution.

The open-source reconstruction platform called CASToR (Customizable and Advanced Software for Tomographic Reconstruction) [96] has been used to reconstruct most of the images shown in the dissertation. This platform allows one to also handle non-conventional PET system configurations, and the possibility of introducing custom made projectors and algorithms. A Look Up Table (LUT) file can be generated introducing the detector position in the space with no need of a specific classical configuration. For instance, in a multi panel system and preclinical prototypes, that will be all extendedly introduced in Section 4, we integrated CASToR using a LUT geometry file. Moreover, the ring configuration is introduced with a generic macro that the platform allows to modify. It is mandatory to introduce a virtual pixelization, which size depends on the intrinsic spatial resolution of the detector in the monolithic situation or directly the crystal size in the case of pixelated arrays. The platform is able to reconstruct the data, which can be effectively introduced as a sinogram or a LM file.

CASToR has been employed by multiple research studies. For instance, it has been used in the reconstruction of a plant-specific PET scanner called BioPET [97]. Regarding scanners oriented to human patients, a system called Philips Vereos DPC-PET with LYSO pixelated crystals of $4 \times 4 \times 19$ mm^3 and a FOV size of 764 mm diameter with 164 mm axial length was simulated, using CASToR to reconstruct images [98].

3.2.1. Image reconstruction corrections

Some corrections are needed to provide an accurate and quantizable reconstructed image. In Figure 26, a sketch with some PET image correction is illustrated. The coincidence detection efficiency that varies depending on the geometry of the system, as well as possible differences in the electronics of each detector module [99]. To illustrate this, if detectors would exhibit different gains in the OP collection (due to the crystal light yield, photosensor gain spread, coupling, etc…) they might produce image artifacts. These effects are mitigated with the normalization correction. This correction is typically carried out using a phantom with a cylindrical shape such that all LORs of the scanner geometry are passing through this [99]. The efficiency differences are kept in a normalization file as well as the difference of the sensitivity according to the position within the FOV, compensating all the artifacts.

An alternative technique for normalization correction with a significant less scatter contribution, is an annular phantom where the activity is concentrated in such ring only [99]. Considering each LORs length as a multiplication factor for each voxel it is feasible to reproduce the normalization map with much less scatter contribution this time. Normalization data is reconstructed with the same number of voxels and dimensions that the final image. In Figure

27, the normalization map (real data) obtained with an annular phantom is shown. See details in 4.1.4.

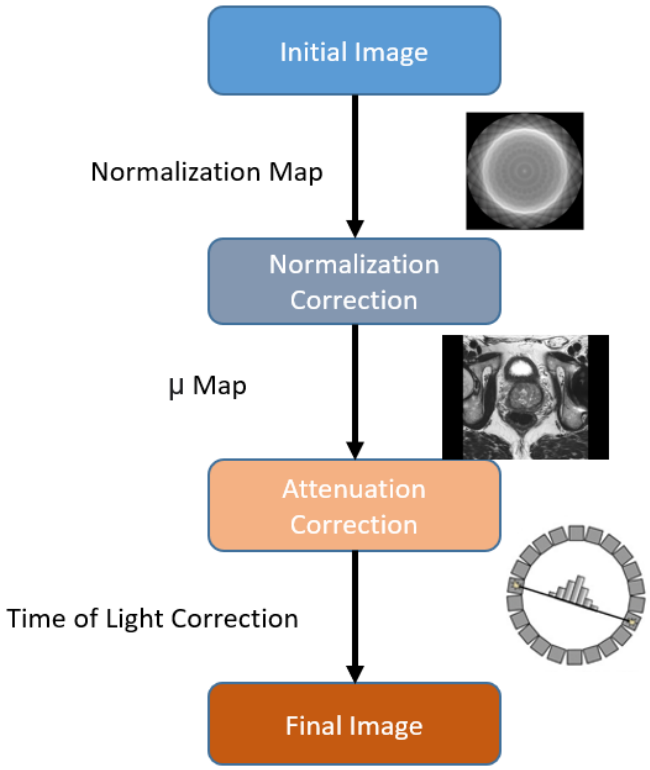

Figure 26. Image corrections scheme including the normalization following by the attenuation and the Time of Light.

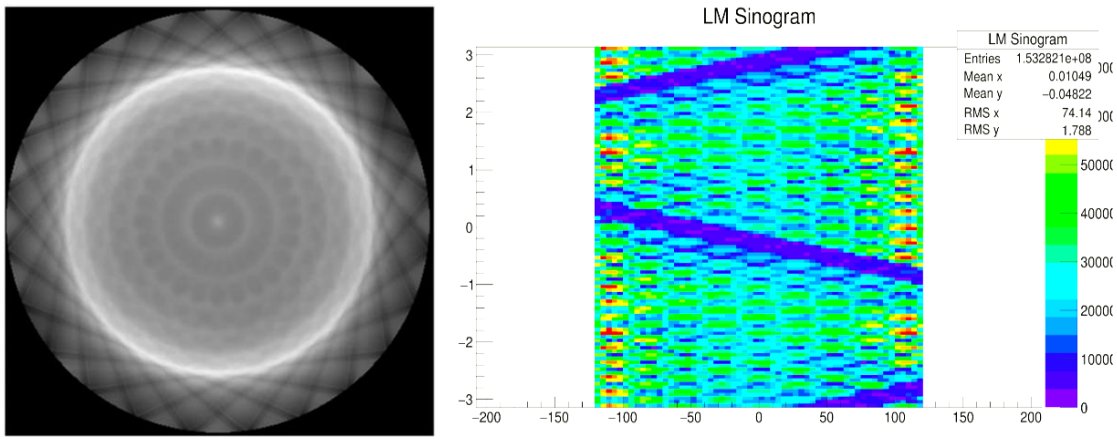

Figure 27. Left: Normalization map of a PET ring configuration. Right: Sinogram of the normalization data.

Gamma rays that pass through the body suffer from attenuation, scatter, and other effects, affecting the registered events on the detector. The attenuation correction takes into consideration the total path that the LOR has crossed with the probability of interaction of the annihilation photon depending on its energy and the attenuation coefficient (μ) of the material. An attenuation map must be provided to the reconstruction algorithm in order to compensate these effects. Figure 28 shows a scheme of the attenuation correction process by introducing an

attenuation mask. It is convenient to use the information of a CT or MR scanner to generate the attenuation mask [100].

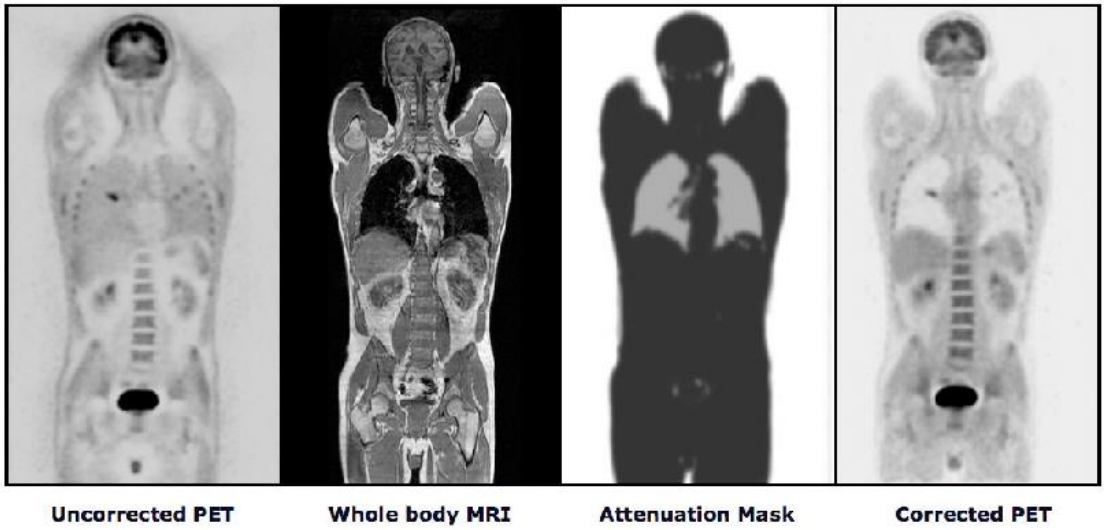

Figure 28. Attenuation correction for a PET system. First image of a raw PET image without attenuation correction. Next, a Whole-Body MRI image that will be used for the attenuation mask, which is the consecutive picture. Lately, by applying the attenuation mask, the corrected PET image can be calculated [101] .

In a PET image reconstruction, scatter and random events need to also be properly addressed . Notice that these two effects have not been considered in the reconstruction processes carried out within this doctoral thesis. The scatter correction makes use of the energy spectrum that comes from the LM data in order to estimate the percentage of scattered events. This correction is usually supported by simulated data. Random corrections consider the singles rates of every pair of detectors as an approximation.

3.2.2. TOF Algorithms

On the assumption that the scanner time resolution is poor, conventional PET reconstruction algorithms cannot predict with precision where the positron-electron annihilation process has occurred, so they will use the entire LOR length in the process. However, if accurate time resolution is provided, there is no need of using the total length of the LOR and thus, algorithms can replace it with a Gaussian distribution centered in the approximated annihilation point, optimizing this way the spatial resolution and the SNR of the reconstructed images [104]. The detectors time resolution directly impacts the Gaussian width and, therefore, the quality of the final image. This process is called Time of Flight (TOF), and many PET scanners which use pixelated crystal arrays can incorporate it, enhancing its performance. A comparison of the Siemens TOF PET/CT mCT and its predecessor, the scanner Biograph TruePoint, was performed by B.W. Jakoby reporting a 20% sensitivity improvement [105]. In Figure 29, the application of TOF algorithms is depicted.

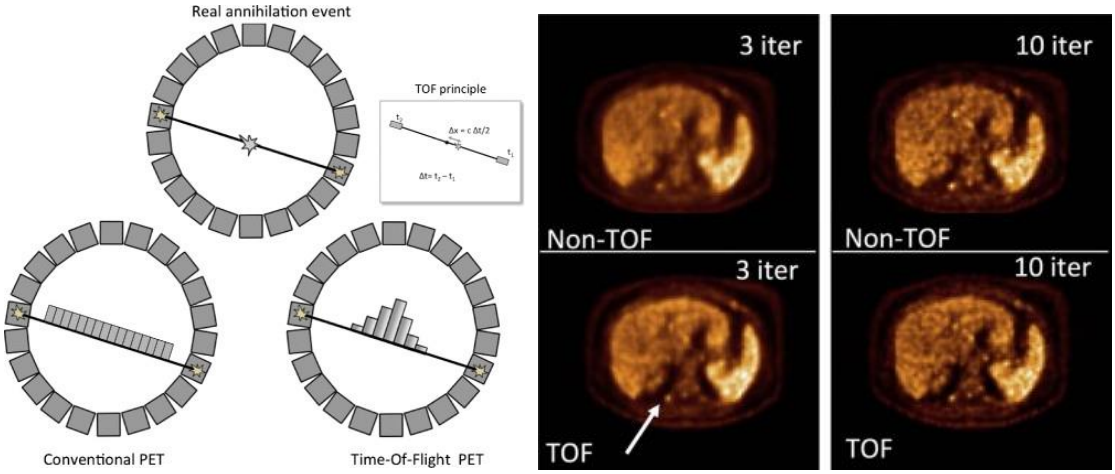

Figure 29. Left: TOF algorithm correction, where a complete LOR is replaced with a gaussian distribution, scheme. [69] .Right: PET image before and after the TOF processing.

In organ dedicated PET scanners, the open ring configuration is an interesting approach in which the detector modules are placed closer to the patient in comparison with classical ring configurations. An example of this system can be appreciated in Figure 30, a PET scanner with two symmetrical panels that will be introduce later. One drawback of the appearance of a very characteristic artifact in the reconstructed image. This artifact is an elongation in the axis that joint both parts of the scanner. It is possible to partially correct this effect with the addition of TOF information, if the CTR is good enough, see Figure 30.

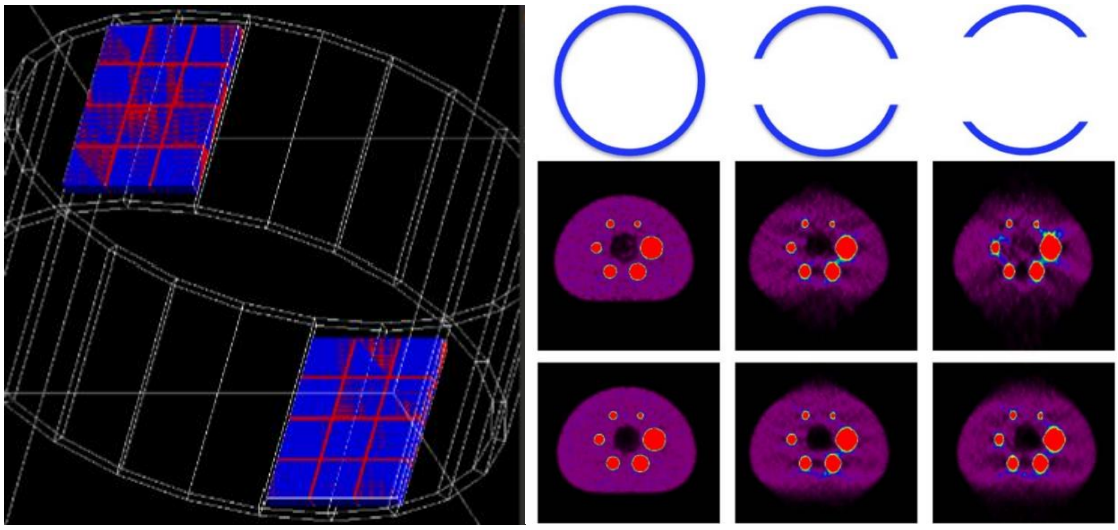

Figure 30. Left: Sketch of an open ring PET scanner composed by two panels with 12 detector modules each. Right: Three PET configurations showing two levels of open ring degrees. The first row of panels depicts the NEMA image quality phantom without TOF reconstruction. The bottom row of panels exhibits the same images after considering a TOF algorithms with 545 CTR.

3.3. PET performance procedures

Novel gamma ray instrumentation both electronics and photosensors, combined with new radiotracers and other technological aspects, have made possible a significant improvement of PET performance since the 70s decade. The aim of specific PET systems, organ-dedicated, is to reproduce, or even overcome, conventional WB-PET performance, but at a reduced cost. The aim of this thesis is to show the capabilities of some organ-specific systems, especially with novel geometries. In order to illustrate this, system characteristics such as sensitivity, noise equivalent count rates (NECR), or spatial resolution, have been studied based on NEMA [106]-[109] protocols.

3.3.1. Sensitivity

The sensitivity reflects the amount of true LOR events that the system can collect, without scatter and random coincidences included. It is defined as the ratio between the total number of coincidences measured and the total annihilation gamma rays emitted by the source. The use of a low activity source avoids random events. Independently of the activity, a minimal number of 10^4 coincidence events are recommended to be collected, to decrease the statistical uncertainty. According to the NEMA NU 2018 protocol [109], a linear source must be used. Sensitivity values are shown across the whole axial FOV of the PET scanner. For preclinical systems, following the NEMA NU 4 – 2008 protocol [107], a small size source can also be used as an alternative. The sensitivity depends on two factors, geometrical and intrinsic. Geometrical factors consider the solid angle that is covered by the PET system for gamma rays that are isotropically emitted. The intrinsic factor, however, relate the probability of the photon interaction within the scintillation crystal, and depend on the crystal size, material, and annihilation photon energy.

3.3.2. Spatial resolution

The spatial resolution of a PET scanner shows the ability of the system to distinguish two source points after the reconstruction process. It is a complex parameter that depends on multiple variables. It strongly varies with the detector intrinsic capabilities such as spatial resolution, energy resolution and size. It is a function of the specific reconstruction algorithm (analytical or iterative), the number of iterations, the image voxel size, and the LORs size, to name but a few. NEMA protocols establish that the spatial resolution characterization must be carried out with an encapsulated source not larger than 0.3 mm in all directions, and with an activity sufficiently low to avoid random events. It also recommends using FBP algorithms. In order to calculate the spatial resolution, the image voxel size should be adequately reduced so

the source size would fit. The spatial resolution is defined as the Full Width Half Maximum (FWHM) of the PSF (Point Spread Function). No smoothing must be applied.

3.3.3. DOI Correction

Previously, in section 1.2.1, we have introduced the advantages and disadvantages of pixelated and monolithic crystals. As a summary, we have concluded that pixelated crystal arrays, despite their good time resolution, all the light is collected mainly in a single SiPM so LD is not preserved. Monolithic crystals, on the contrary, can recover all the LD as we can observe in Figure 19. LD shape is related with the DOI so we can estimate this value with the width of the distribution as explained in a previous section. DOI estimation plays a crucial role when dealing with the parallax error [51]. If we only consider in the reconstruction process the XY local coordinates of the detector, and the DOI is not estimated as in the pixelated crystal situation, for an electron-positron that takes place far of the FOV center, where the LORs arrive more obliques than in the FOV center, the misalignment of the real LOR and the perceived LOR will become relevant and produce some artifacts in the image, see Figure 31. In the case that the DOI is estimated and hence the correct LOR is computed, the effect is corrected. The parallax error worsens as the LORs becomes more oblique. However, recalculating the XY impact coordinates with the DOI information, mitigates the parallax error.

Parallax error gets more critical in reduced FOVs given that the LORs arrive more oblique. For WB-PET systems, in contrast, they prefer a good timing optimization for TOF correction than DOI estimation. In organ dedicated systems, on the contrary, we work with reduced FOVs as the preclinical scanners, so it is interesting to estimate DOI value with high precision [55]. DOI correction will play a major role in the spatial resolution characterization, and if it is not enabled the scanners performance will be degraded far of the FOV center.

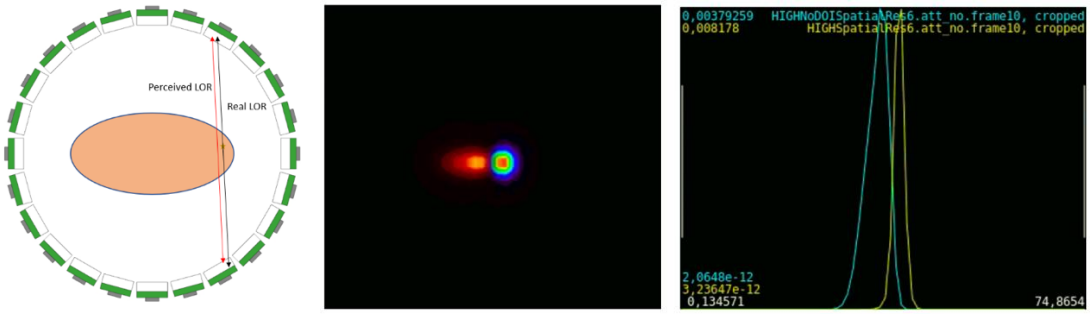

Figure 31. Left: Representation of the parallax error. Center: Reconstructions of a point-like source shifted 20 cm of the FOV center before (red) and after DOI correction (blue) is enabled. Right: Profile extracted from the non-corrected source (blue) and from the corrected (yellow).

3.3.4. Noise Equivalent Count Rate (NECR)

Random and scatter coincidence events might significantly affect the PET scanner performance, including the final image quality. These events depend on factors such as the scanner geometry, the detector electronic configuration or the coincidence time window. Moreover, the deadtime of the detectors and the events pile-up contribute to count losses as well. The estimation of the total count losses and the percentage of random events within the prompts reveals the ability of a PET system to accurately work with high activity concentrations. Increasing the sensitivity by allowing random events to surpass the true LORs might produce poor-quality images [110]. For this reason, the NEMA protocol introduces the NECR estimation, a factor that can be compared between different scanners. NECR values can be calculated following this equation:

$$NECR = \frac{T^2}{T+R+S} \tag{6}$$

T is the true events rate or the total number of coincidence events that comes from the same annihilation point with no Compton deviation. *R* is the coincidence random rate within a timing window, and *S* is the scatter rate. By evaluating the NECR for different activities, two important factors can be found. The first is the NECR maximum value and the second is the activity where NECR is maximized so if we surpass this activity the quality of the reconstructed image will be degraded. At this optimum activity, the True coincidences rate presents a high value and is not yet overpassed by the random rate. With the aim to compare between different PET systems, NECR curves give relevant information of the scanner capabilities.

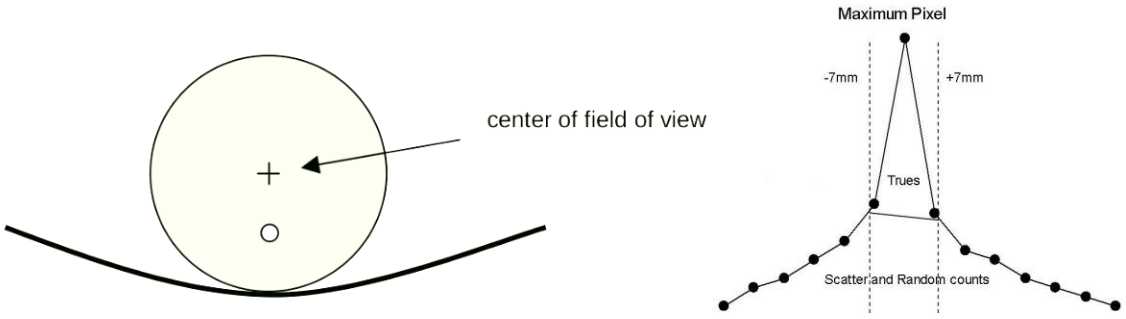

Figure 32. Left: Cylindrical phantom used for NECR calculation. Right: Profile calculated from the phantom acquisition sinogram.

The estimation of the NECR values is obtained with a specific phantom which consists of a cylinder made from high-density polyethylene with a drilled hole shifted off the center where the activity concentration is introduced using a capillary. This phantom reproduces the attenuation of a patient. According to the PET system size, if it is clinical or pre-clinical, the phantom diameter and length would vary. For a pre-clinical PET system, three different

phantoms should be considered according to the kind of animal that fits within the scanner: a mouse, a rat or a monkey. For instance, the NEMA NU 4 - 2008 [107] describes a mouse phantom with a cylindrical geometry of 25 mm diameter and 70 mm length. This phantom is depicted in Figure 32. Focusing on the mouse phantom, the drilled hole is displaced radially 10 mm and its diameter is 3.2 mm. On the other hand, NEMA NU 2 – 2001 [108], the one that is applied for clinical scanners, establishes just one-cylinder size; 203 mm diameter and 700 mm length. The drilled hole diameter is 6.4 mm, and it is placed 45 mm off-the-center FOV.

The procedure consists in introducing a high activity solution of at least 10 mCi of ^{18}F inside the capillary and let it decay several hours. After several semi-disintegration periods, the activity of the source will decrease until true coincidence rates become dominant over scatter and random. Several measurements of short periods of time, in comparison with the semi-disintegration time, must be acquired. Each measurement should be restructured into a sinogram. For every axial slice, the sinogram will present a sinusoidal shape. The maximum value for every angle is forced to be placed at the center and, thus, the original sinogram becomes a single straight line. For each 2D sinogram, the angle component is projected so a 1D graph is generated as it is shown in Figure 32. In this profile, the background distribution accounts for the random and scatter contributions, whereas the peak area represents the true coincidence event contribution. The distribution background increases with the activity. If the background counts are lower than 1% of the total prompts, it is understood that random rates are negligible and scatter coincidences are predominant over the randoms. In this region the Scatter Fraction (SF) is calculated so it can be extrapolated, determining the difference of the random and scatter ratio for every acquisition.

4. CHARACTERIZATION OF SYSTEMS

In this section we will introduce three different PET scanners, two organ dedicated systems and one pre-clinical imager. Their main goal is to boost the performance by increasing the spatial resolution and the sensitivity, improving the final image quality by the use of novel geometries and technology. All simulations and most of the experimental tests were performed within this PhD work, as well as the post-processing of the data and the analysis of the results. In most of the cases the NEMA protocol with some mild modifications has been applied. A dissertation about motion correction approaches is also introduced in this section.

4.1. PROSPET. A specific prostate PET scanner

It is estimated that around 17% of the adult male population will have PCa [111]. This neoplasm has not the highest mortality rate, but still 3.8% die caused by this cancer. PCa might result in urine incontinence and other drawback due to the organ inflammation, see some details in Figure 33. It is recommended to apply an active surveillance routine and periodical tests for all the male population above 40-50 years. The first and fastest test is a rectal examination. Specialists look for tissue irregularities by touching the anal wall closer to the prostate region. Provided that they find irregularities or tissue harshness, a meticulous study of

the tissue is required by means of biopsy methods. Biopsy techniques consist in introducing a rectal needle and take prostate tissue samples on random locations expecting to hit in the neoplasm or the irregularity, see again Figure 33 left. Later all the samples are examined by a pathologist. In order to locate the prostate properly, a transrectal ultrasound (TRUS) probe is attached to the needle. However, this process has only a clinical sensitivity around 60%, more reliable for large and advanced tumors [112][113].

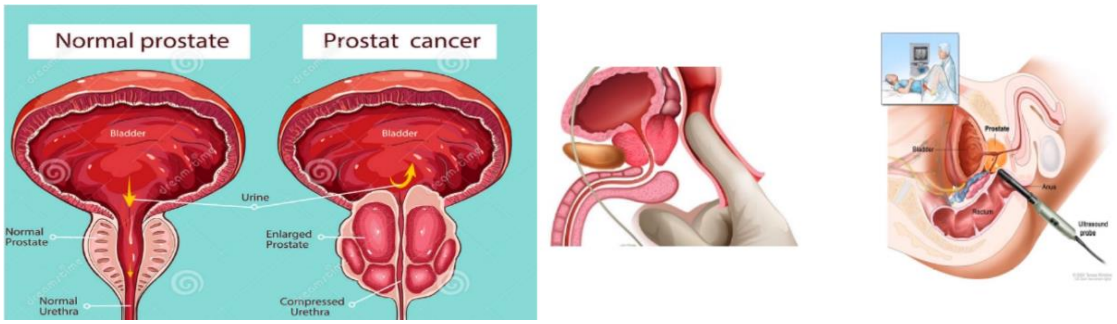

Figure 33. Left: Comparison between healthy and tumoral prostate tissue (www.shutterstock.com). Center: Description of a transrectal test. Right: US guided biopsy. (nurses.uroweb.org).

With the development of new specific radiotracers for prostate imaging, PET imaging can help monitoring PCa diagnosis and treatment. Conventional markers, such as the ones combined with fluorodeoxyglucose (FDG) may not be the best for PCa detection due to the reduced and heterogeneous uptake of glucose. Specific radio markers such as ^{18}F-Choline are better candidates. Other radioisotopes such as ^{68}Ga facilitate generating specific prostate radiotracers that can be processed in the hospital itself. Nevertheless, positron particles generated by ^{68}Ga are more energetic that ^{18}F, so their range will be larger, around 2 mm in water, significantly blurring the final image. The inclusion of the prostate specific membrane antigen (PSMA) [114], combined with ^{18}F and ^{68}Ga, further improves the radiotracer uptake by the prostate tissue. Despite these new radiotracers improvement, WB – PET systems are not the most appropriated for PCa due to their limited spatial resolution. Moreover, WB-PET geometries do not allow the specialists to get close to the patient to carry out a biopsy, so the biopsy guidance using molecular imaging is not feasible.

4.1.1. Detector performance

To overcome these drawbacks, the PROSPET project was launched, that is the development of a prostate-dedicated high-resolution PET system. This project was funded by "*The Spanish Ministerio de Economía, Industria y Competividad*", grant DTS15/00152. The idea was to place the detectors very close to the organ, reducing this way the scanner geometry and improving the PET performance. An additional goal for this prostate specific PET system was to allow in vivo biopsies using MI guidance. The key component of this system was the use of monolithic

LYSO scintillation blocks of 50 × 50 × 15 mm^3 dimensions, with lateral black painted surfaces and a RR film at the entrance surface. 12 × 12 SiPM arrays of 3 × 3 mm^2 area with a 4.2 mm pitch are coupled to the scintillator using optical grease. Some detector performance details can be found in [48].

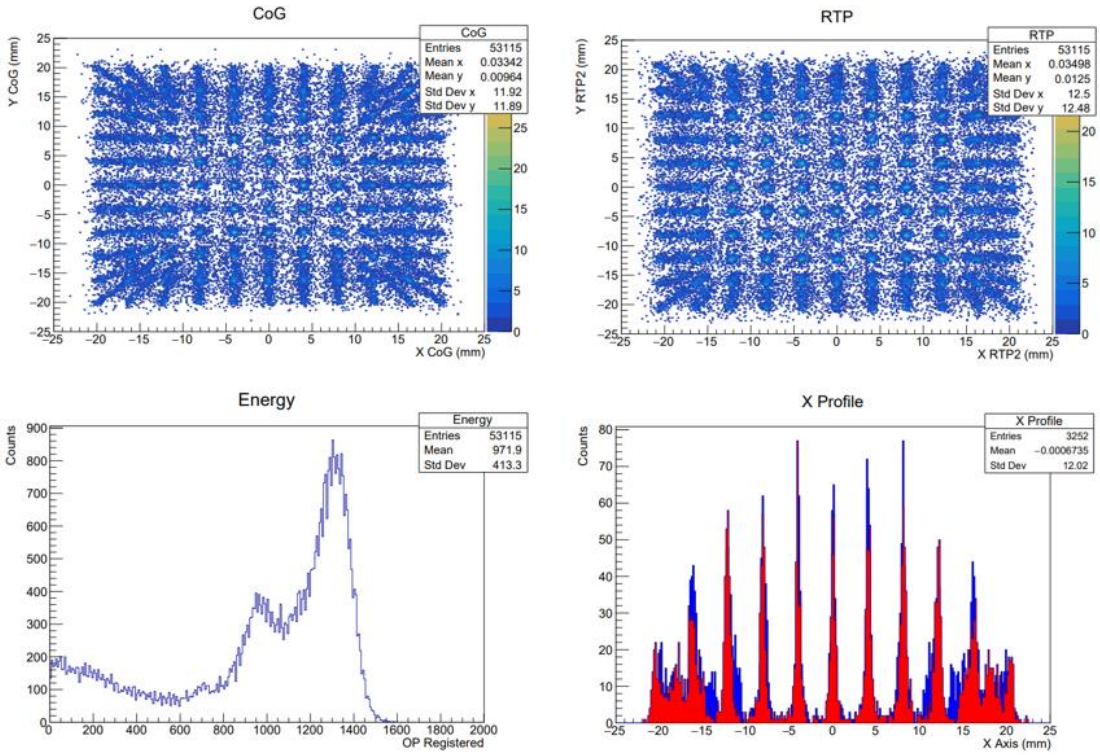

Figure 34. Top Left: Flood map of the 11 × 11 sources using CoG calculation. Top Right: Same as top-left but using RTP2 calculation. Bottom Left: Energy spectrum calculated with the sum of OP resulting 15% energy resolution. Bottom Right: CoG and RTP2 profiles for the central row of sources.

The specifications of the detector blocks have been previously modelled in GATE. We wanted to test the detector performance forcing to scintillate the crystals and evaluate the benefits of this configuration. The 98% of optical photons that get to the RR are bounced back towards the emission source. Energy resolution is calculated with the histogram of optical photons registered at the SiPM, whereas the coordinates are calculated using CoG or RTP2 (RTP of 2) methods for both X and Y axes. Tests have been carried out with 11 × 11 collimated 511 keV gamma ray beams impinging perpendicular to the entrance detector surface. Detector image compression (scintillation light truncation) due to the finite volume of the scintillator is observed in the flood maps for both CoG and RTP decoding. However, RTP exhibits a smaller edge effect, see Figure 34 left. A comparison of CoG and RTP2 profiles are depicted on the top of this figure. According to the results, RTP2 was chosen as the most appropriate algorithm improving event characterization at the edges. In the bottom-left of this figure, we plot the energy histogram with a Gaussian fit, resulting in an energy resolution of 11%. Notice that the LYSO intrinsic resolution has not been included in the simulation. In previous experimental tests,

time resolutions in the range of 2-3 ns were achieved, and this resolution was later included in the simulations. Experimentally, the energy resolution mean value for all the detector volume is 13±0.7%, detector spatial resolution is around 1.9 mm whereas DOI resolution is 3.7 mm [48].

We have simulated and developed different PET configurations, specific PCa imaging. All of these designs make use of the scintillator blocks described above. In the following sections we describe the prototypes that were built and the achieved performances.

4.1.2. Two panels prototype, initial approach. PROSPET1

The design of the first prototype, called PROSPET1, presented a novel and challenging geometry, that is two panels with 12 detector modules each (3 × 4 configuration). Twenty-two MRI images from patients diagnosed with PCa were analyzed determining the average dimensions of the patients in the prostate region abdominal and thickness, resulting on 36 cm and 22 cm, respectively. The distance between the panels was set to 30 cm. All coincidences between the two panels were allowed, generating a XY plane of roughly 30 × 20 cm^2, and 15 cm in Z (axial direction). Figure 35 shows on the left-hand side, a sketch of the detector blocks and panels along with the definition of axes. On the right-hand side of this figure, there is a photograph of the prototype, fully assembled. The gap between adjacent detectors in the panels was just 5 mm (white lines in sketch). This first prototype does not include TOF electronics and thus, TOF algorithms could not be applied so we were expecting some degradation in the final image due to the lack of angular information. Every detector block provided 12 rows and 12 columns of the SiPM array, allowing to characterize the scintillation light distribution. These signals were fed into 12 bits precision ADCs and integrated for 250 ns.

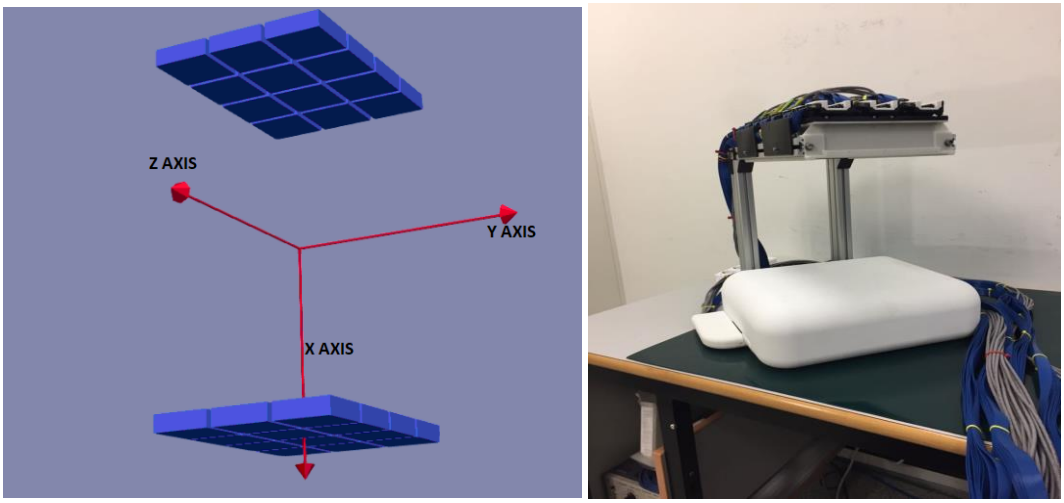

Figure 35. Left: Sketch and position of the detector blocks in the two panels PROSPET1 system. Right: Photograph of the PROSPET1 scanner.

Nuclear simulations were carried out with GATE v9.0, using the detectors information obtained from former experiments. According to the experimental detector performance, the energy resolution was set to 15%. The coincidence time window was set to 5 ns. First simulation tests were carried out with a spherical ^{22}Na source of 1 mm in diameter moved across the axial axis in the scanner. The sensitivity across the Y axis is shown in the Figure 36. The sensitivity is calculated for two different energy windows, namely ±30% and ±50%, around the photopeak. The maximum sensitivity value appears at the FOV center, where the maximum number of LORs are geometrically collected. For these first tests, simulations run very fast using a single Central Processing Unit (CPU). A sensitivity close to 5% was determined, which is higher than that measured in conventional WB-PET scanners, for instance the Siemens mMR PET with a sensitivity below 2% [65].

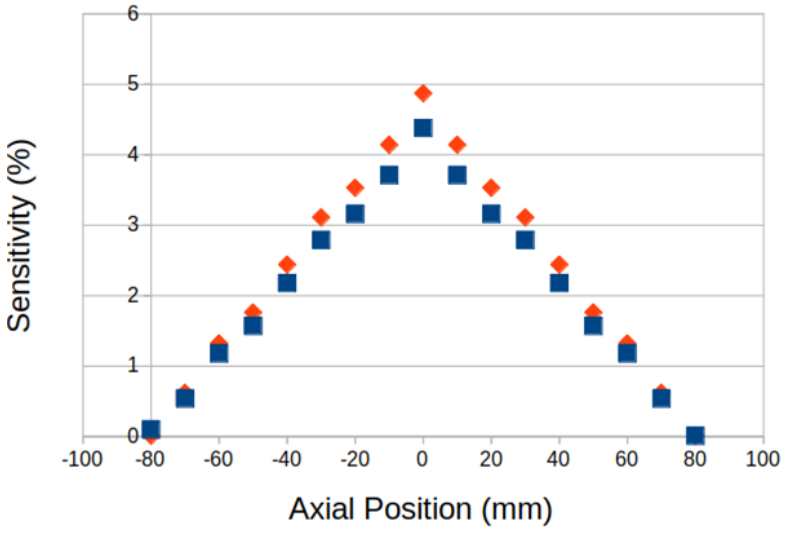

Figure 36. Sensitivity profile for the PROSPET1 system for a 30% energy window (blue spots) and 50% (orange spots).

A ^{22}Na source with 0.25 mm diameter, was simulated moving across the X axis, and then reconstructed with an OSEM algorithm using 3 iterations, see Figure 37. For the reconstruction process, LM data files were generated. The sagittal plane is the parallel to the panels, in this case the YZ, where no source deformation is observed. Nevertheless, both in the transversal (XY) and coronal (XZ) planes, an elongation in the X coordinate is observed and it cannot be mitigated without additional TOF information in the reconstruction process. The volumetric spatial resolution, that is the product of the three space components, was calculated for every source position and compared with a typical volumetric spatial resolution of a WB-PET, estimated as 5 × 5 × 5 mm^3. As the source moves out of the FOV center, the spatial resolution worsens, but always below 30 mm^3.

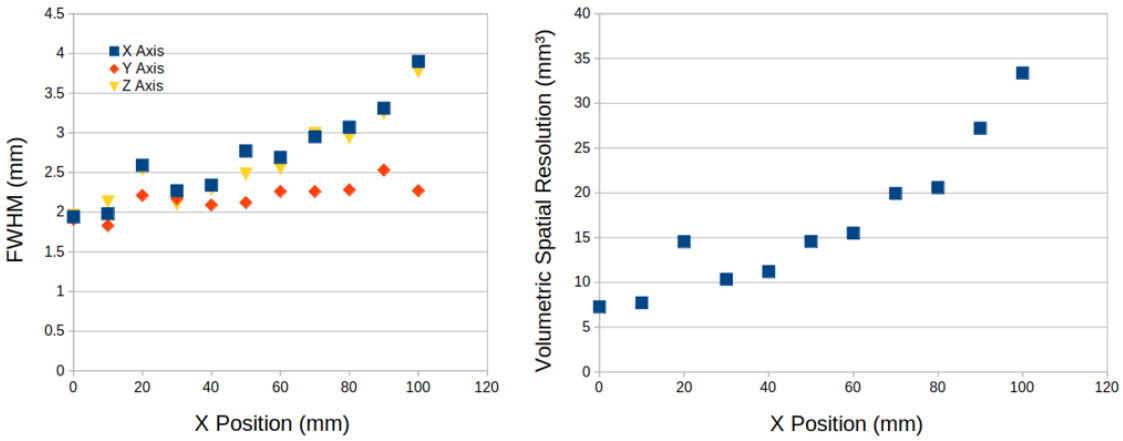

Figure 37. Left: Spatial resolution of a small spherical source in three directions as a function of the position in the X axis. Right: Volumetric spatial resolution across the X axis.

A Derenzo-like phantom was also simulated for this PET configuration to evaluate the image resolution capabilities. A Derenzo-like phantom is a structure composed by multiple inserts, with different sizes, that can be filled with radiation. It is very useful in order to evaluate the spatial resolution. This phantom was designed with 6 different groups of capillaries with diameters of 2.4, 2.8, 3.6, 4.4, 5.2 and 6 mm, see Figure 38. It was placed at the FOV center with the capillaries long axis perpendicular to the X axis. The phantom was filled with ^{18}F, surrounded by Polymethyl methacrylate (PMMA) material. The spatial elongation that takes place in the X axis leads to a deterioration in the final image so not even the 3.6 mm sources are clearly distinguished. This artifact, typical for open ring systems, can be partially fixed with the inclusion of TOF algorithms. Nevertheless, our poor CTR does not allow us to apply them satisfactorily.

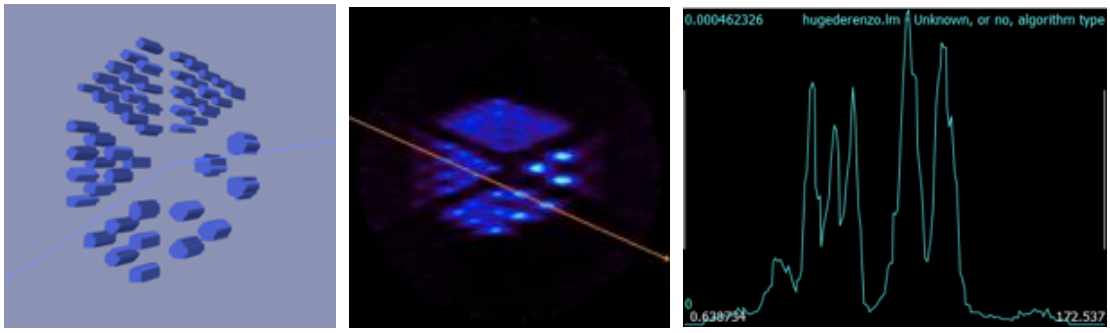

Figure 38. Left: Sketch of the simulated Derenzo-like phantom (notice the image is tilted). Center: Reconstructed image with the elongation. Right: Profile extracted from the reconstructed image, along the 5.2 and 3.6 mm. capillaries.

4.1.3. Two panels prototype, second approach. PROSPET2

A second prototype of prostate dedicated PET, called PROSPET2, was designed and simulated following the same two panels configuration, but with different numbers of detectors in each panel. Since the prostate is placed off-centered between the abdomen and bottom of the patients by 45 mm approximately, the previous design was not geometrically optimized for

such organ location. To make sure that the maximum of the sensitivity would take at the prostate location, the distribution of the 24 detectors was changed. A smaller panel was composed by 6 detectors in a 2 × 3 configuration, whereas the large panel contained 18 detectors (3 × 6). Panels were separated 28 cm. This geometry assures that the maximum sensitivity area lay closer to the prostate preserving the total number of detector modules, which is very important to not increase the scanner total prize. Moreover, it was planned to vary the panel-to-panel distance, if desired. We carried out simulation tests using detector parameters already described for the previous section. A spherical source was again scanned across the X axis (panel-to-panel axis), in steps of 10 mm starting at the center position and moving in the direction to the small panel, see Figure 39. The maximum sensitivity was found at about 50 mm off-center.

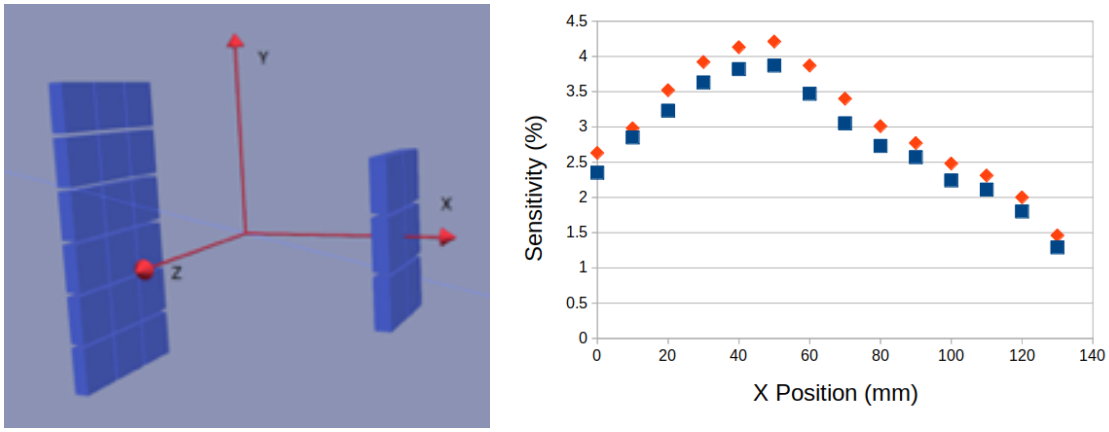

Figure 39. Left: Prototype sketch of the asymmetrical panel PROSPET2 system. Right: Sensitivity across the X axis.

In order to approximate the prostate volume and a possible multi-tumoral lesion, a sphere with 30 mm in diameter was simulated, including two hotspots of 1 mm each and separated 5 mm. The concentration ratio between the hotspots to the background was set to 8. A coronal view (XZ plane) of the reconstructed image is shown in Figure 40 left, along with a profile across the sources. We determined the signal to noise ratio (SNR), defined as the ratio of the hotspots value of the reconstructed image to the background. Despite the elongation, an SNR of 4 was found. For these reconstructions, the OSEM algorithm with 3 iterations was used. No normalization was included. The voxel size of the image was set to 1 × 1 × 1 mm^3. A virtual pixelization in the detector modules of 300 × 300 pixels was carried out. That means a virtual pixel size of about 0.16 mm.

After the simulation tests, the second prototype was built. The system was calibrated using standard procedures we have used in our group [47][55][115], regarding impact position, energy and depth of interaction. The scanner was tested with patients at the Hospital La Fe in Valencia. They were injected with about 10 mCi of ^{18}F-Choline for other tests and later asked (under an

agreed consent letter) to also be scanned afterwards with our prototype and, thus, without the need for extra doses. Total acquisition in our prototype lasted 10 minutes. No normalization nor attenuation correction were applied during the image reconstruction process. OSEM reconstruction was again used with 3 iterations and pixel and voxel values of 1 mm. As an example, Figure 41 shows the image obtained for one of these patients, where a hotspot with higher uptake is observed. The patient was comfortable during the acquisition. However, the image resolution was poor due to the lack of angular information, as well as for the radiation in the patient outside the FOV, in particular at the kidneys, as indicated by the clinicians. This is a prototype that, although useful for some applications in PCa or others, did not fulfilled our expectancies. Given that the dual panel PET system was not able to provide a good patient image, additional studies as NECR rates or quality image were not succeeded.

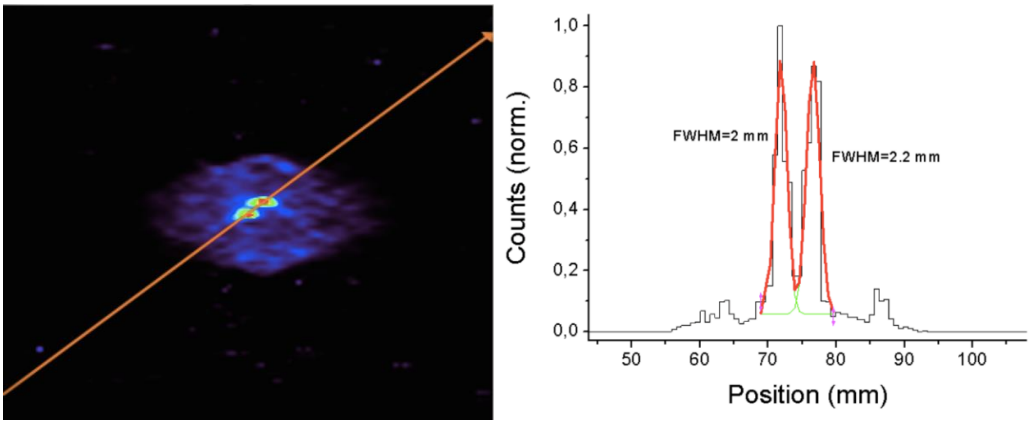

Figure 40. Left: Reconstructed image of the sphere with two hotspots. Right: Profile along the line depicted on the left image. The profile was fitted with two gaussian distributions.

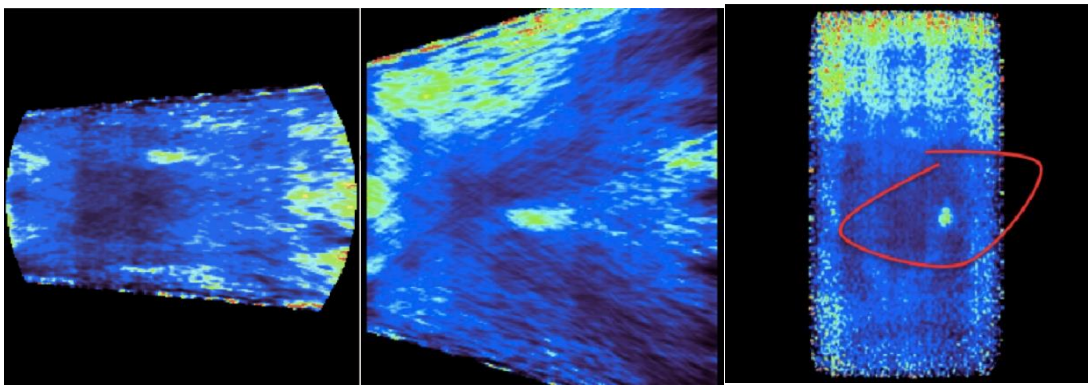

Figure 41. Three views of a reconstructed image with the second prostate PET system. The detection of a small lesions is highlighted at the right panel.

4.1.4. Ring configuration prototype. PROSPET3

The quality of the image exhibited in Figure 41 suggests the need for a different scanner approach either including TOF capabilities or a more regular (cylindrical-like) geometry. At the moment of decision, we were lacking TOF electronics, so we decided to build a PET scanner

following a ring configuration. Thus, the original goal of allowing in-vivo biopsies is still feasible and the former open systems artifacts should be vanished. The ring scanner diameter was 41.6 cm, see sketch and photographs in Figure 42. Despite this prototype is only composed of one ring, the scanner can move axially expanding the axial coverage to 80 mm. The system does not account for a cooling system, but temperature of the detectors was monitored. The system permits to open the top half-ring into two parts, allowing an easy positioning of the patient. Furthermore, the system can be shifted axially to cover more FOV, increasing form 50 mm to more than 70 mm. Figure 42 bottom shows the patient position both for diagnosis and in-vivo biopsy. This reduced PET geometry, in comparison with WB-PET systems, allows the portability to several hospital rooms.

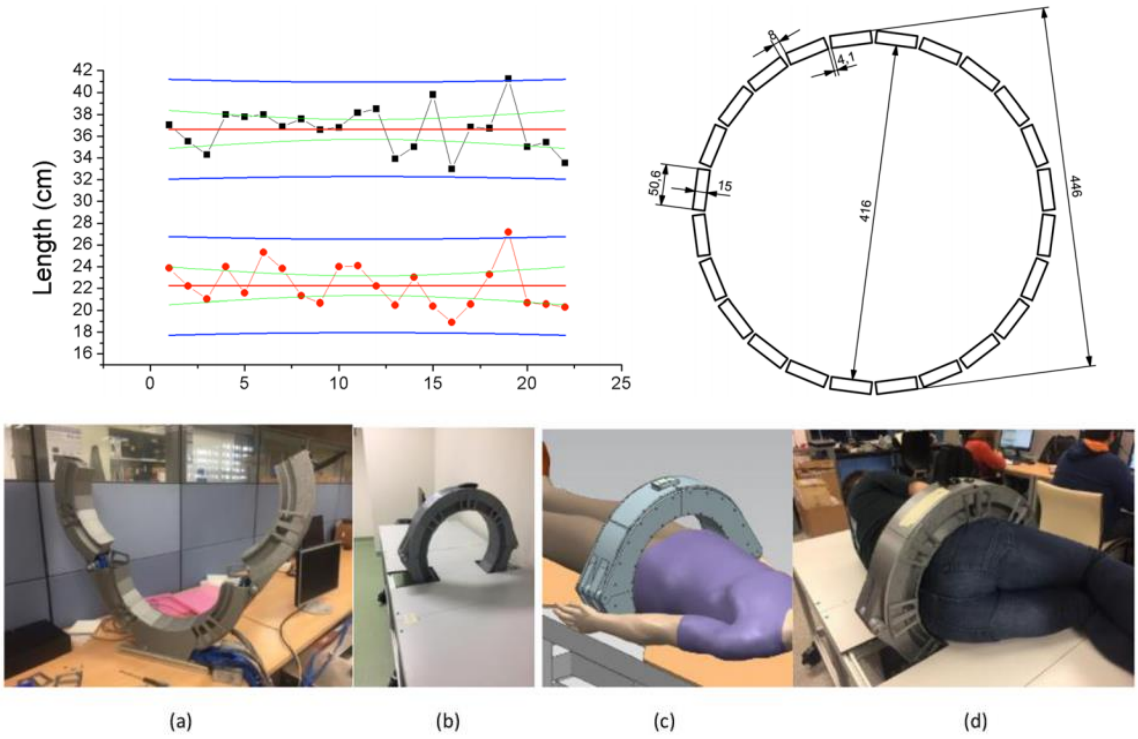

Figure 42. Top Left: Distribution of dimensions for 20 patients. Black points are the wide size whereas the red points are the thickness. Top Right: Sketch of the dedicated prostate PET ring configuration. Bottom: a) PROSPET3 ring system opened, b) Scanner closed and ready to acquire data, c) Patient in supine position, d) Patient in fetal position.

A first simulation test using the GATE platform and this scanner geometry was to image a ^{22}Na source with 0.25 mm diameter, with an activity of 22 µCi at different FOV positions. The aim for this test was to calculate the sensitivity profile along the axial axis. A specific mechanical structure was designed allowing one to place the source in 5 mm steps, see Figure 43 right. The system sensitivity was calculated for two different energy windows namely ±30% and ±50% around the photopeak. The simulation parameters for the detectors were the same used in former designs since the same detector modules were utilized. Coincidences of one detector against its 13 opposites were considered, giving an operational FOV diameter of 30 cm. Figure

43 left shows the simulation and experimental sensitivity obtained using a 30% energy window. Simulation results exhibit a sensitivity maximum of 2.2% while the experiment resulted in 1.4%. The difference between experimental and simulation suggested to some data loss during the data acquisition.

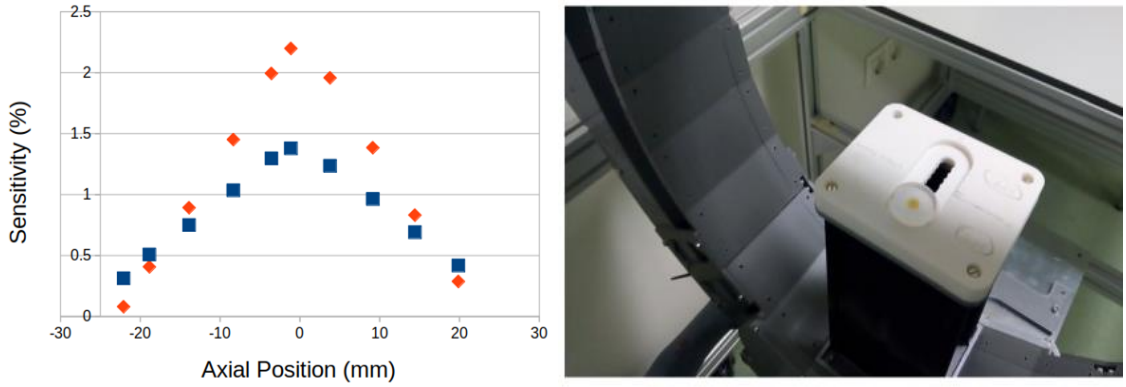

Figure 43. Left: Axial sensitivity profile for simulated (orange spots) and experimental data (blue spots). Right: Mechanical structure used for the experimental sensitivity measurements.

For this prototype, we developed a novel method to correct for the image normalization. An annular phantom of 30 cm in diameter was placed at the FOV center. The phantom was 50 mm in the axial direction and 3 mm active thickness. The phantom was filled with an initial activity of 10 mCi of FDG. The acquisition lasted 10 hours. In Figure 44, a photograph of the phantom is shown (left) together with the reconstructed image (right). The reconstructed image of this phantom has 416 × 416 × 50 voxels, with 1 × 1 × 1 mm^3 each. Detector module coordinates were virtually pixelated to 1 × 1 mm^2.

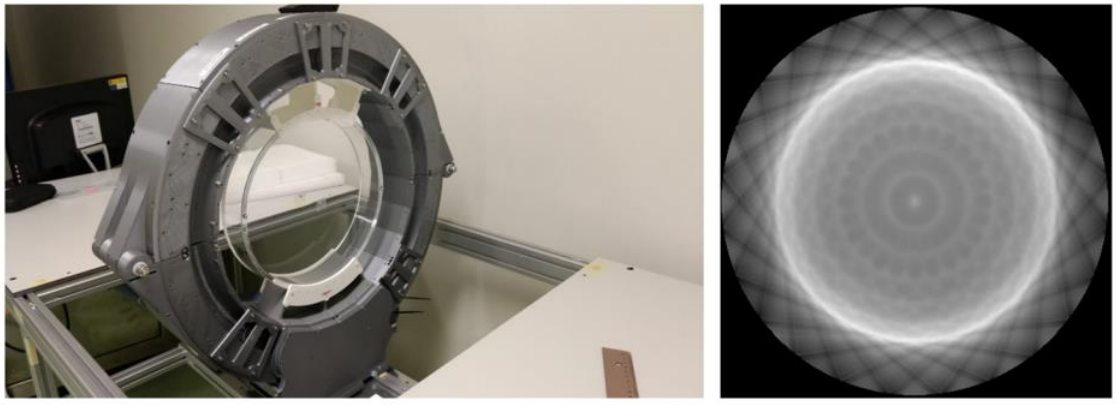

Figure 44. Left: Photograph of the normalization phantom inside the PET ring. Right: Normalization map obtained after an OSEM algorithm with 1 iteration and 1 subset.

Following the NEMA NU2 – 2001 protocol and using the same source than for the sensitivity calculation, we experimentally acquired data along the radial axis in steps of 20 mm starting

from the FOV center. The protocol suggests repeating the same acquisitions but at ⅜ of the axial FOV. A Gaussian fit to every position determined the spatial resolution (FWHM). When the DOI is included in the impact calculation and related LOR, an improvement in the reconstructed images is observed. To illustrate this, Figure 45 shows the reconstruction for a 1 mm in diameter size source with and without DOI correction. Here, the shape and position of the source changes with the DOI. The flatten source corresponds to the reconstruction where the DOI correction was not enabled, elongating the image. However, when the DOI correction was considered, the source recovered the spherical shape and a source shifted is observed, correcting for the parallax error.

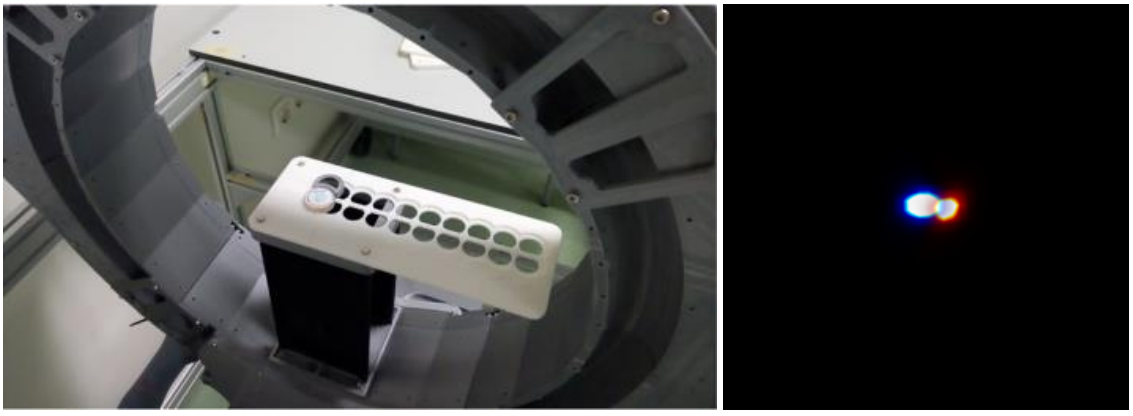

Figure 45. Left: Photograph showing the holder for the spatial resolution measurements. Right: Reconstruction of the 10 cm off centered source with DOI (red) and non-corrected (blue) DOI.

We studied the spatial resolution FWHM as a function of the number of iterations for the OSEM algorithm using the source at the center of the FOV. In Figure 46 top-left, we can observe the minimum number of iterations needed to optimize the radial spatial resolution is 3 iterations, reducing the initial 2.3 mm FWHM to 1.7 mm. Thus, all other reconstructions were made using DOI and 3 iterations. The spatial resolution remains below 3 mm for all three space components. As observed in Figure 46 bottom-right, if the DOI correction is not considered, the radial spatial resolution worsens near the FOV edges, with values larger than 4.5 mm. Furthermore, as expected the spatial resolution does not degrade when the source moves radially far of the FOV center. Due to the small values in comparison with the FWHM of the sources, no errors are shown in the graphics.

Comparison between simulated and experimental data is depicted in Figure 47 with DOI correction, using the same number of iterations than the previous study.

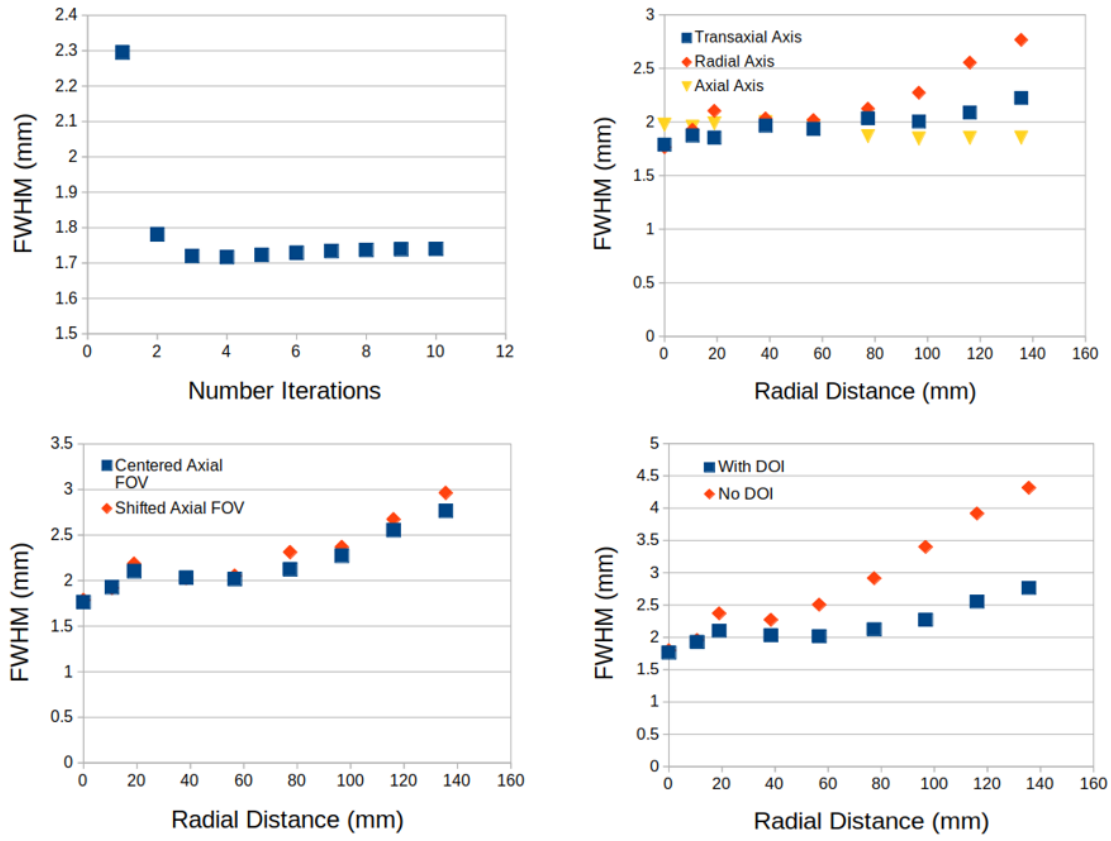

Figure 46. Top Left: Spatial resolution as a function of the number of iterations. Top Right: Spatial resolution for every direction, Bottom Left: Radial Spatial resolution for two different axial positions. Bottom Right: Same but with and without DOI correction.

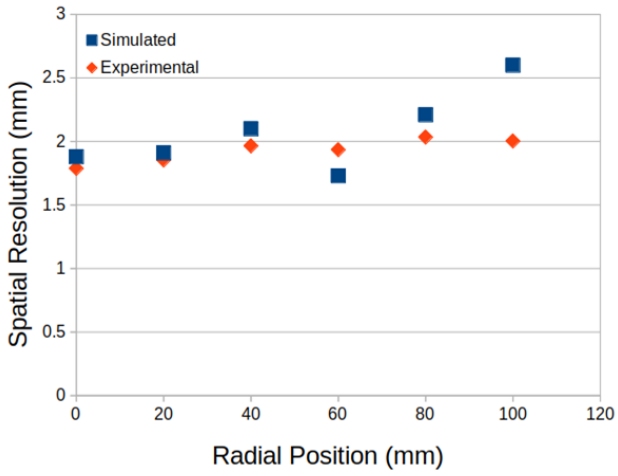

Figure 47. Results of simulated and experimental spatial resolution with a small spherical source.

The experimental NECR curves were found using the cylindrical high-density polyethylene phantom placed at the system FOV center, with a diameter of 60 mm and 170 mm length. A 3.2 mm diameter hole was drilled at a radial phantom offset center of 13 mm. A tube of 1 mm (inner) and 3 mm (outer) diameters was introduced with an initial activity of 5.45 mCi. Before the experiment, the same phantom was simulated with the GATE platform. Activity values ranging between 5.45 mCi down to 0.1 mCi, were simulated. Figure 48 shows both the experimental

data acquisition and simulation sketches, left and right, respectively. Simulations included the 1 µs paralyzable dead time of the electronics data acquisition system.

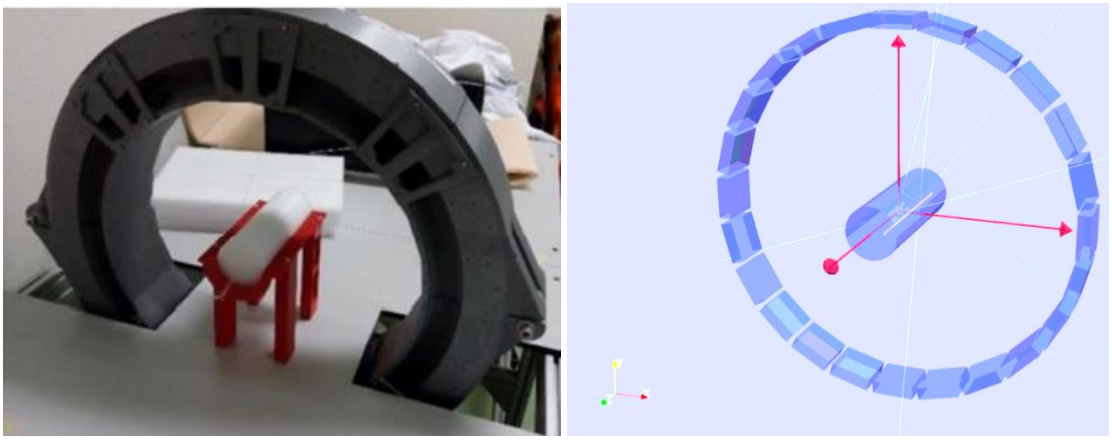

Figure 48. Left: Photograph of the NECR phantom inside the PET system. Right: Same NECR phantom simulated with GATE platform.

Sequential experimental acquisitions every 10 minutes were carried out, for 18 hours. About 100 list-mode (LM) acquisition files were generated corresponding each one to a specific activity [115]. The conversion of LM data to 2D sinograms is carried out after the global coordinates are calculated. Following NEMA protocol, all the sinograms were projected into a 1D plot by summing all the angular contributions. In Figure 49 top, a sinogram for the first acquisition, corresponding to 5.45 mCi activity, and its projection in a 1D graph are depicted. In Figure 49 bottom, a sinogram for one of the latest measurements, corresponding to 250 µCi, is also shown, where the activity has decreased until the random and scatter fraction are much lower than the true rate.

The count rate results are shown in Figure 50. For activity concentrations near 1.7 mCi, the combination of random and scattered events become similar to the true rate and, for higher activities, random and scatter overpass others. According to the simulations, we expected the optimum activity around 2 mCi with an approximated NECR value of 20 kcps. The experimental NECR maximum value is found at 2.4 mCi with at an activity concentration value of 16 kcps. There is a good agreement between experimental and simulation data for low activities, but some differences are observed at higher values.

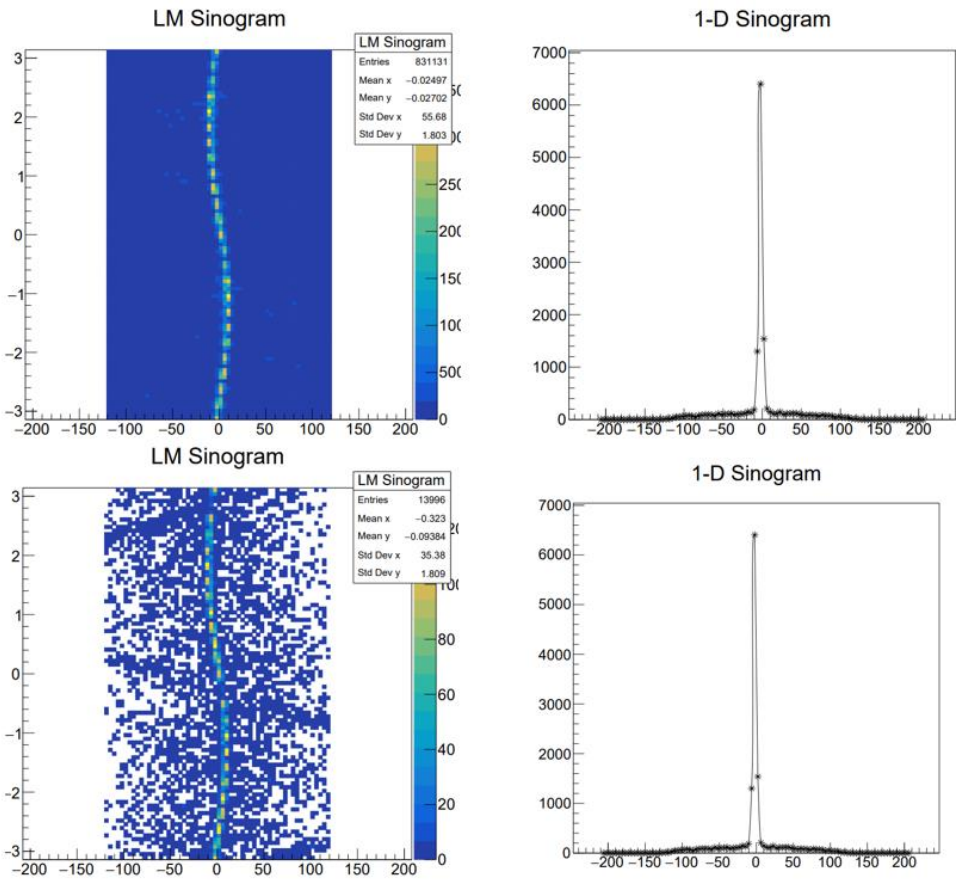

Figure 49. Top Left: Sinogram for the first acquisition. Top Right: Corrected profile extracted from the sinogram. X axis in mm. Bottom Left: Sinogram for one of the latest acquisitions. Bottom Right: Corrected profile.

For this thesis, we had access to the Philips Gemini TF PET/CT scanner installed at the La Fe Hospital in Valencia with the aim to compare PROSPET performance with this scanner [116]. In the figure below, we can appreciate PET and CT images of a patient and the co-registration of both, preserving the advantages of each modality. The PET Gemini TF exhibits a 0.7% sensitivity value in the FOV center and reports 4.7 mm spatial resolution with no DOI information available. The image quality phantom is composed by a main PMMA cylinder with an outer diameter of 135 mm and 103 mm height. Inside the cylinder, six different insert tubes (with 4.5, 6, 9, 12, 15 and 20 mm diameters and 60 mm height) are placed radially at 35 mm offset, see Figure 51. Inserts (or hotspots) were filled with an FDG concentration, 38 and 18 times higher to the one used in the phantom background.

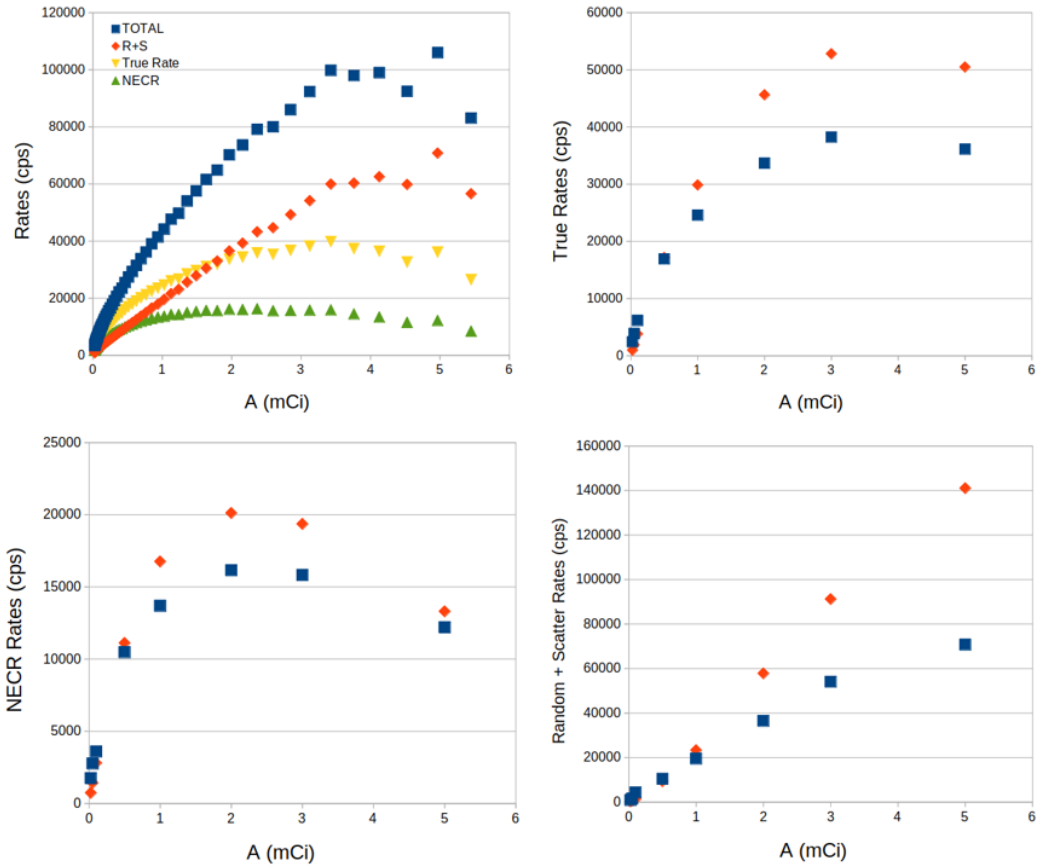

Figure 50. Rates for the PROSPET3 configuration. Top Left: Experimental rates. Top Right: Comparison between the experimental data (blue spots) and the simulated data (orange). Bottom Left: Same but with the random and scatter events. Bottom Right: NECR rates comparison.

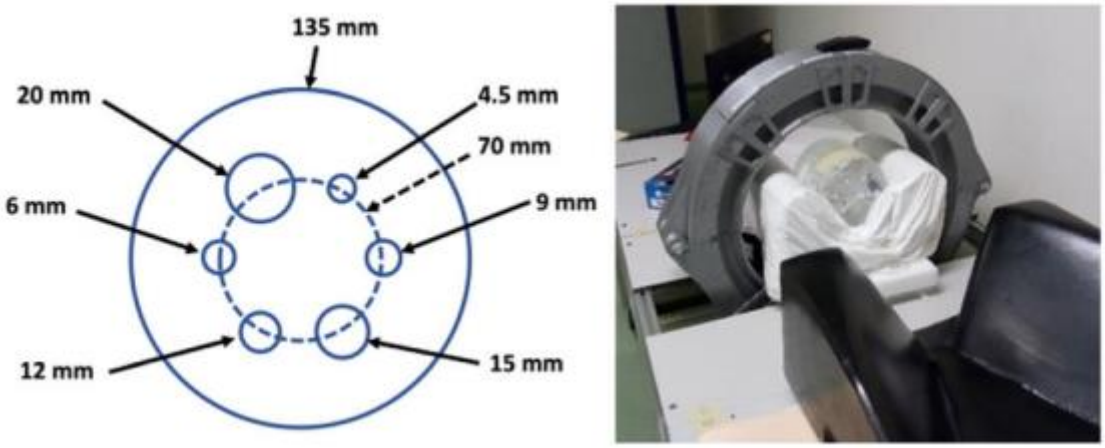

Figure 51. Left: Sketch of the quality phantom. Right: Photograph of the image quality phantom during data acquisition.

For these tests, the phantom measurements were first carried out at the Gemini TF and later with the PROSPET3, lasting 10 minutes each. The Gemini TF data were reconstructed using the BLOB - OSEM - TOF algorithm tool, with 2 iterations and 33 subsets, including a single scatter simulation correction and the delayed window approach for the random correction. Attenuation was corrected for the PET Gemini TF data. With the PROSPET data, the image was first

reconstructed only with the normalization correction in order to extract the shape and location of the phantom inside the PROSPET3 image space. A mask with the shape and location was generated and included in the normalization data. The pixel value of the mask was set as the attenuation coefficient of the water 0.096 cm^2/g. Normalization was recalculated adding the mask information, generating a combined normalization - attenuation map, see Figure 52.

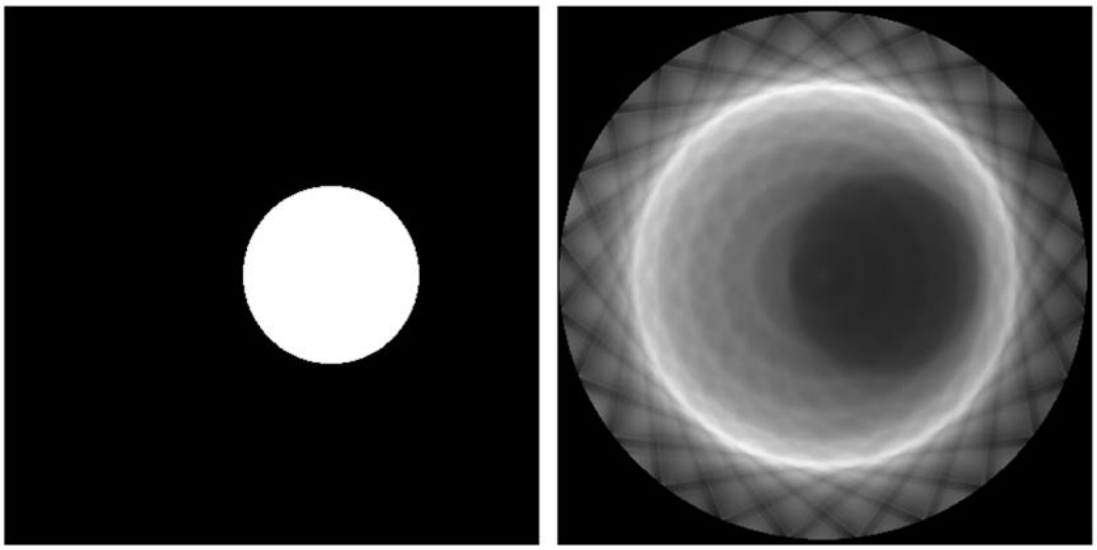

Figure 52. Left: Attenuation mask of a cylindrical shape phantom filled with water. Right: Overlapping normalization and attenuation maps.

We compared the Contrast-to-Noise ratio (CNR) as well as Contrast for both scanners. Volumes of Interest (VOI) were extracted for each image. 12 VOIs were generated, with the same theoretical radius than the hotspots and 25 mm height, distributed along all the background regions. Analyzing these VOIs, the background value and its standard deviation were estimated. 6 more VOIs were produced and placed in each hotspot. CNR and Contrast values are calculated using the following expressions:

$$CNR = \frac{Mean\ Hot\ Spot\ VOI - Background}{Background\ Standard\ Deviation} \quad (7)$$

$$Contrast\ (\%) = 100 * \frac{Mean\ Hot\ Spot\ VOI - Background}{Mean\ Hot\ Spot\ VOI} \quad (8)$$

The number of iterations was again optimized but for this phantom. Reconstructions with iterations varying from 1 to 16 were performed and for each of them the background as well as CNR values obtained. In terms of background, a valley was found between 6 and 9 iterations, see Figure 53. The CNR for the largest and the smallest hotspots (20 and 4.5mm diameter, respectively) exhibited different behavior. The largest gets a maximum value at iteration 8, whereas the second one gets stabilized in the 14-th iteration. A compromise between the average background value and the CNR of both inserts was set to the 8-th iteration.

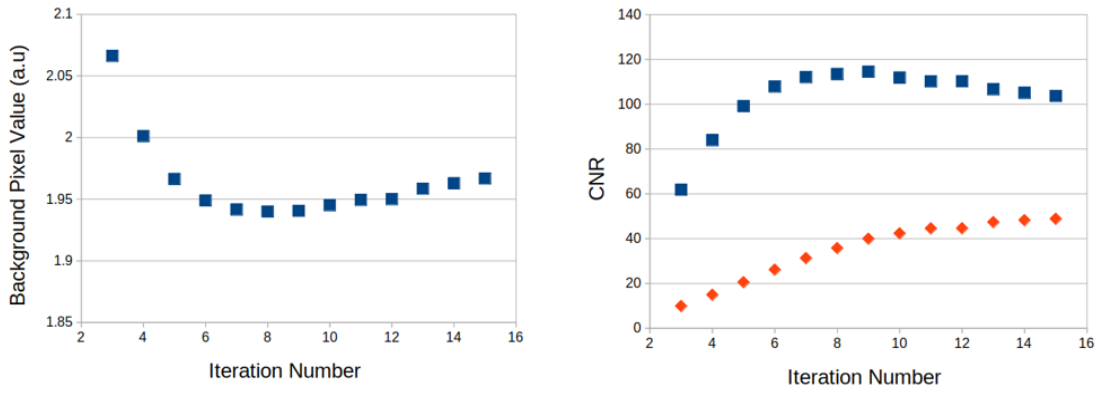

Figure 53. Left: Background value as a function of the number of iterations. Right: CNR for the largest (blue) and the smallest (orange) insert as a function of the number of iterations.

Reconstructed images of the phantom for the Gemini TF and dedicated prostate PET, for both activity concentration ratios, are shown in Figure 54. Notice that the dimensions of the voxels for the Gemini TF were $4 \times 4 \times 4$ mm^3 in comparison with the $1 \times 1 \times 1$ mm^3 of the PCa dedicated PET. CNR and Contrast results are shown in Figure 55. Even without scatter and random corrections, the performance of the prostate-dedicated PET is similar to a TOF-PET scanner. Furthermore, in the case of the smallest rods the contrast is enhanced in comparison with a conventional PET scanner.

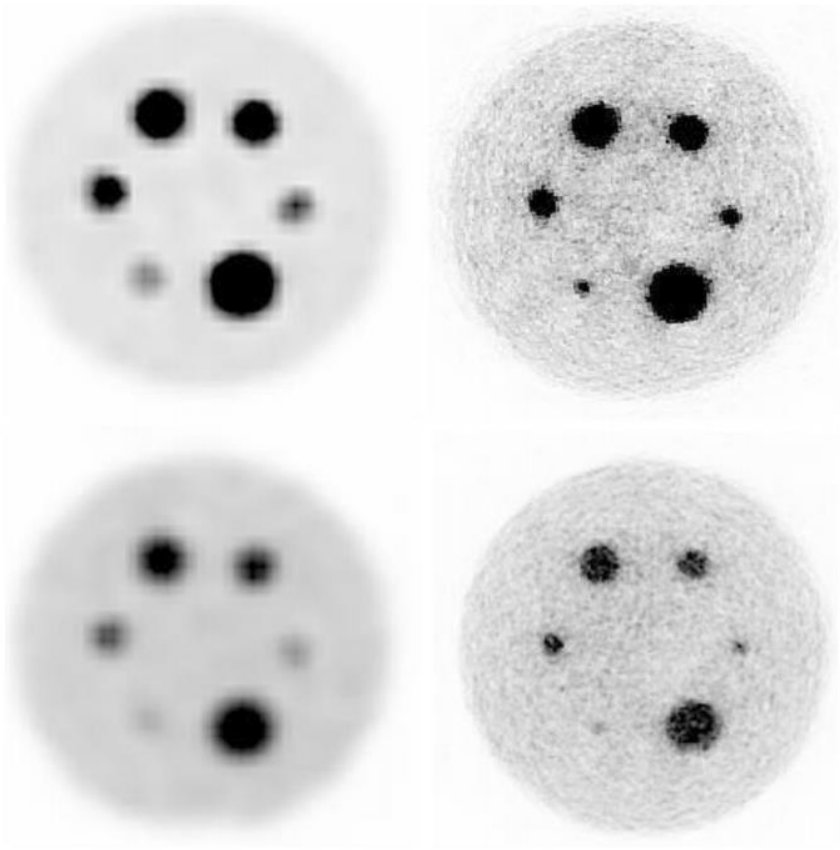

Figure 54. Top: Phantom comparison between the PET Gemini (left) and PROSPET3 (right) for an activity ratio hotspot-background of 38. Bottom: Same for an activity ratio hotspot-background of 18.

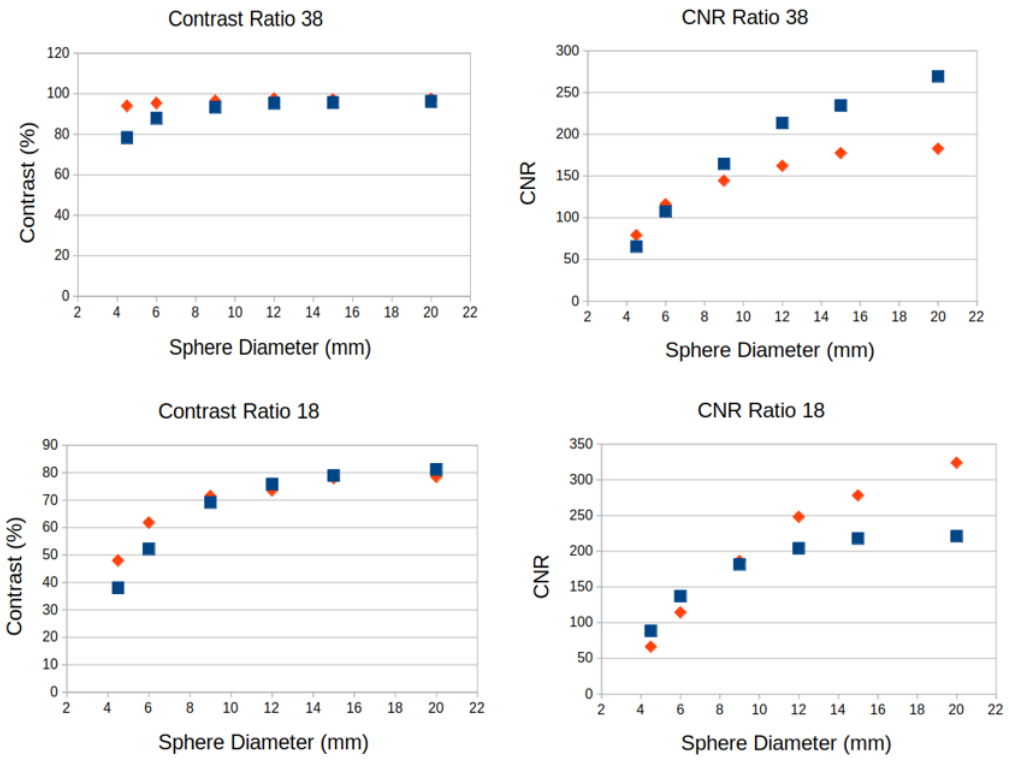

Figure 55. CNR and Contrast comparison for the WB-PET Gemini and the PROSPET, for two different spots-to-background ratios.

Finally, the system was installed at the Hospital La Fe in Valencia to check its capabilities with patients. One person diagnosticated with two lesions in the prostate area agreed to be examined with the PROSPET3, after an acquisition with the Gemini TF PET/CT scanner. The patient was injected with 7.5 mCi of a ^{18}F-Choline solution 30 minutes before the WB-PET acquisition. In the prostate PET, attenuation correction was implemented by introducing an anatomical image of the patient generated by the CT scanner. 30 minutes after the WB-PET acquisition, the patient was scanned in the PROSPET3 for 7 minutes at each axial position. A smoothing post filter was applied with 5 mm FWHM and 3.5 sigma in the convolution kernel, see Figure 56. Despite all the image corrections, the clinical image obtained with the conventional PET had a higher quality. We believe possible activity outside the FOV, a poor attenuation correction, the data lost during the acquisition and other factors might have caused the image degradation. Nevertheless, some of these issues can be improved for future projects.

We started in a multi panel system with monolithic detectors named PROSPET1, but we finally rebuilt the system in an annular geometry (PROSPET3). In Figure 57, we compare the capabilities of the first system and the ring configuration.

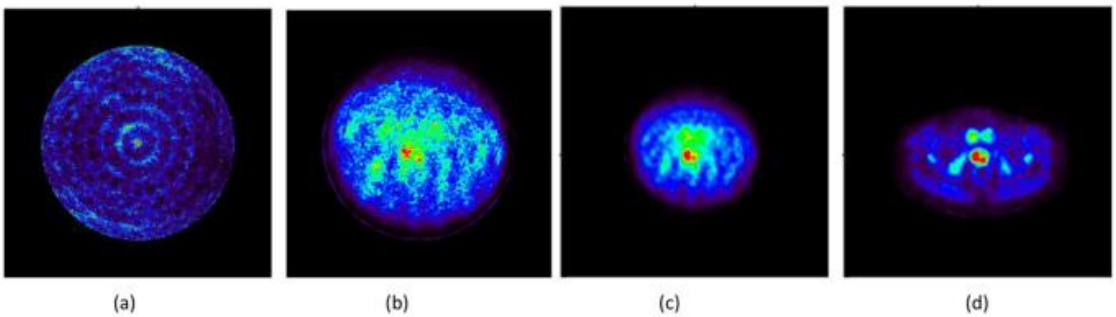

Figure 56. a) PROSPET patient image with no normalization b) Normalization but no attenuation c) Attenuation correction with the CT d) WB-PET image.

Figure 57. Comparison between the first prototype (PROSPET1) and the last one (PROSPET3).

4.2. Heart PET imaging: CardioPET

PET systems that enable the use of TOF information enhance the image contrast capabilities and, furthermore, allow one for the design of open ring geometries [104]. A specific PET system for heart imaging is described in this section. The main target of this device is to evaluate the radiotracer distribution and uptake under stress heart conditions. To make so, the patient would be doing exercise with a static bicycle during the data acquisition. Undesired patient motions are unavoidable under these experimental conditions and, therefore, an optical camera device would be integrated with the system. Motion correction algorithms will be applied to correct PET images with the optical camera information. All motion correction information will be extendedly introduced in section 4.3. This project was named CardioPET. It was supported by the Spanish *Ministerio de Economía, Industria y Competitividad* under Grant TEC2016-79884-C2-1-R. This scanner is composed by either two or four identical panels placed in such a way that the sensitivity maximum area is at the heart area. Figure 58 depicts the position of the panels.

The original aim in this project was to use detectors blocks based on thick monolithic crystals and analog SiPMs. However, this combination presents some challenges to provide an accurate sub-300 ps time resolution [49][118]. Therefore, we decide to use pixelated crystals in the CardioPET system [119].

4.2.1. Pixel and microcell simulation study

LYSO pixels of 10 mm height were chosen for each detector block. The size of both SiPM and pixels was deeply studied to provide the best performance. In addition to the experimental study [119], optical simulations were carried out, as discussed in the following figure.

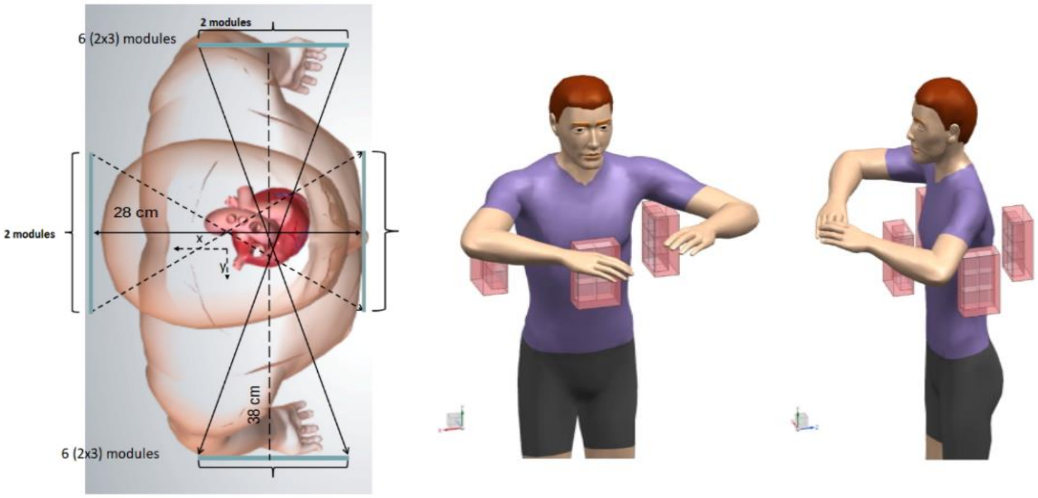

Figure 58. CardioPET sketch. Four panels with the same dimensions are placed for enhance sensitivity at the hearth position.

When using pixels of small dimensions compared to the SiPM active area, a photosensor saturation may occur producing light losses and affecting both energy and timing capabilities. A series of simulations were run to test several configurations. Regarding SiPM microcells, 3 different SiPM cases were considered: Configuration 1 is based on the largest SiPM area of 3 × 3 mm^2, Configuration 2 uses 2 × 2 mm^2 SiPM and Configuration 3 refers to 1 × 1 mm^2 SiPM area. For each configuration, two different microcells sizes were investigated namely 25 × 25 μm^2 and 50 × 50 μm^2. These two different microcell types exhibit different fill factors, which were included as an additional probability detection in addition to the SiPM Photodetection Efficiency, namely 47% for the 25 µm and 74% for the 50 µm. Three different LYSO pixels were studied all with 10 mm height but 3 × 3 mm^2, 2 × 2 mm^2 and 1 × 1 mm^2 size. An ESR surface was introduced in the simulation between the LYSO pixels. A layer of optical grease with 300 µm thickness was included between the LYSO crystals and the SiPM entrance.

It is expected to find a better detector time resolution when more optical photons are registered in one single SiPM pixel. A photoelectric event (511 keV energy) occurring in a LYSO crystal generates 16000 OP. The percentage of light that is registered in the main SiPM (defined as the SiPM in which the photoelectric effect has happened), is shown in Figure 59 top. In the bottom of this figure, the total light registered in the main SiPM is depicted. For all configurations, a major part of the scintillation photons is registered in the main SiPM, but the

light in configuration 2 and 3 gets more spread than configuration 1, and more OP are collected in the neighbor SiPMs. Furthermore, a smaller number of OP are collected in the main SiPM for these configurations. The fill factor introduced for 25 microcells size leads to a higher saturation collecting this way less OP.

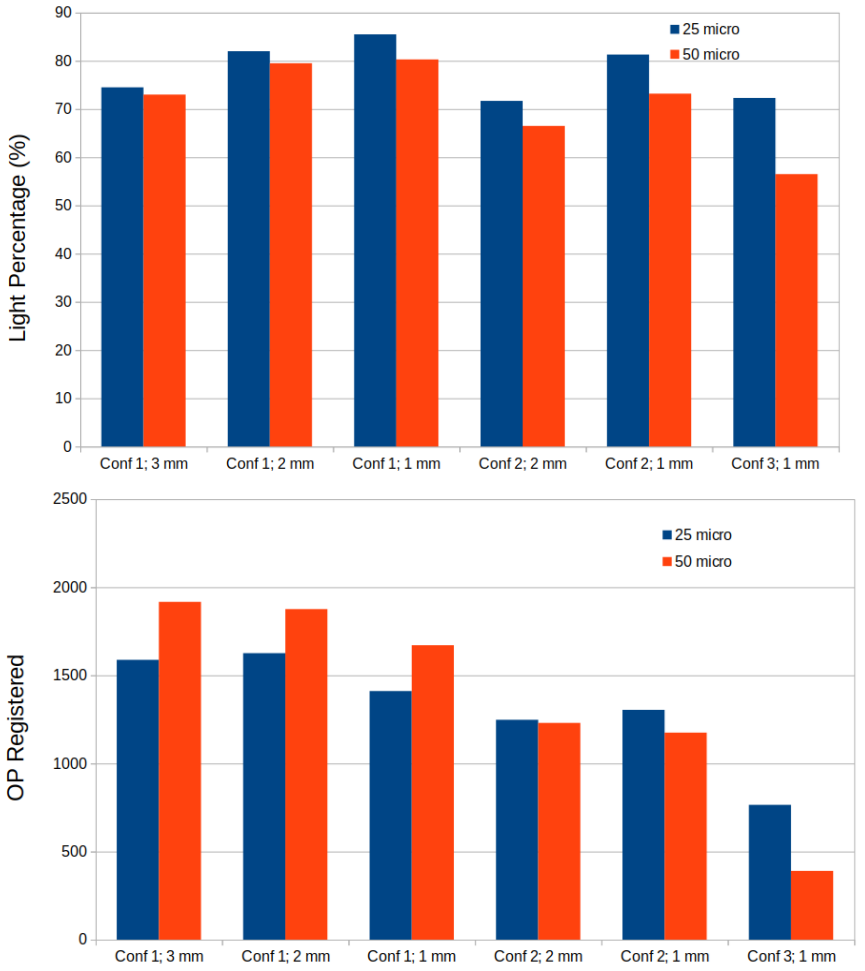

Figure 59. Top: Light percentage registered in the main SiPM. Bottom: Number of OP registered in the main SiPM.

Due to the high light collection in the main SiPM, the chosen LYSO pixels to build the simulations and prototype were the 3 × 3 mm^2, with SiPM of the same area and 50 × 50 μm^2 cell size. Using this pixel-SiPM configuration, an additional simulation test was carried out using an array of 8 × 8 LYSO crystals with dimensions of 3 × 3 × 10 mm^3 and a pitch of 3.36 mm, coupled to a SiPM array of the same active area dimensions. In order to evaluate the energy resolution, we have simulated a small spherical ^{22}Na source placed above the center of the detector module. Every time a nuclear interaction is recorded within the LYSO volume (Compton, Photoelectric…), scintillation light is produced and registered in the photosensor plane. CoG algorithm was applied to the light collected by the different SiPMs, resulting in the flood map shown in Figure 60. The flood map exhibits the capabilities of the detector block to resolve the pixels. The energy

resolution was calculated with the spectrum generated with the total amount of OP registered, resulting in an 11%, see Figure 60 bottom.

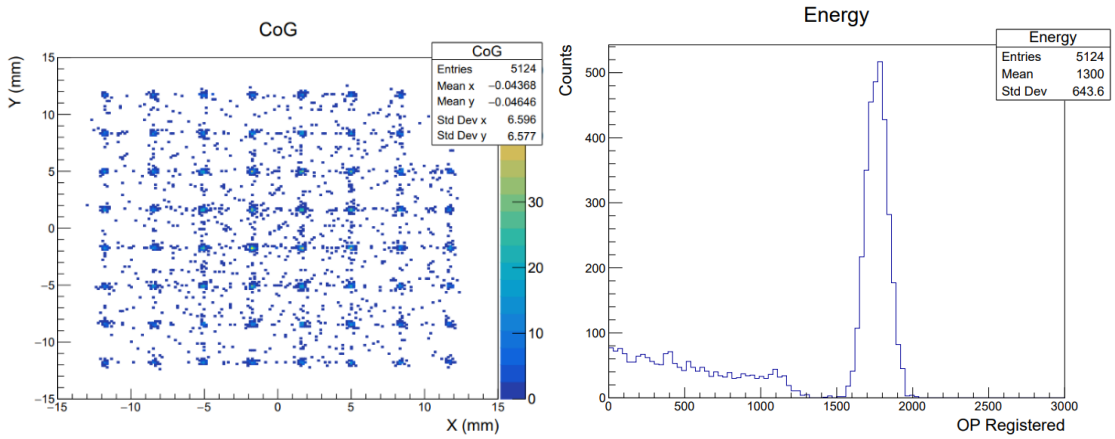

Figure 60. Left: Flood map of the 8 × 8 crystal pixels when irradiated with a far source. Right: Energy spectrum with a 11% resolution.

4.2.2. Performance study

Figure 61 shows the schematic of the cardiac PET scanner, including the definition of all system axes. A complete nuclear simulation study was performed in order to analyze the CardioPET capabilities. A coincidence time window was set to 5 ns and no coincidences between two consecutive panels were allowed. Energy resolution was estimated to be 11 %, based on the optical simulation results, and the time resolution set to 240 ps based on preliminary experimental results [109]. Two panels, separated 28 cm in the X axis, were installed and tested experimentally, in order to compare with the simulations [117]. With the simulations, we determined the sensitivity profile by moving a ^{18}F source of 0.25 mm in diameter and 10^5 Bq along the X axis, following the NEMA NU 2 2012 protocol. Experimentally, a ^{22}Na source with a low activity of 22 µCi was also scanned along this axis. In Figure 61, the comparison between experimental and simulated data for these two panels is depicted.

The NECR estimations, also for two panels, were performed also following the NEMA NU 2 2012. We have simulated and also experimentally obtained such NECR rates for several activity concentrations. The phantom was the same used in section 4.1.3 for the prostate-dedicated PET system, with 25 mm in diameter and 70 mm length. In order to calculate the NECR curves, sinograms must again be calculated for each activity. In terms of simulation, the curve is shown in Figure 63, the blue line. Only few activities were simulated but there were enough to study the trend. EW was set in 30%. At 2.36 mCi, the simulated NECR peak reaches almost 160 kcps. The experimental curve was obtained and compared for the same activities tested in the simulation. The experimental NECR maximum activity takes place at 2 mCi and 140 kcps. There

exist some differences between the experimental and the simulated rates that can be explained with the data loss in the acquisition system and other factors.

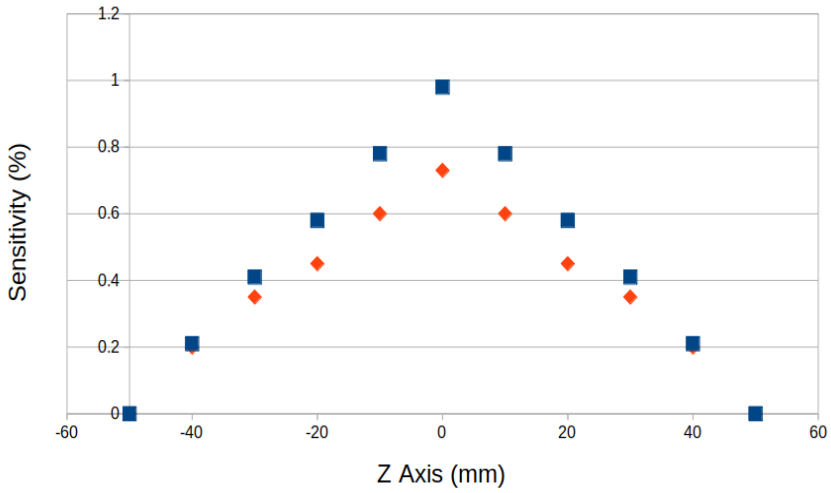

Figure 61. Left: Sensitivity profile for the two panels configuration (both connected by X axis). Comparison between simulated (blue) and experimental (orange) data.

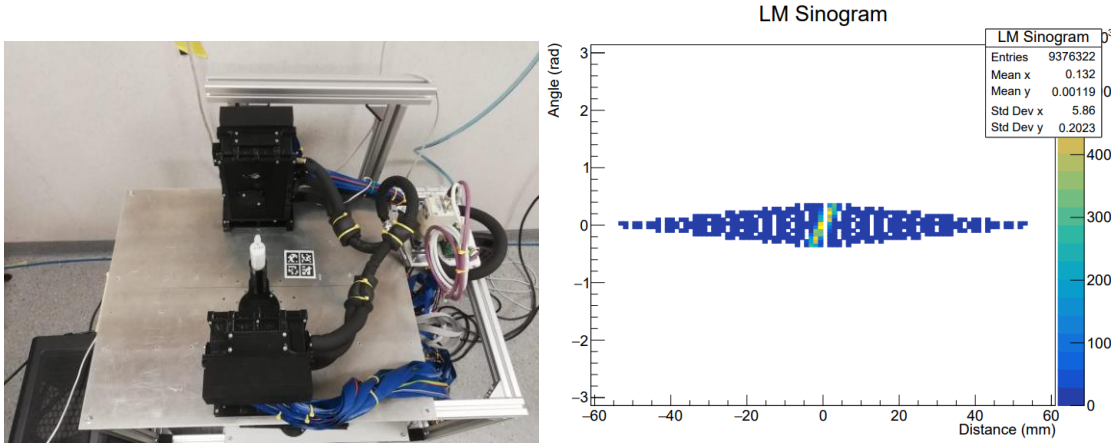

Figure 62. Left: Photograph of the NECR acquisition. Right: Experimental sinogram obtained for this phantom. Notice that is truncated due to the lack of angular information.

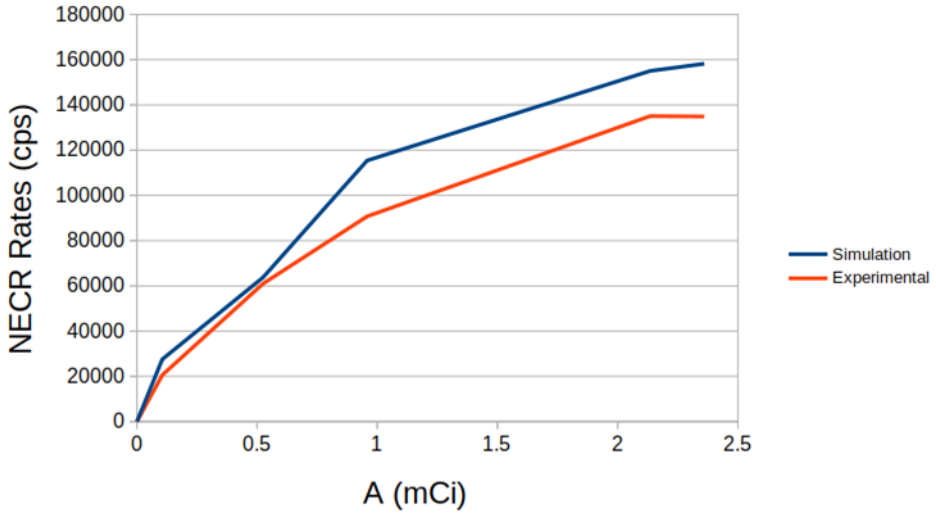

Figure 63. Comparison of simulated (blue line) and experimental (orange) NECR values for 30% energy window.

Nuclear simulations tests, with a spherical 80 mm diameter phantom, were also carried out (back-to-back radiation) to study the reconstruction process with the two and four panels PET configurations. Notice that TOF was not considered during the reconstruction process. The reconstructions were carried out using an OSEM algorithm with 4 iterations and 1 subset. The phantom was placed in the FOV at the maximum of the expected sensitivity, which takes place at 45 mm off-the-center of the system in the X axis. See the obtained reconstructed images with only 2 panels and with four in Figure 64, left and right, respectively. For only two panels, the lack of angular information results in a significant deformation of the phantom. If the information of the other two panels is considered, this elongation is partially mitigated. Even that the reconstruction with 4 panels approximates the spherical shape better, it is still not enough to reproduce a total sphere.

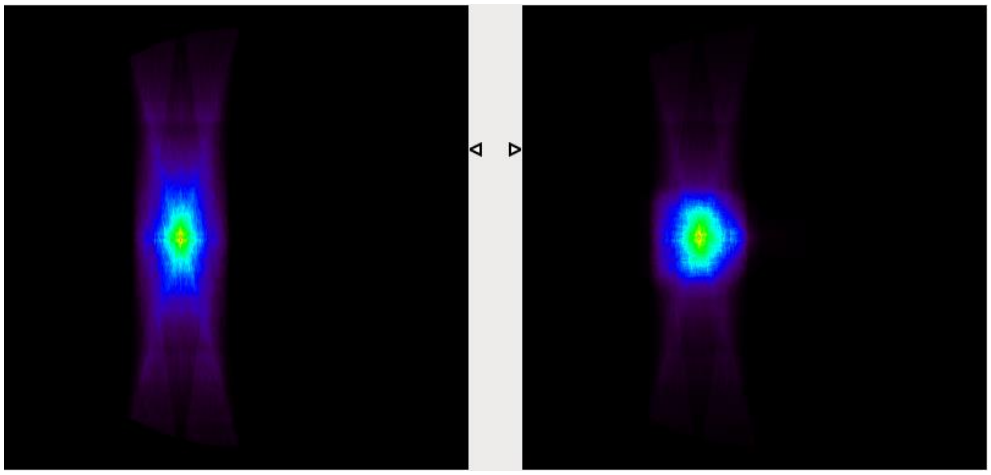

Figure 64. Spherical 80 mm in diameter phantom reconstructed with 2 (left) and 4 panels (right).

The simulated spatial resolution of the system has been evaluated using again a spherical ^{22}Na source, 0.25 mm diameter, placed across the Y axis in the X = -45 mm position, in 10 mm steps. For each simulation, data has been reconstructed with 4 iterations and 1 subset with both only the two panels in the Y axis, but also for the 4 panels system configuration, see Figure 65. The artifact is almost vanished with the 4 panels case.

An additional test we carried out was to compare the simulated and experimental spatial resolutions with the two panels. The sodium source was placed in the FOV center and then shifted in steps of 10 mm along the Y axis. The FWHM was calculated in the X axis, where the elongation takes place, and in the radial Y axis. The radial spatial resolution exhibits an average value of 1.4 ± 0.3 mm for the simulation and 1.5 ± 0.1 mm for the experimental data. Moreover, as expected the FWHM at the X axis is worst, reaching and average of 5.3 ± 0.4 mm for simulations and 5.0 ± 0.4 mm for the experimental case [117].

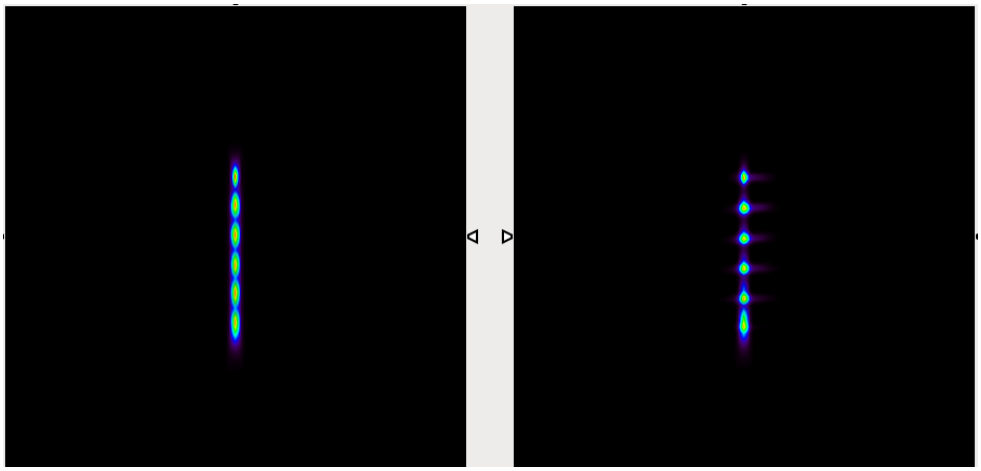

Figure 65. Left: Small ^{22}Na sources reconstructed with 2 panels. Right: Same with 4 panels.

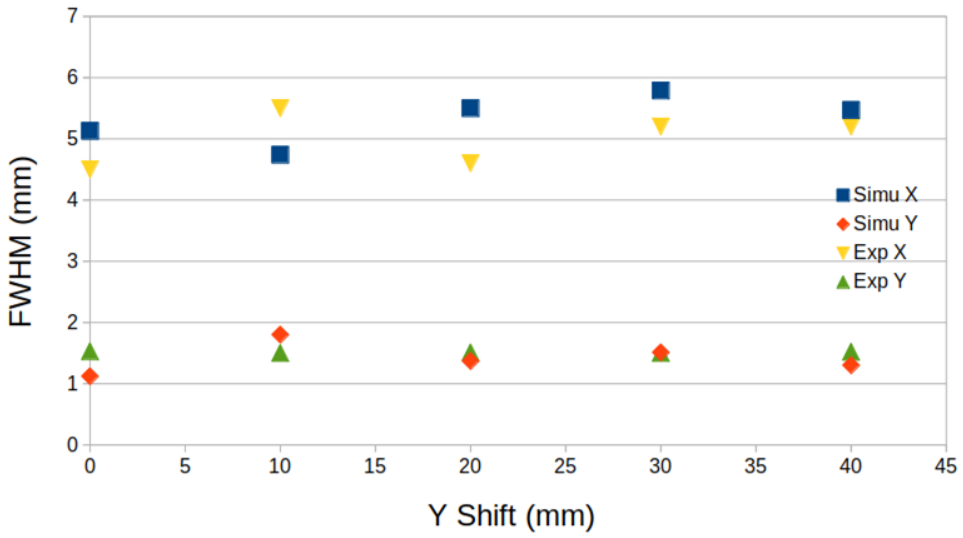

Figure 66. Spatial resolution comparison of experimental and simulation data.

4.3. Motion correction

Artifacts originated from the patient motion cause a blurring in the final reconstructed image [120]. Figure 67 shows examples how motion uncorrected images are affected, for two different views. According to a typical clinical study, PET acquisitions can last many minutes, up to the range of 30 minutes, where the patient can unconsciously move. This situation can get worse for dynamic studies where multiple acquisitions are taken during a time frame that can last as more as 60 – 90 minutes. The particular case of heart imaging studies is furthermore complex, since this organ accounts for its intrinsic non-rigid movement.

Most of the algorithms that correct the motion deformation in the image require to accurately know the patient displacement. The motion respect to the original position must be recorded, both the space coordinates and the three angular positions (yaw, pitch and roll

angles). This information is provided to the reconstruction process. In this thesis we will focus on the patient motion, in particular in the motion of sources, leaving the intrinsic motion of the heart for future works.

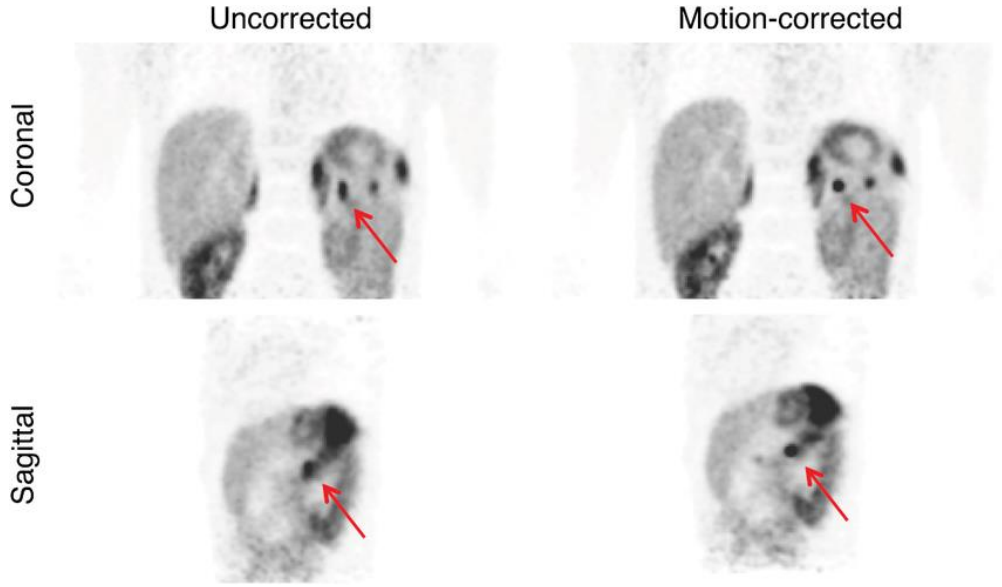

Figure 67. Motion correction applied for a PET system [121].

4.3.1. Tracking camera

One of the objectives of this thesis was to set up an external camera device that records all the motion parameters. We selected a 12 MegaPixels camera with a time resolution of 8 fps. For patient tracking, ARUCO markers have been employed [122]. These markers consist of an inner region with a binary pattern with 6 × 6 pixels surrounded by an external black border. Marker identification is performed by the pixels pattern. After the calibration and the corner calculation, the camera is able to register the Euclidean displacements XYZ, and also the Euler rotation angles. To accurately carry out this process, the black squares should be well differentiated from the white corner. During the calibration process, the subpixel accuracy algorithms differentiate the corners in order to provide the cartesian coordinates [122]. ARUCO libraries offer the possibility of working with more than a single marker to improve the resolution, nevertheless for this study we only worked with a pair of different markers, see Figure 68. One of them remains static within the PET scanner framework and can be used as a system reference, whereas the other follows the patient movement or the radioactive source in our bench-top case. ARUCO markers are a good choice to categorize the solid rigid motion of the patient with sub millimetric precision, but for solid deformations, or non-rigid displacements, additional information is required.

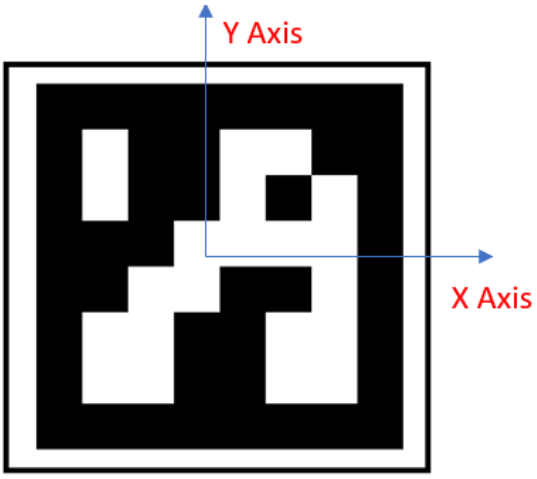

Figure 68. Sketch of an ARUCO marker (www.medium.com).

4.3.2. Motion correction algorithms

After achieving accurate parameters for the 3D motion of the object/patient using the camera, this information is used to compensate the patient movement. Among others, two methods to carry out this process are the LOR rebinning [123], see Figure 69, and the Multiple Acquisition Frames (MAF) algorithm [124]. Both methods require an accurate synchronization of the PET data and the camera. In the LOR rebinning algorithm, the LOR are recalculated to the correct space, every time a motion is registered. This is a well-known technique for brain studies [125]. However, this method presents some drawbacks, such as the inability of dealing with non-rigid motion cases [126][127].

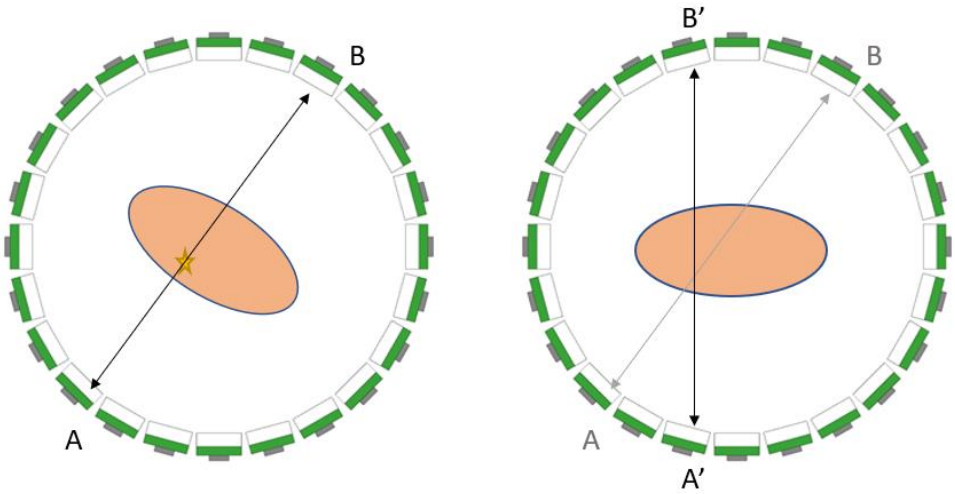

Figure 69. AB relocation with LOR rebining motion correction.

MAF algorithms do not directly work with the LORs. After properly synchronizing the camera output with the PET acquisition, the algorithm divides the total acquired file (LM) into N frames according to a 3D space condition. For instance, this condition can be such that the source has moved if the Euclidean vector module that connects two consecutive camera positions is larger

than a certain distance, for example 1 mm. Even this is the fastest condition, the results can significantly vary according to the programmed distance. Another condition is to grid the 3D space with a well-known voxel size and associate each voxel with a sub-LM file that will be filled if the camera file establishes that the displacement reaches that voxel. This last procedure, called motion condition, was the chosen one for the real data used in this thesis due to the non-dependency of an arbitrary vector condition that can significantly affect the results. An additional algorithm with the grid configuration was implemented to split the main LM data in sub-LM files [128]. An additional condition, such as eliminating the sub-LM files that account for very low LOR events, might help discarding noisy contributions. Later, an OSEM or MLEM algorithm is applied to every individual sub-LM file, with the same number of iterations and subsets, so there will be as many images as sub-LM files divided. Finally, a particular translation and rotation matrix is applied to each image according to the shift respect to the reference image, typically the first frame. In Figure 70, the MAF process is summarized. The main advantage of this technique is the possibility of including the non-rigid motion blurring in the translation matrix, despite additional information being required. For this reason, one step forward would be the inclusion of, for instance, an electrocardiogram (ECG) for the heart intrinsic motion [126].

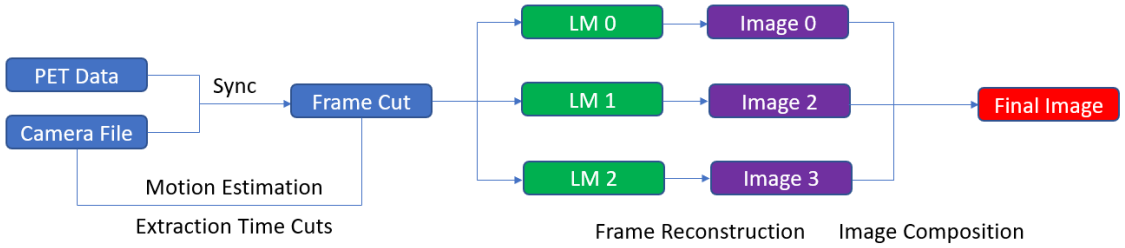

Figure 70. Scheme of the MAF motion correction process.

4.3.3. Simulation tests

The MAF algorithm was tested with simulated data for two PET configurations. The first scanner was the two asymmetrical panels PROSPET2, and the second one the ring configuration PROSPET3. Using the PROSPET2, a set of spherical sources, with different diameters and activities, were distributed in a grid and placed at X = 45 mm (see Figure 71). The sources had radius of 15, 10, 7.5 and 5 mm, with activities of 6, 3, 1.5 and 1 MBq, respectively. Two simulations were carried out namely a static one and another where all the sources randomly moved in the YZ plane as a solid rigid, so there is no relative motion between the different sources. The solid rigid motion was planned to emulate a patient random misplacement, so the frame-to-frame shift was restricted randomly 1 to 5 mm in any YZ direction, but always in the X = 0 plane. A file was generated containing the motion information, XYZ positions and Euler

angles, as well as the exact time when this happens, emulating the camera output. The MAF algorithm was applied to these sets of data. The static, the uncorrected and the corrected images were reconstructed with the OSEM algorithm and 3 iterations. Figure 71 shows on the top the uncorrected and corrected images of the simulated sources, together with the sketch of PET system. At the bottom of this figure, profiles across the smallest sources (S1 to S4) for the two cases namely corrected (MC) and uncorrected (No MC) are depicted.

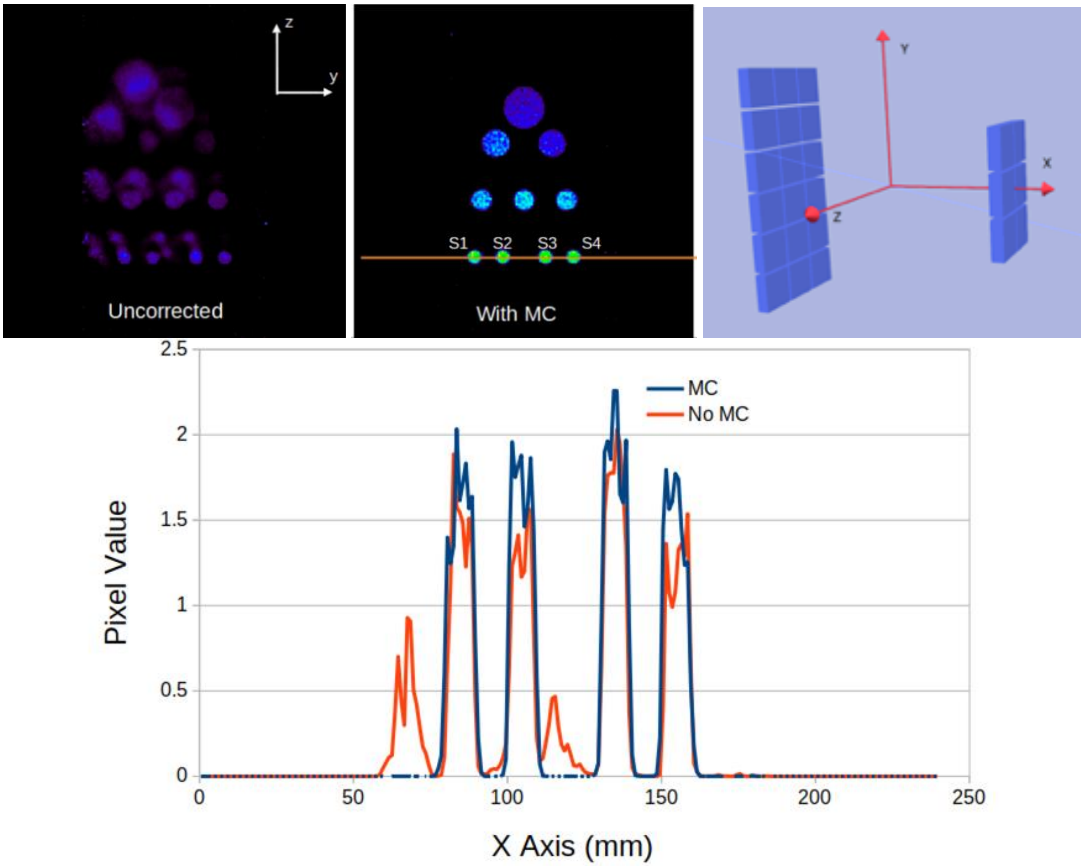

Figure 71. Top Left: Uncorrected final image of the spherical sources grid. Top Center: MC (Motion Corrected) image after MAF algorithms. Top Right: Sketch of the dual panel PROSPET2. Bottom: Profiles of the uncorrected final image (orange) and the MAF corrected (blue).

Additional motion correction tests were carried out with the annular PROSPET3 configuration. Two different source arrangements were simulated. For the first test, three ^{18}F sources with 10 mm diameter were randomly moving together in the Z = 0 (axial axis) plane. The three sources had identical activities of 39.7 µCi. The motion condition was established as a displacement of more than 1 mm similarly than the two panels simulation. As in the previous test, the grid was moved as a solid rigid so the individual sources cannot separate between them. Sources shapes were satisfactorily recovered after applying the MAF technique. All reconstructions were implemented using an MLEM algorithms and 3 iterations. Voxel dimensions were 1 × 1 × 1 mm^3, see Figure 72.

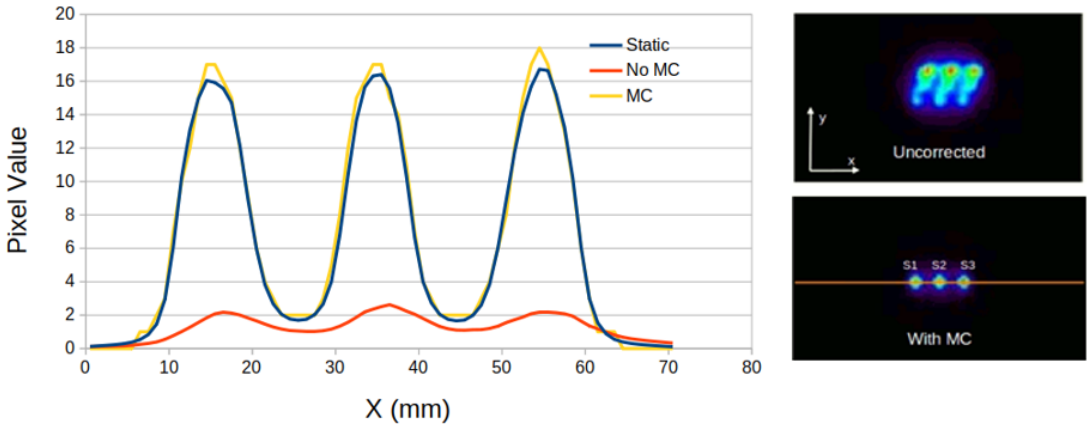

Figure 72. Motion correction of the sources grid moving across the PROSPET3 configuration.

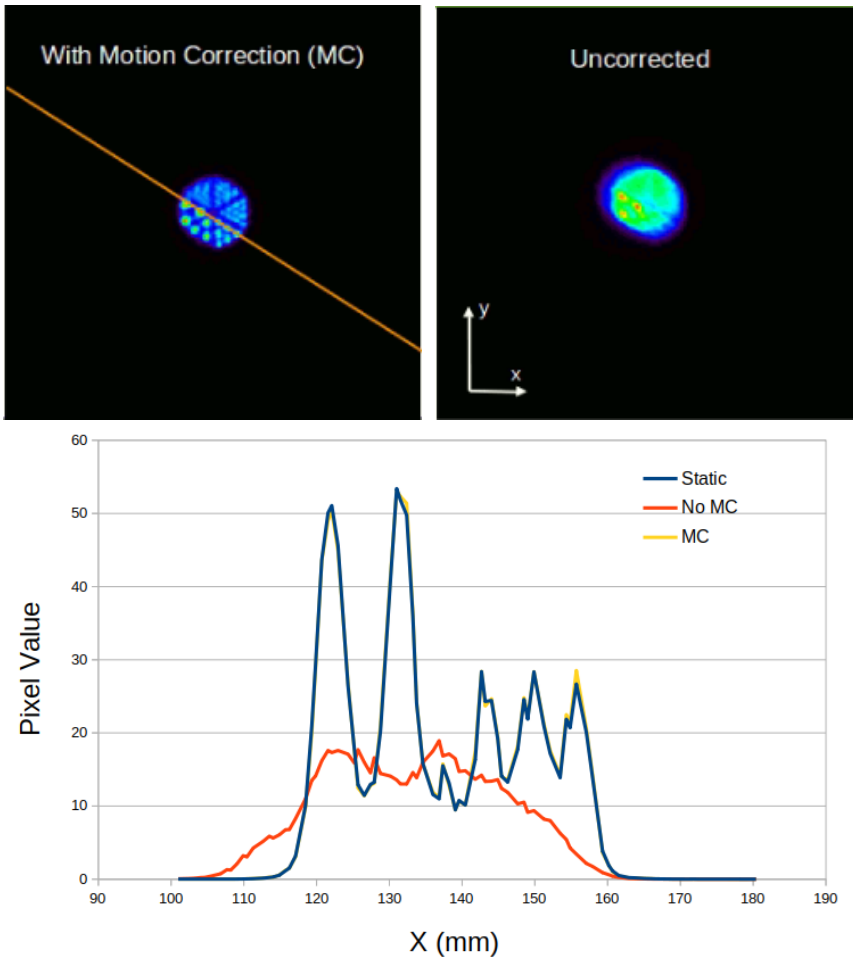

Figure 73. MAF motion correction applied to the acquisition of a Derenzo phantom. Top Left: Final image reconstruction after MAF is applied. Top Right; Image reconstruction with no motion correction. Bottom: Profiles showing the comparison of the static, No MC and MC images.

With the aim to check if the spatial resolution of small inserts remains constant after MAF correction, a Derenzo-like phantom was simulated moving at the axial center, with a random motion in the XY plane. The phantom had capillaries with diameters of 1.2, 1.6, 2.4, 3.2, 4, and 4.8. mm, parallel to the Z axis. Reconstructions of the uncorrected and corrected images used the same parameters and iterations as in the former tests. In Figure 73, the reconstructed

images are shown, together with a profile across the 4.8 mm and 3.2 mm sources, including the case with static acquisition.

4.3.4. Motion correction with experimental data

We have performed motion correction tests with two of the PET prototypes described above namely the PROSPET3 and the CardioPET, the annular prostate-dedicated PET and the heart PET based on two panels, respectively, see Figure 74.

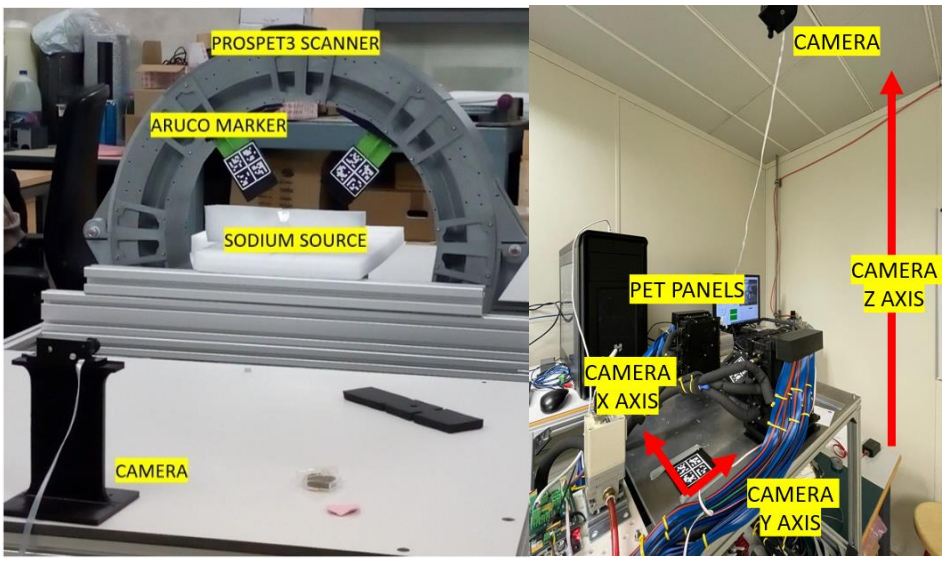

Figure 74. Photographs of the experimental set-ups used for the motion correction measurements. Left: PROSPET3 system with ARUCO markers. Right: CardioPET prototype with two panels.

Camera synchronization. Using the PROSPET3 prototype, we tested the MAF algorithm with real data. A precise synchronization and a good camera spatial resolution are mandatory conditions to generate corrected data. The camera was controlled with a computer and every time an acquisition was started with the camera, a Transistor-transistor logic (TTL) pulse originated at the COM port. This signal is used for synchronization between the camera and the PET acquisition system. When the camera is turned-on, it starts registering the motion of the Aruco patterns. In the acquired PET data, we can identify the TTL pulse and, therefore, the time range the camera acquired data.

Experimental tests. To improve the spatial resolution of the identification of markers, two ARUCO markers were employed instead of just one. The use of more markers helps with possible problems such as bad light conditions or markers with a low pixels contrast. Both markers were attached to the PET ring. Instead of moving the source, the scanner was axially moved following a two-steps motion pattern.

Figure 75 shows the recorded data with the camera for the markers during the experiment, being Z the axial axis of the PET system, which is the direction of motion. The image reconstruction of the uncorrected acquisition results in two well distinguished sources corresponding to the two motion positions, see top-right panel in this figure. After applying the MAF technique and correct for the motion, only one source is found on bottom-right of this figure.

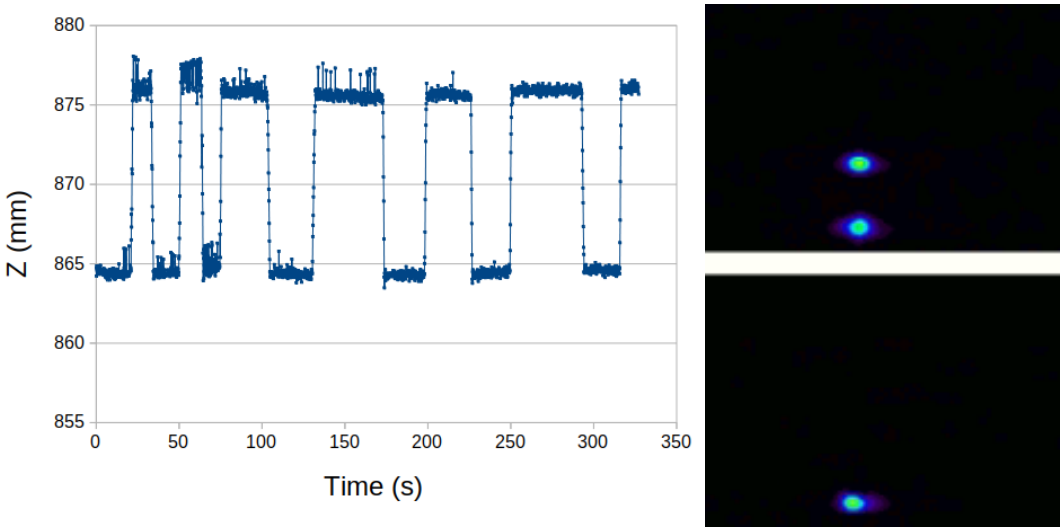

Figure 75. Left: Distance between the camera and the markers as a function of the time. Right: MAF correction of a spherical small source that was shifted axially (top) to get the final image (bottom).

An additional set of experimental tests were carried out with the CardioPET system. The optical camera was placed at the celling of the lab, at 1.2 meters from the PET system. The spatial resolution of the camera exhibits a higher accuracy for the orthogonal plane (XY) than for the Z axis (camera to PET direction). For the orthogonal plane, the spatial resolution for a static acquisition was found to be 0.03 mm FWHM whereas for the Z axis this increases to 0.5 mm due to the camera – marker distance, see Figure 76 bottom. These values were estimated by measuring the marker at a static position for 300 seconds.

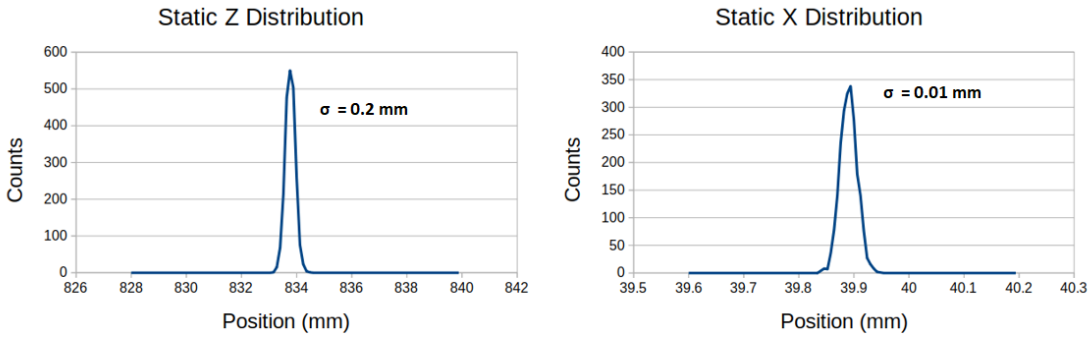

Figure 76. Static camera measurement providing X and Z position accuracy.

A spherical ^{22}Na source with 0.25 mm diameter and 22 µCi was used for the test. We first acquired data with the source in a static position, to be used it as a ground truth for the MAF

algorithm application. Later the source was randomly moved within the FOV with no limitation of speed and motion range (inside the expected FOV). Notice we attached an ARUCO marker to the source. All the motion was tracked and registered with the optical camera. The reconstruction of the source is shown in Figure 77. On the left, the static acquisition and reconstruction is depicted. On the center, we show the uncorrected image reconstruction and, on the right, the corrected image. The OSEM algorithm with 4 iterations and, voxel and pixel sizes both of 1 mm were used. Notice that only two panels of the heart dedicated system were used, and this is reflected in an elongation of the sources in the X axis (left-right in this images). After making use of the MAF technique, the reconstructed image becomes very similar to the static one. Some profiles have been extracted for the static image, the non-corrected and the final post-processed image. In Figure 77 bottom there is a comparison of these profiles. In the case of the non-corrected profile, we have multiplied all the pixel values to 10 just to compare with the other data.

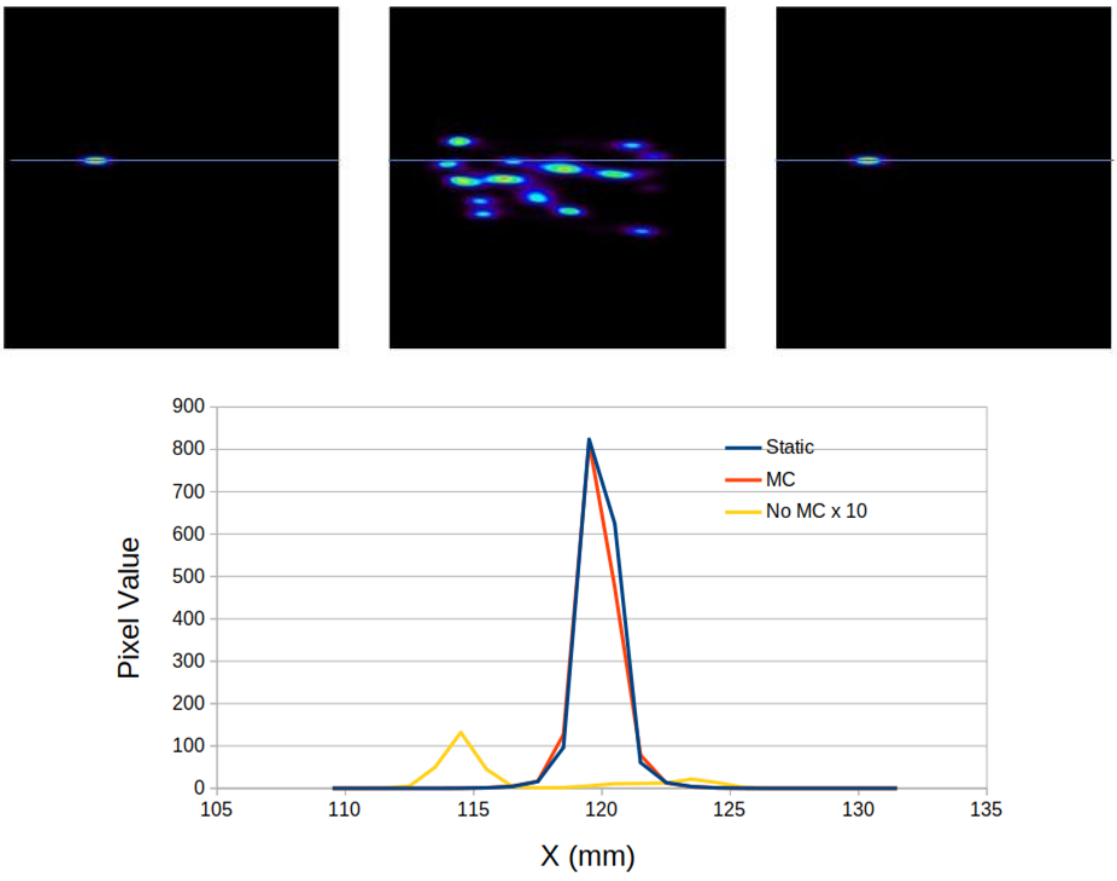

Figure 77. Top Left: Static measurement of a small spherical source in XY plane. Top Center: Reconstructed images of a random motion of a source. Top Right: After motion correction. Bottom: Profiles along the blue line in the top images, of the static initial source position (blue profile), the non-corrected image multiplied by a factor 10 (yellow) and corrected via MAF algorithm (orange).

We have additionally investigated the goodness of the camera and PET synchronization as a function of the object (possible patient) movement speed. For these tests, we have

implemented a rotational stage that moves the source and the marker together. The stage was placed outside the FOV but with the source and marker moving inside of this. Five angular speeds were programmed ranging from 0.384 rad/s to 1.789 rad/s. The radius of circumference was 3.5 cm. We investigated the spatial resolution and capabilities of the camera tracking as a function of the angular speed. Output motion coordinates were fit with a sinusoidal function, and we estimated the residue between the fit function and the real data as an estimator of the precision. The spatial resolution "σ" of the camera is defined as the mean value of all the residue of a coordinate axis according to the speed.

$$\sigma_k = \frac{\sum_n Abs(r_{k,n})}{N} \tag{9}$$

Being *r* the residuum and *N* the total number of samples. In Table 3 the residue values found for each speed and axis are summarized. As the speed increases the optical camera output gets noisy so the residues get higher, especially in the Z direction which is highly related with the focal distance of the camera lens. In Figure 78 and Figure 79 are shown the X coordinate data of the first (0.384 rad/s) and third (1.227 rad/s) speeds as well as the residue values as a function of scanning time.

Speed (rad/s)	Sigma X (mm)	Sigma Y (mm)	Sigma Z (mm)
0.384	0.01	0.84	1.97
0.783	0.06	0.18	2.77
1.227	0.23	0.28	4.93
1.456	0.37	0.43	6.24
1.789	0.94	0.86	Bad Fit

Table 3. Camera spatial resolution according to the motion speed.

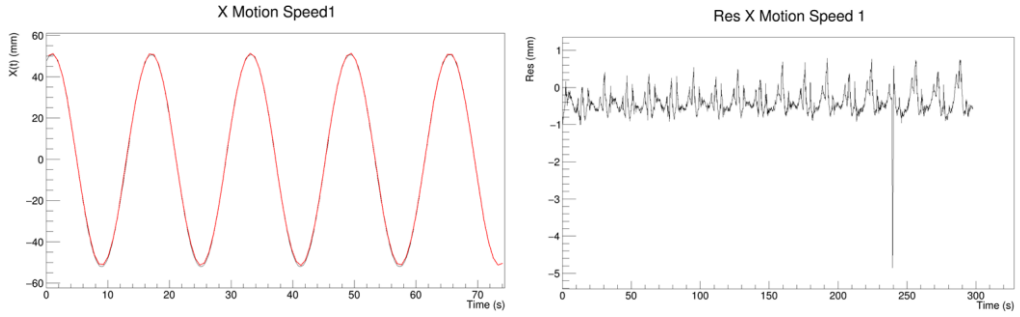

Figure 78. Left: Motion tracking output for 0.384 rad/s speed. Right: Residue obtained.

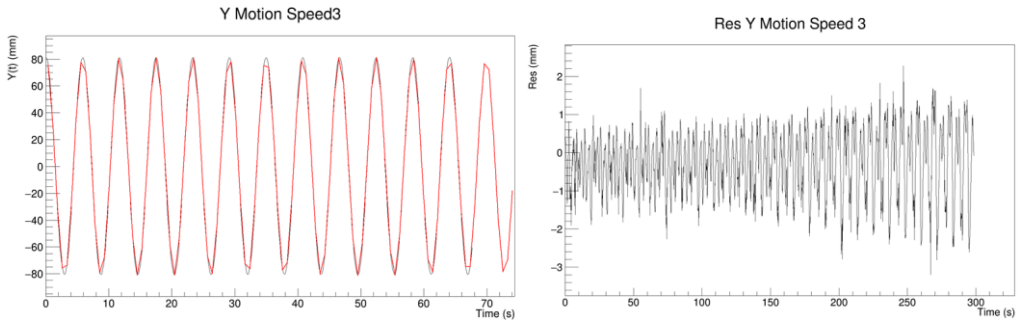

Figure 79. Left: Motion tracking output for 1.227 rad/s speed. Right: Residue obtained.

4.4. ScintoTube: A study for a pre-clinical edgeless PET

An important conclusion of the PROSPET scanner is that monolithic detectors cannot easily achieve accurate CTR, so they are not the best choice for open ring geometries. Nevertheless, they are a good option for ring configurations like PROSPET3 due to their good capabilities such as the spatial resolution and intrinsic DOI. Ring configuration are still a good option for organ dedicated systems, so we were interested in improving the performance as much as possible. Furthermore, PET systems based on ring configurations have advantages over limited angular tomography designs, preserving the spatial resolution due to the total angular sampling. For all these reasons, we suggested a novel PET design based on the ring configuration enhancing parameters such as the sensitivity and the spatial resolution [131][132]. Most of PET scanners are designed following a block detector configuration. Blocks of either pixelated or monolithic detectors are placed in a ring configuration, with gaps in between these detectors both in the axial and in the transaxial directions. This causes a decrease of the scanner sensitivity. This behavior is also observed in pixelated configurations where the pixel size is smaller than the photosensor active area [48].

In order to provide insights on this principle, a Derenzo-like phantom acquired with the Albira PET system was reconstructed for two cases, notice that this system makes use of monolithic 50 × 5 0× 10 mm LYSO crystals. For the first case all the impacts within the monolithic crystals where considered, including those that suffer edge effects. For the second case, we applied a filter for which only impact encountered in the 60% of the central active area were processed, that means avoiding impacts at the edges. 35 iterations with a MLEM algorithm have been employed with 0.25 mm cubic voxel sizes and 0.16 mm virtual pixels. In Figure 80 a comparison between the reconstructed images for the two cases is depicted.

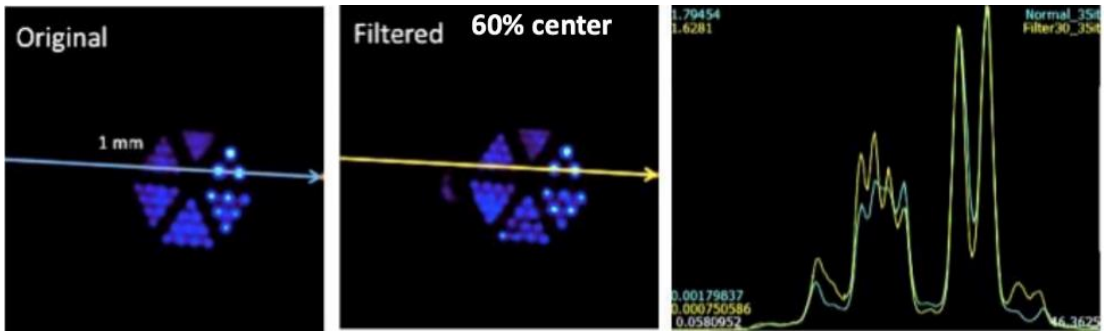

Figure 80. Reconstruction of a micro-Derenzo phantom with the Albira PET system. Left: Considering all impacts in the monolithic crystals. Center: only considering impacts in the inner 60% volume. Right: profile comparison for both cases (yellow only 60% of centered events).

A profile across the 1 mm rods is depicted in the right panel of Figure 80 showing an improvement in the detectability (SNR) of 25% for these rods. Obviously, eliminating the data at the crystal edge is not the solution because sensitivity will significantly decrease. There are some methods that could allow one to better determine the impact position at the edges of the scintillator such as machine learning or Neuronal Networks [87]. However, these methods still cannot compensate the number of LORs missing due to the gaps in between detectors.

4.4.1. Prior works

Probably the first prototype that studied the feasibility of an edgeless scanner was proposed by S. Genna and A. P Smith [133]. It consisted of a SPECT scanner made with NaI scintillators, called ASPECT, with an inner diameter of 31 cm and 8 cm width. Regarding PET systems, in 2019 a small animal system was simulated using GATE, by K.J. Wilson and others [134], using GLuGAG:Ce as scintillation material. The scanner had an internal diameter of 46 cm and 30 cm length. An additional edgeless scanner, built with LYSO scintillators was presented by J. Xu [135]. This PET system was composed by a single monolithic crystal of 48.5 mm inner diameter coupled with a curved SiPM array. The AnnPET was introduced by A.V. Stolin [136], and tested with the NEMA NU4-2008 by using the GATE platform. The external surface of the cylinder was faceted this time, with an inner diameter of 50 mm, and outer diameter of 75 mm and an axial length of 72 mm.

4.4.2. Prototype ZERO: facetted faces

With the aim of developing a PET system which combines the benefits of a ring configuration and solves the aforementioned limitations, we modelled a single continuous tube with simulations at first. That means a single monolithic annular scintillation crystal (LYSO) with no dead areas or gaps. Therefore, for this configuration, due to the absence of crystal edges in the transaxial plane, the spatial resolution will potentially improve. Moreover, the lack of gaps will increase of LORs collection, enhancing the system sensitivity as well.

The most extended process to manufacture a scintillator crystal, like LYSO or BGO, is the Czochralski method [137]. This was initially developed by Jan Czochralski in 1916, using seeds to grow crystals. By controlling the temperature and other factors the scintillator block can be shaped with precision. Notice that an average size of a LYSO ingot is about 90 mm in diameter and 150 mm in length.

The PET system was modelled consisting of a LYSO tube with 60 mm inner diameter, and 80 mm outer diameter and 52 mm axial length. With the aim to also construct this design experimentally, and to integrate commercially available SiPM arrays, the outer surface was faceted in 10 faces, see Figure 81.

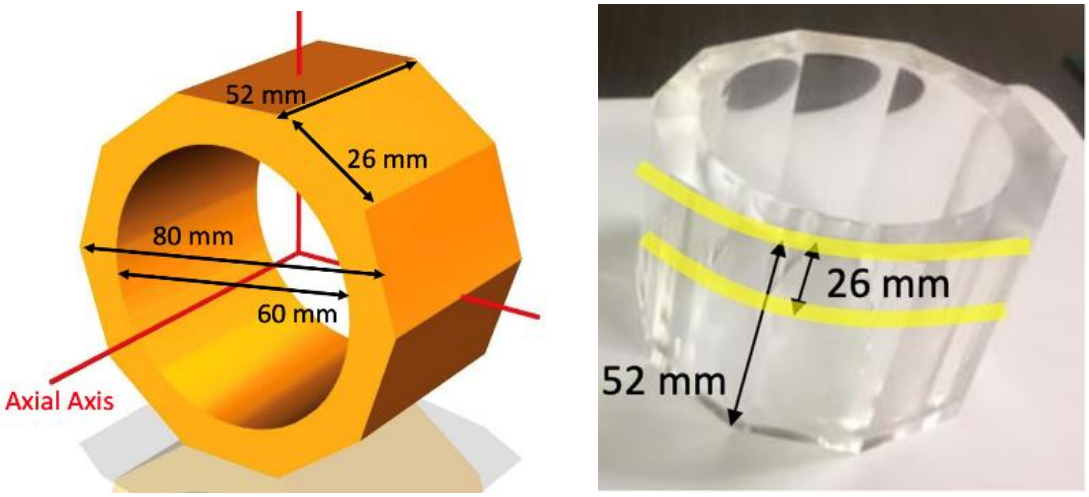

Figure 81. Left: Sketch and dimensions of the crystal geometry for prototype zero. Right: Photograph of the crystal tube.

4.4.2.1. Optical simulations

Simulation studies with optical photons have been carried out to understand how the light is spread in this novel geometry. All faces were polished. Regarding the crystal treatment, all surfaces except the facets that are coupled with optical grease to the SiPM arrays, have been black painted. Thus, only OP that directly reach the SIPMs are considered. When a coincidence event has occurred and scintillation light has been recorded, all the system is analyzed looking for two different light distributions at rather opposite sides of the system. LD are projected and sampled onto the 80 SiPMs of 3 × 3 mm^2 active area in the transaxial axis, see Figure 82. This information is relevant for the simulations because this will be the sampling used during the optical modelling. Once these two projections are obtained, CoG or RTP techniques are applied to determine the centroids, as previously described. DOI estimation is obtained using the N/I estimator [48].We have only characterized the scintillation light within the central 26 mm axial crystal length since, as it will be later described, our implemented prototype only considers photosensors in this area.

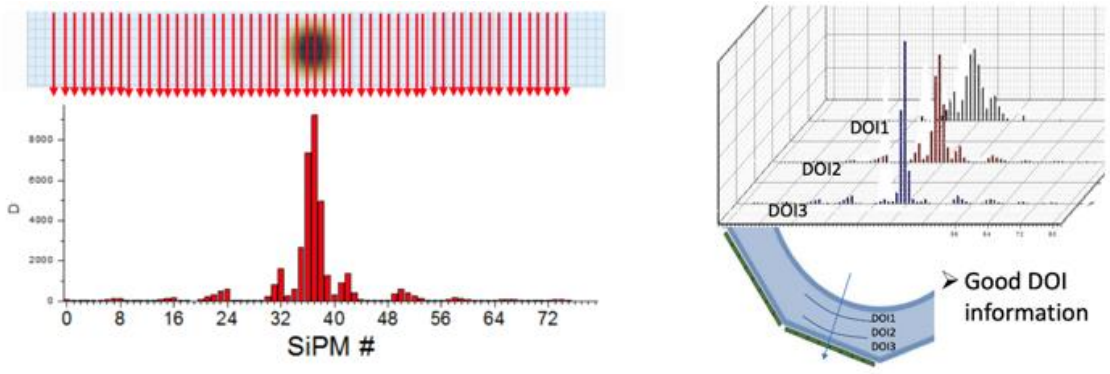

Figure 82. Left: LD projection along the transaxial axis. Right: LD for different DOIs.

Our first findings when using optical simulations and the described crystal geometry, was noticing that the light distributions in the transaxial axis reveals the appearance of tails with valleys (low counts), as depicted in Figure 82 left. If the annihilation photon interacts near the scintillation crystal entrance, the light distribution is wider, worsening this effect and larger tail contributions are registered. We observed an energy dependence with the impact DOI, so this effect should be considered in the calibration process. In this PET scanner, light is shared between multiple SiPM arrays and, thus, facets. For gamma rays that scintillate closer to the entrance surface, their light distribution would present more components in other SiPM arrays, in comparison with impacts closer to the photosensor layer [131].

To study the reduction of light scintillation truncation and, thus, edge effects, we simulated light sources within the annular monolithic block at different angular positions (transaxial positions), see Figure 83 left. We were interested in the center of the facets (angles 0 and 36 degrees), also positions in two facets joint (18 and 90 degrees) and a few intermediate positions. With these few simulations, we want to assure that CoG algorithm will work both in the facets center and in the joints, and no compression should be noticed in the transaxial axis. Notice that the axial axis will still suffer for some compression effect due to its finite dimensions. The position was estimated using the CoG algorithm and compared to the true positions. As shown in Figure 83 right, there is not compression effect observed. If there is no compression and the system is able to characterize the local coordinates with more precision in the transaxial axis, it is expected that the system spatial resolution will improve.

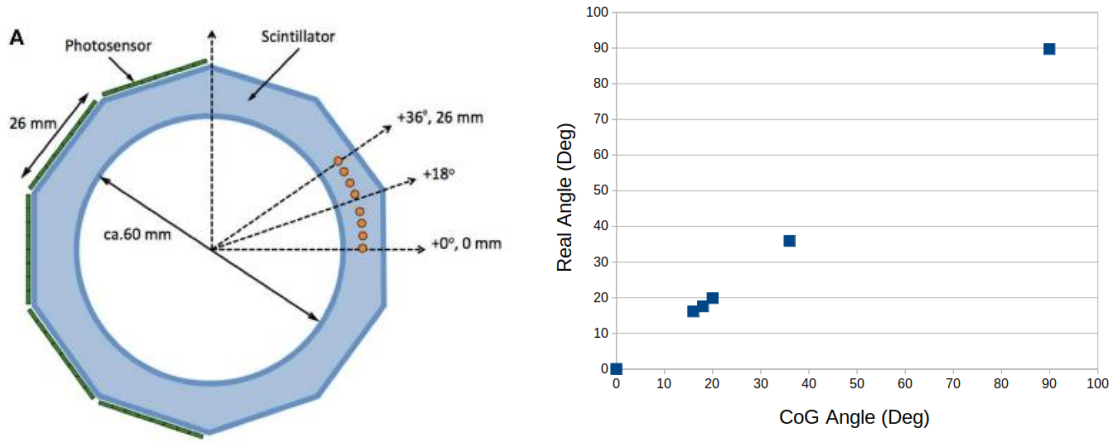

Figure 83. Left: Position of the emission sources. Right: CoG calculation for the transaxial coordinates.

4.4.2.2. Nuclear simulations

In addition to the optical simulations, we evaluated the PET system performance using nuclear simulations. The expected detector spatial resolution for the transaxial and axial axes was set to 1 mm, and 2 mm for the DOI component. These parameters were estimated based on former tests and expected system performance. The energy resolution was defined as 15% around the 511 keV photopeak. For these tests, the coincidence time window was set to 2 ns.

In a first step, we have studied the sensitivity response of the system. A small spherical ^{18}F source with 0.25 mm diameter and 22 kBq activity was simulated along the axial. Sensitivity at the FOV center achieves 5.3%. Similar data was taken with the experimental system my assembled [131]. In Figure 84 a comparison between simulated and experimental sensitivity axial profile is depicted, for 30% energy window.

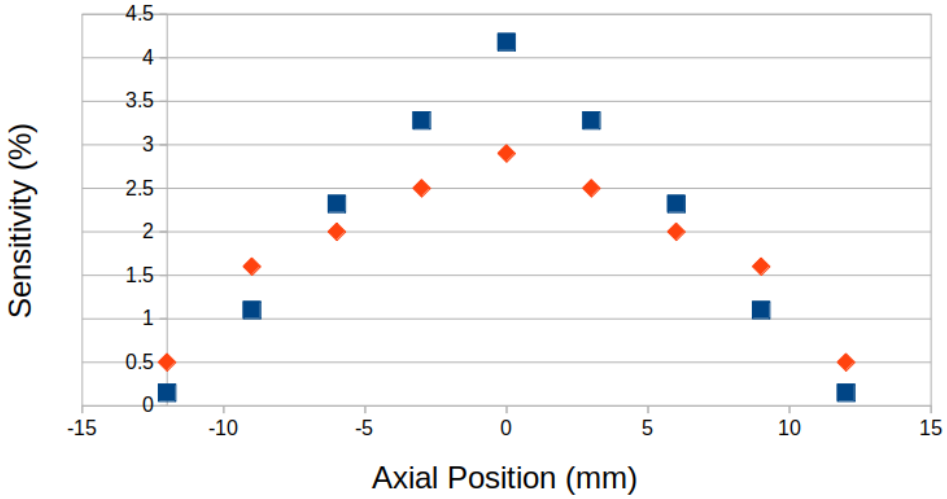

Figure 84. Simulated (blue spots) and experimental (orange spots) sensitivity profile comparison.

The simulated data was reconstructed using an OSEM algorithm with 4 iterations and 10 subsets. The reconstruction process made use of voxel sizes of 0.5 × 0.5 × 0.5 mm^3. In order to

account for the normalization correction, an annular phantom was simulated with GATE. The idea is to reproduce a normalization map similar than the prostate PET scanner, see section 4.1.4. The diameter of the annular phantom was 31 mm with 2 mm thickness and 25 mm axial length. This phantom was filled with radioactive ^{18}F water with 10 mCi, see Figure 59.

We also modelled two ^{22}Na sources of 1 mm diameter separated by 15 mm. The image reconstruction of these sources is shown in Figure 85 left, along with a profile across them, see central panel. This figure also includes a 3D reconstructed image of the annulus phantom used for normalization.

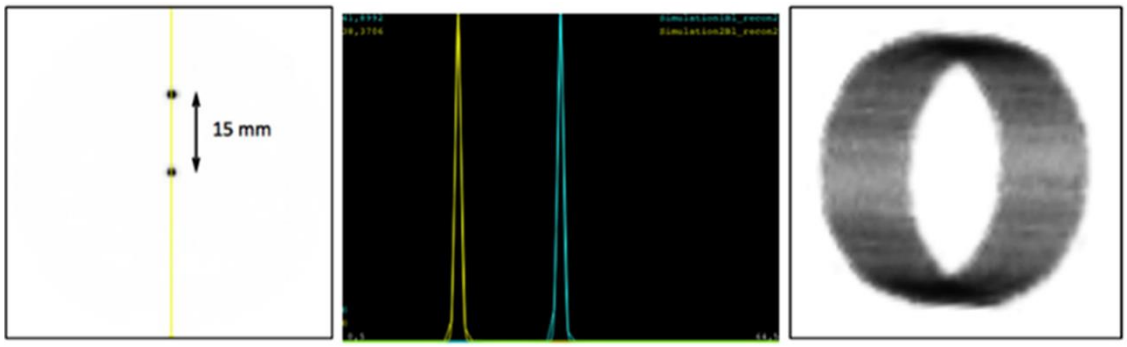

Figure 85. Left: Two spherical reconstructed sources. Center: Profiles along the sources. Right: Image reconstruction of the normalization ring.

The image capabilities of the simulated system were also tested with a Derenzo - like phantom placed at the CFOV, whose size is 31 × 31 × 26 mm^3, see Figure 86. The same reconstruction parameters were used. The phantom consists of rods with diameters of 1, 1.25, 1.5, 2 and 2.5 mm, and filled with 200 kBq of ^{18}F with no background radiation. Normalization correction has been applied to the reconstruction of the Derenzo phantom using the annular measurement. One of the large rods was filled with 10 times less activity. A profile across the smallest rods is depicted on the right of the same figure. As a conclusion, this PET scanner presents a good behavior in terms of spatial resolution, resolving the smallest rods.

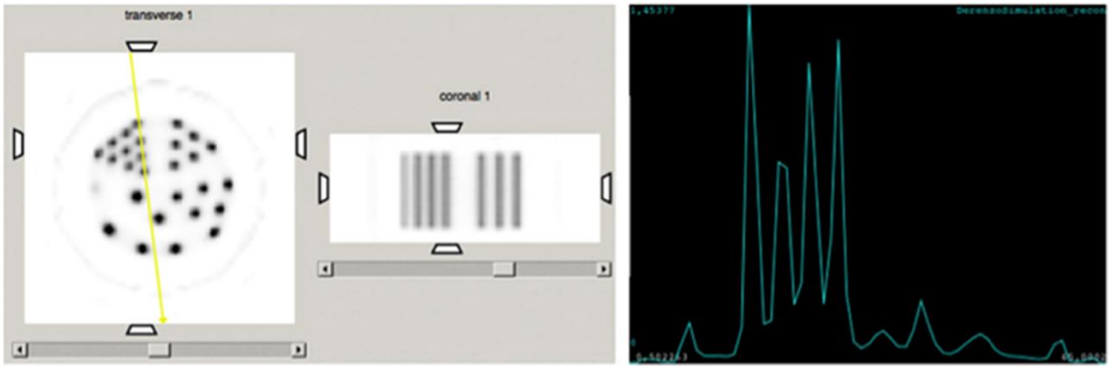

Figure 86. Left: Two views of the Derenzo phantom reconstructed. Right: Profile along the yellow line.

Trues, random and scatter event rates have been simulated following the NEMA NU 2008 protocol. A cylindrical high-density polyethylene phantom, with 25 mm diameter, was placed at the FOV center. A drilled hole, shifted 10 mm off the phantom center, was filled with ^{18}F water. The initial activity was 0.34 mCi. The maximum value of the NECR was found at 46 kcps at an activity of 0.27 mCi, see Figure 87, which is considerably lower than other preclinical systems. According to the small contribution of scatter and random rates in comparison with the true rate implies that the reason that the system saturates so early is because of the high amount of pile-up events due to large photodetector area. After simulations, as in the case of the sensitivity, we have experimentally measured the NECR rates following the same NEMA protocol, see Figure 87.

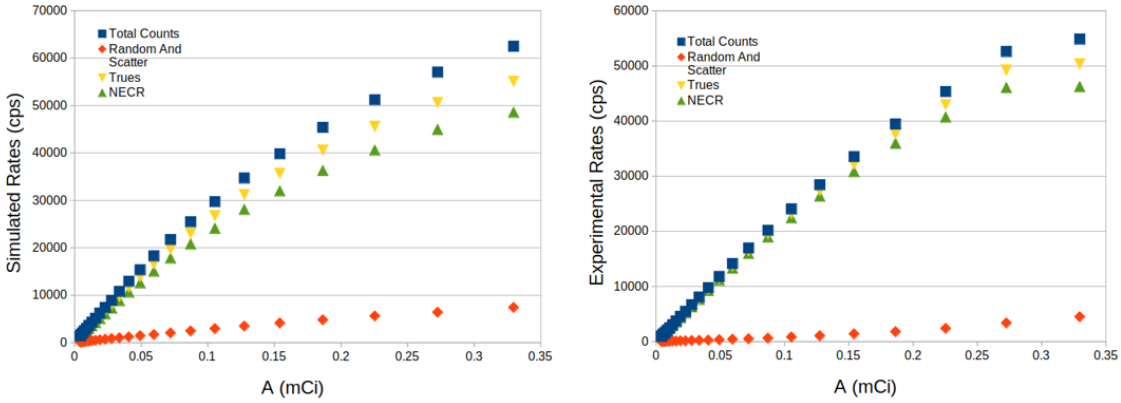

Figure 87. Left: Simulated rates results. Right: Same but the experimental data.

Spatial resolution was characterized also experimentally with a small spherical ^{22}Na source placed at the FOV center and then in several places across the transaxial axis. For the source at the center, sinograms obtained show a misalignment, especially in the transaxial sinogram, caused by problems in the position calibration. Considering that the reconstruction would lead to artifacts, spatial resolution was determined by the width of the sinogram once it was projected for all angles. In Figure 88 we can study how the spatial resolution varies according to the source position.

4.4.3. Prototype ONE: UVa project, cylindrical geometry

As it has been described above, the estimation of impact coordinates in the previous configuration was complicated due to the tails induced by the facets. Our group has been recently (2021) awarded with a grant from the National Institute of Health in USA (reference 1R01EB029450-01), for the design and fabrication of a similar annular system design but without the facets in the outside surface. Simulations were very important for the initial steps to study the scanner performance and to design the reconstruction algorithms. In particular, the PET

scanner makes use of a perfect cylinder with inner and outer diameters of 62 mm and 80 mm, respectively, and an axial length of 96 mm. The system is surrounded by arrays of 72 × 27 SiPMs (transaxial × axial) with 3 × 3 mm^2 active area each and 3.56 pitch. This array is divided into 24 sub-arrays of 9 × 9 SiPMs each, 8 transaxial and 3 axially. A sketch of the LYSO tube can be found in Figure 89. With the removal of the external facets and the incremented axial FOV, we expected an improvement in the scanner capabilities.

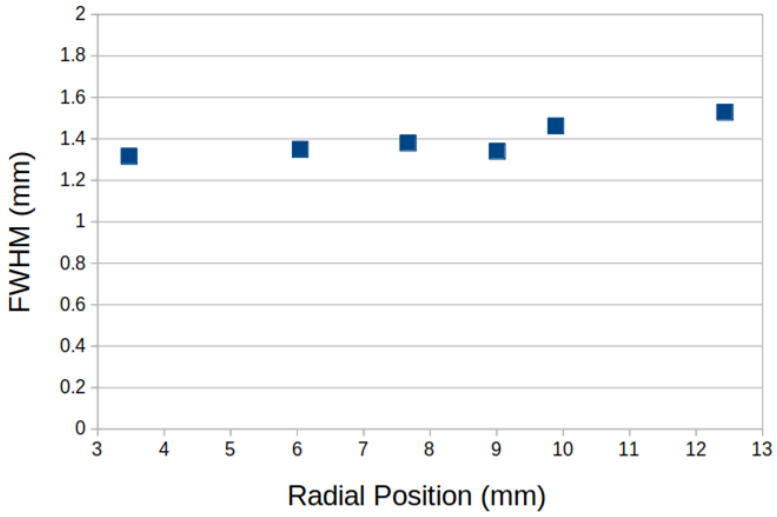

Figure 88. Spatial resolution of a small spherical source moving across the radial axis.

We have studied the percentage of the different iteration types within the whole scintillation crystal. Secondary interactions shift the coordinates of the first interaction, causing a blurring in the impinging position, due to the unknown true LOR. We have represented this effect in Figure 90. More than 50% of the gamma rays only suffer one interaction within the LYSO crystal, whereas only 30% of all events are pure photoelectric. Only pure photoelectric events have no coordinate degradation and deposit the total amount of the 511 keV gamma ray at the same time. As expected, the probability of multiple interaction decays until 4% for more than 3 iterations. The annihilation photons that suffer more than one interaction within the LYSO material will be the ones that degrade the spatial resolution. Nevertheless, if we compare the final CoG coordinate with the initial one, only around 30% of them will exceed more than 1 mm degradation.

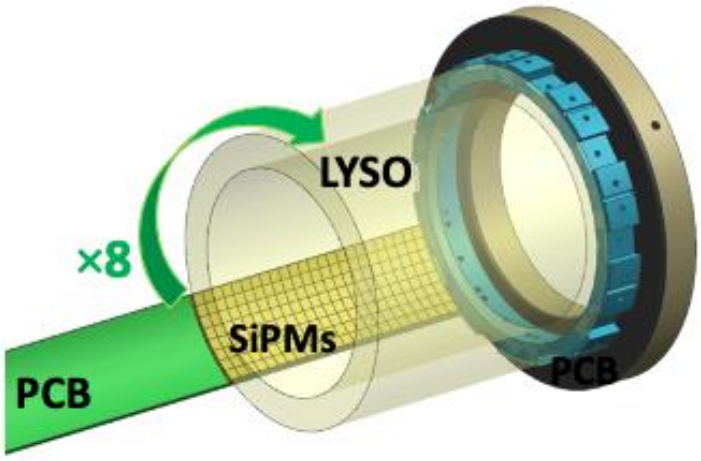

Figure 89. Sketch of the experimental mounting, showing the detail of one printed circuit board (PCB) with 9 × 27 SiPMs each.

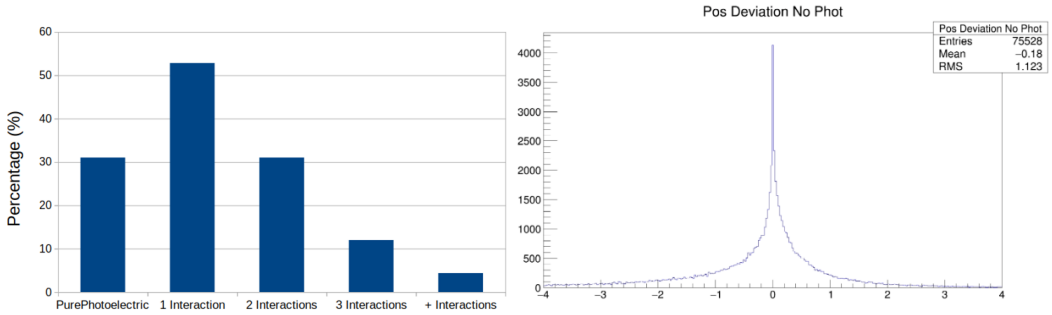

Figure 90. Left: Hits distribution within the scintillator tube. Right: Spatial deviation for multiple scattered events.

4.4.3.1. Optical simulations

In the optical simulations we especially focused on the shape of the collected LD. Notice the facets in the previous design generated profiles with some artefacts, that should be mitigated in the current design. A source of optical photons was placed at three different DOI positions. Notice that the scintillation tube was simulated having all crystal surfaces polished and black painted. The three light distributions along the transaxial axis are shown in Figure 91 left. No tails were observed, and DOI information can be estimated using the N/I estimator from each projection. For research purposes, the inner cylinder surface was covered with a RR material and thus increasing the scintillation light collection in comparison with the black painted case. In Figure 91 right, two LD of a source emitting in the same position but with different surface treatments is also shown.

The LD shapes were corroborated with real acquisitions on a system that we built following the described geometry. Figure 92 shows, for two different DOI positions, both experimental and simulated LD normalized each other to their maximum value. Some minor small differences are induced by the non-perfect black surface of the prototype.

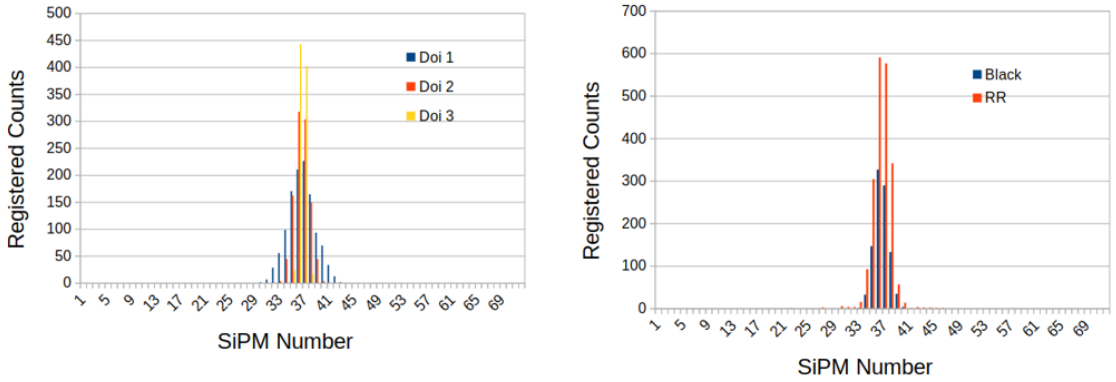

Figure 91. Left: LD Projections when using an entrance RR layer at different DOIs. Right: RR and black LD comparison.

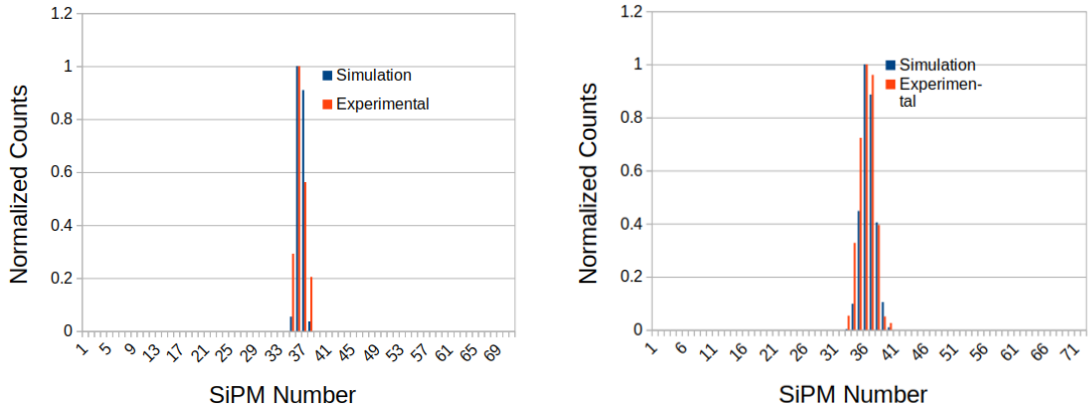

Figure 92. LD comparison between simulation and experimental. Left: LD for and event close to the SiPM surface. Right: same but closer to the gamma ray entrance surface.

The CoG, and RTP2 as well, algorithm is applied to the light distributions to estimate the radial and axial impact coordinates. Once the energy and the position of the maximum peak distribution event is stored, the algorithm looks for a second maximum peak beyond all the SiPM involved in the first interaction and then repeats the process. If a second maximum peak is found, and the total energy calculated with their neighbors exceed a certain level, then the energy and the coordinate is stored as well in a LM file as a coincidence event [131].

4.4.3.2. Nuclear simulation

We have estimated the axial sensitivity with a spherical source moved across the axial axis. For this test, only nuclear simulations were used. The source had a low activity of 10^5 becquerel, so random, scatter, deadtime and pileup effects are negligible. Based on the optical simulations described above, energy resolution was set to 15%. Two energy windows were considered, 30% and 50% around the photopeak. Figure 93 shows the sensitivity curve, exhibiting the maximum value of 11% at the CFOV.

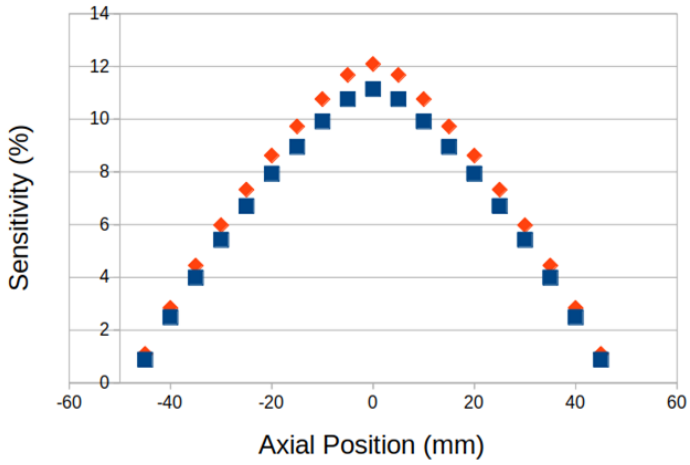

Figure 93. Sensitivity along the axial axis for 30% (orange) and 50% (blue) energy windows.

4.4.3.3. Simultaneous nuclear and optical simulations

Mixing both nuclear and optical simulations in the same run implies a large amount of data memory in the computer, so for this work the total simulation was split and computed in a CPU cluster. A completely new routine was designed just to work with different stages, starting with the nuclear simulation, continuing with the cluster optical simulation and finally the conversion into a LM file. Everything was systematized with a high computational cost. Since we have stored the nuclear interaction of the gamma rays, both photoelectric and Compton events, we can identify all the light distributions that are stored in the output file and only keep the coincidence events, reducing the total amount of data. For this configuration, light distributions present two different peaks corresponding to the single events, that form the coincidence, which have deposited the energy in different places in the scintillation tube. The algorithm applies the CoG for both distributions, estimating the impact position and the energy deposition for each single. A LM file is generated with all the information so it can be used as an input file for the reconstruction program.

A back-to-back 511 keV gamma source, with 0.25 mm in diameter, was simulated at the scanner center FOV. All the coincidences in the tube generated light distributions and were stored to post-process them. The energy spectra were calculated as the histogram of the light collected for each event in all SiPM fired. We have observed an energy gain dependence with the impact DOI as shown in Figure 94 top. This effect can be calibrated for reconstruction purposes. The energy resolution exhibited values close to 15% for the case of having the surfaces black painted. The same source was used for simulations considering a RR layer coupled to the inner surface of the tube, see Figure 94 bottom. We can again observe an energy dependence with the DOI, but a higher gain is in general found due to the use of the RR.

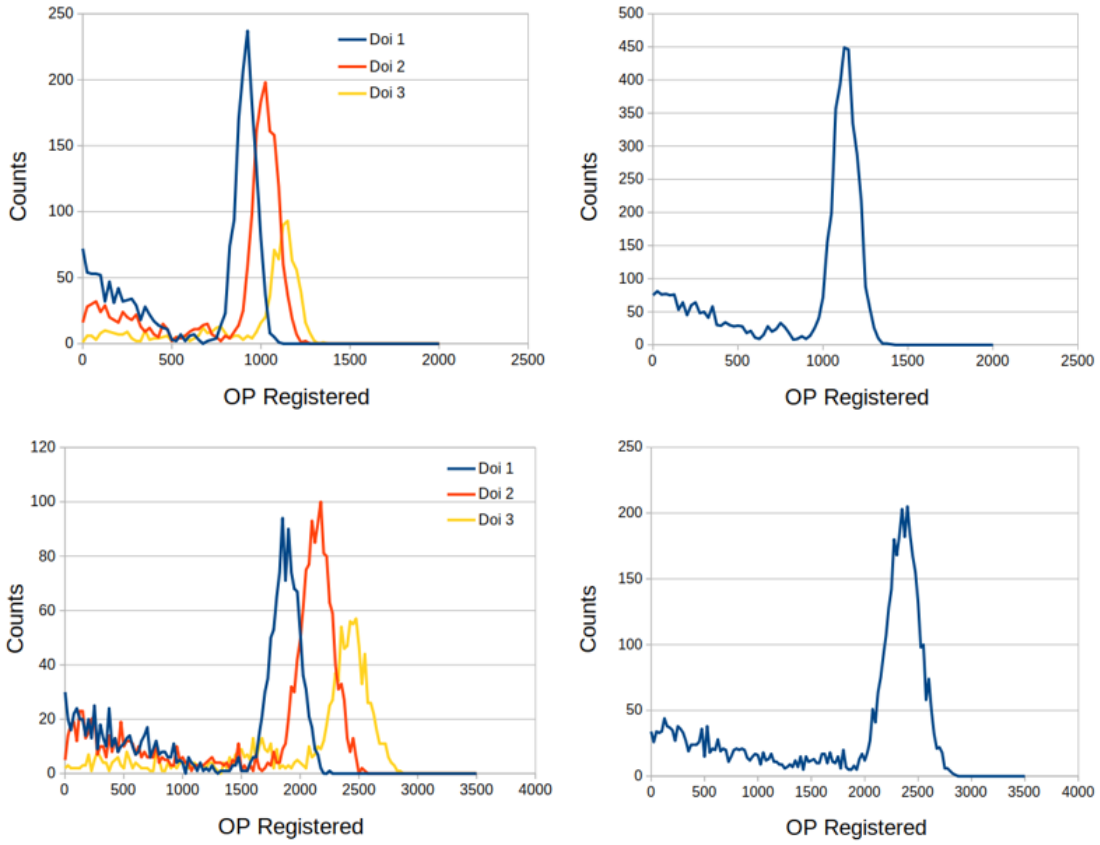

Figure 94. Top Left: Energy spectra for the black surface and different DOIs. Top Right: Same spectrum after energy calibration. Bottom Left: Energy spectra for the RR surface for different DOIs. Bottom Right: Same spectrum after energy calibration.

We integrated the system geometry in the CASToR platform for image reconstruction. We have used an OSEM algorithm with a crystal virtual pixel size in the transaxial plane of 0.8 mm and 0.5 mm in the axial axis. The image space was defined with voxels of 0.5 × 0.5 × 0.5 mm. The DOI estimation was used to correct to the true LOR, compensating for the parallax error. The normalization correction was implemented using a cylindrical phantom with a diameter of 40 mm and 96 mm axial length. DOI correction was also included into the normalization data. To evaluate the whole simulation and reconstruction processes, the back-to-back 511 keV ^{18}F sources of 0.25 mm in diameter were placed along the radial axis in steps of 5 mm with 10 iterations, see Figure 95.

NECR, trues and random rates have been evaluated, following the procedure described for the facetted tube and the prostate-dedicated system. Notice that every time a coincidence event has occurred, the system reads the information of the arrays of photosensors trigger, but also all the information of neighboring arrays (up to 9+9 arrays for each even in the coincidence). This situation is mandatory to benefit from the whole light distribution and avoid its truncation. However, by reading a big amount of SiPM signals within the same integration time (250 ns), the probability of pile-up events increases for high activities. As shown in Figure 97, the NECR

maximum value was found at 110 kcps for 100 µCi activity, which is considerable higher than the first prototype according to the increase in the axial dimensions. Working with such a low activity range, random events are residual and barely affect the NECR curve.

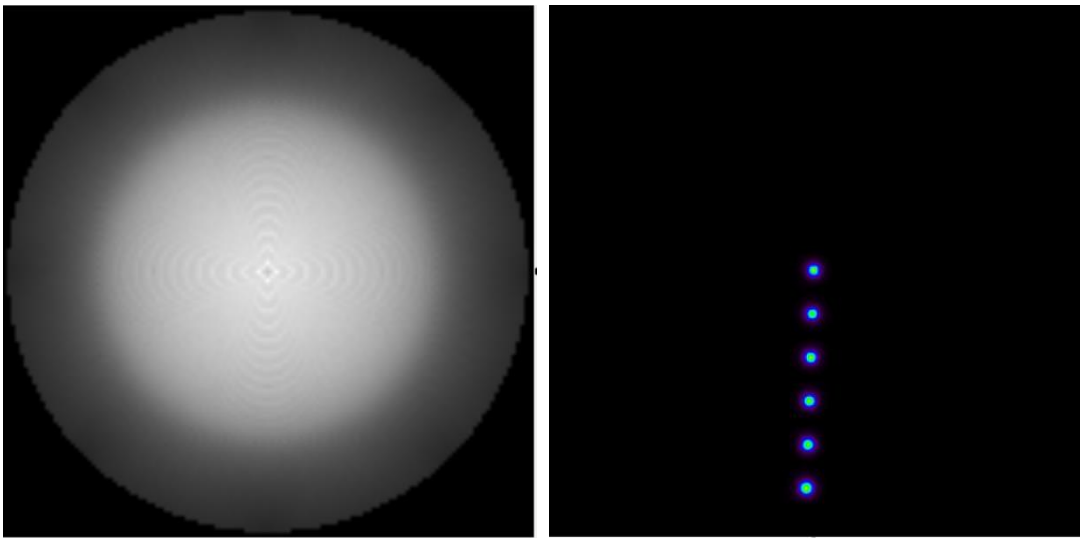

Figure 95. Top: Normalization image. Bottom: Reconstruction of several simulated sources.

The spatial resolution was characterized by calculating the FWHM for each source, see Figure 96. DOI correction was applied with the N/I estimator and then by projecting the local coordinates to the inner surface of the tube scanner.

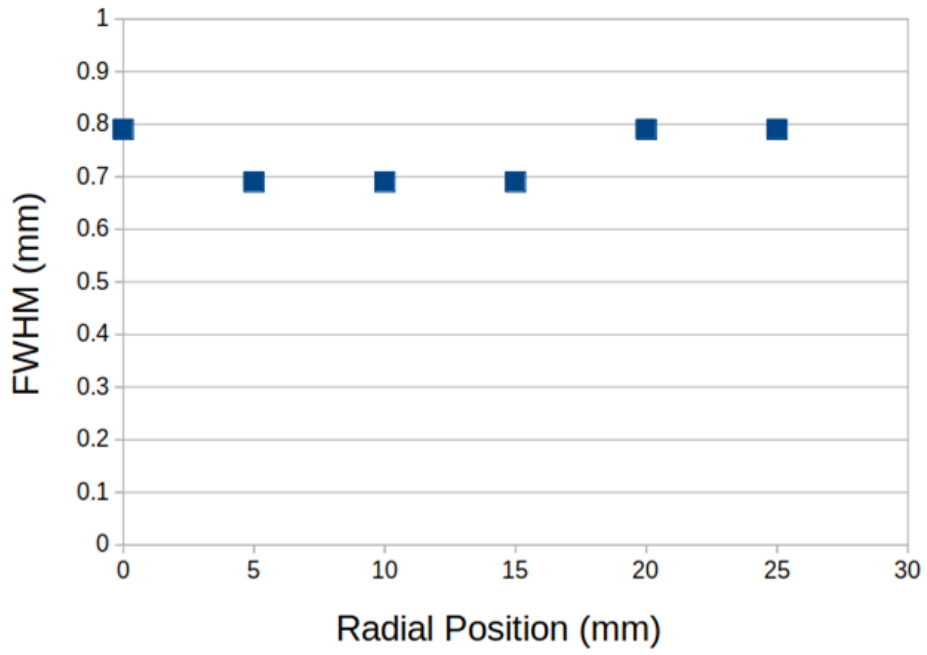

Figure 96. Spatial resolution with DOI correction for different radial positions of a small size source.

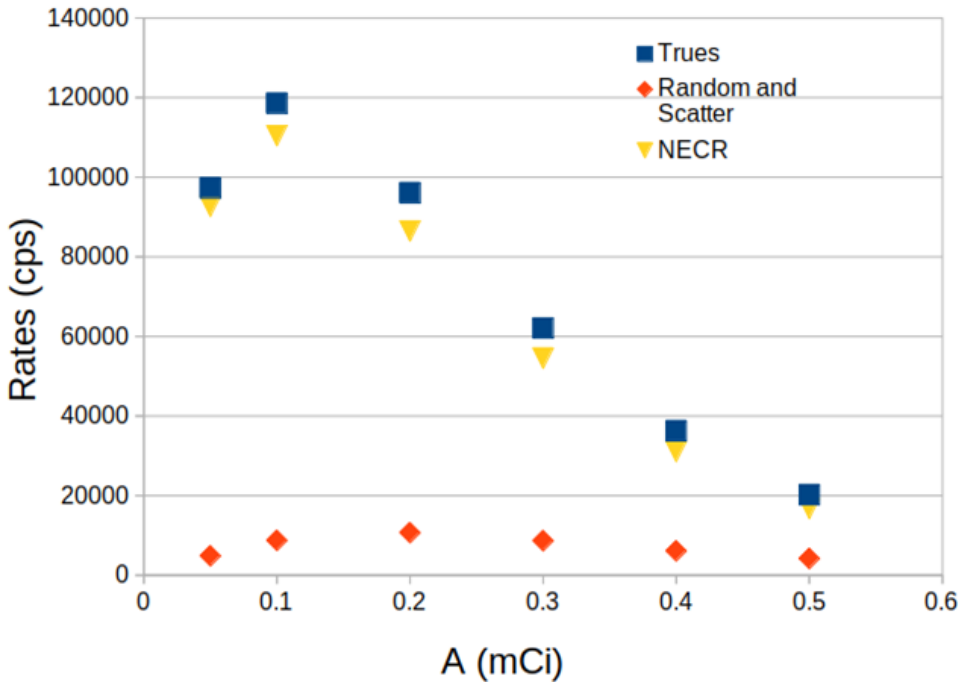

Figure 97. Simulated count rates for a 30% energy window.

This novel geometry suggested us to restructurate the methodology of the post processing of data as well as the image reconstruction process. We tested experimentally and via simulations this configuration in the described pre-clinical system with the aim to also extrapolate this design in the future to an organ dedicated PET. In Table 4**Error! Reference source not found.** we show the performance of both prototypes.

ScintoTube Prototype	FOV Dimensions (mm)	Sensitivity (%)	Spatial Resolution cFOV (mm)	NECR maximum (kcps)
0	31 × 26	3.00	1.3	47
1	32 × 96	11.00	0.8	110

Table 4. Main performance of the two ScintoTube prototypes.

5. DISCUSSION

In this thesis we have studied the capabilities and performance of two organ-dedicated PET prototypes, as well as of a novel edgeless pre-clinical PET system. All these prototypes were simulated with GATE framework with the aim to study their performance before the mounting. Simulations were important to decide the final geometry and to estimate the performance of the scanners optimizing their characteristics. Energy and spatial resolution of the detectors were estimated with both optical simulations and previous experimental research. These scanners were partially tested experimentally and compared with previous simulations. In parallel to this extensive analysis, simulations of multiple radioactive sources moving inside the FOV were performed to apply motion correction algorithms. Furthermore, the MAF was also tested with the use of an optical camera able to register the motion. Moreover, the experience obtained working with these simulations was extended to other projects that are not included in this thesis, like a breast organ-dedicated system with a similar geometry configuration than the pre-clinical PET, and a Total-Body PET with TOF and DOI capabilities.

The system called PROSPET, was designed to visualize with molecular imaging (PET) the prostate organ. One of the aims of this project was to work with monolithic LYSO blocks with RR layers, due to their enhanced spatial resolution together with DOI capabilities. With this prototype, we want to show how this detector modules can improve a scanner performance, so

they can be taken into account for other future projects. With them, we were expecting an improvement in the quality image by increasing both sensitivity and spatial resolution. LYSO crystal dimensions with 50 × 50 mm and a thickness of 15 mm to assure a good sensitivity, were considered. Adding a RR layer at the entrance face of the crystal, the scintillation light bounces back to the emission point enhancing the detector spatial resolution to 2 mm, together with and an energy resolution of 15%. Lateral surfaces were black painted to reduce the OP reflections, preserving the LD for a good intrinsic spatial resolution. The use of monolithic detectors allows the DOI determination, correcting the parallax error for sources far of the FOV center. An aim was to keep a reduced number of detectors, and just 24 were used. One of the goals of these kind of scanners is to maintain its prize as low as possible so increasing the number of detectors is not a desired situation. The first design idea was to allocate the detectors in a two-panels symmetric configuration. After an anthropomorphic study with patients (n=22), 12 detectors were used in each panel, with a panel-to-panel separation of 28 cm. The sensitivity maximum takes place at the FOV center, reaching 5% of events registered. However, the prostate is on average placed off centered by about 40 mm, where the sensitivity is not optimized in this dual panel scanner. With the simulations, we found that the lack of angular information would be a problem when dealing with phantoms more complex than small spherical sources.

A second prototype was studied according to the known prostate location. Two PET panels were built but one of them contained 18 modules and the second only 6, preserving the total number of detectors modeled and experimentally built. In this second prototype, the sensitivity maximum of 4% is 40 mm off centered, a result slightly worse than the previous iteration. Simulations of a Derenzo phantom suggested an elongation in the final reconstructed image (in the panel-to-panel direction). This phenomenon was also present in the patient study. Even if the small lesion in the patient was detected with this prototype, a poor image of the prostate was found. This occurred due to the lack of some angular information, and also the missing correction of normalization and attenuation, together with the missing TOF information. Radiation coming of the kidneys might also interfered the acquisition. TOF information is mandatory in scanners based on limited angle tomography geometries. Monolithic detector blocks cannot easily provide a time resolution enough to consider them as an option, although relevant works are currently undergoing [129].

The lack of accurate timing capabilities in this development, suggested a redesigning of the PET scanner following an annular geometry. The 24 detectors were arranged in a single ring PET scanner, with 41 cm in diameter. Despite the conventional ring geometry, it can still be considered as an organ specific system due to the proximity of the detectors to the patient. This

scanner can be opened to facilitate the patient accommodation, and, due to its reduced dimensions it would be possible to practice an in vivo biopsy study. Sensitivity maximum value takes place at the FOV center but lower than in previous prototypes, reaching this time 1.4%, due to the larger FOV extension. Nevertheless, it was still comparable to WB-PET systems, whose sensitivity is around 1%. In terms of the sensitivity, simulation values exceed the experimental, suggesting some data loss which is not included in the simulation. Normalization and sensitivity corrections were implemented using a coronal phantom instead of a solid cylindrical one. The annular phantom reduces most of the scatter produced in the active volume. Nevertheless, for each phantom or patient acquisition it was mandatory to provide to the reconstruction an attenuation map. An important advantage of monolithic blocks is the capability to accurately estimate DOI, so the parallax error can be partially corrected, as in the previous scanners. When DOI estimation is enabled, the spatial resolution with the prototype remains below 3 mm in all the transaxial FOV. However, if it is not enabled, there exist a degradation along the radial axis. Spatial resolution in PROSPET3 was similar than the symmetrical panel in the FOV center, with the advantage of the non-distortion of the source due to the lack of angular information.

We evaluated the prostate-dedicated PET ring with a cylindrical phantom including fillable spheres with different diameters. We worked with two different activity concentration ratios of spheres – background. Before we acquired data with the ring scanner, the same phantom was tested with a commercial PET, the TOF-PET Gemini scanner from Philips. In terms of CNR, both scanners exhibited a similar behavior for the smallest inserts, being the commercial scanner superior for the largest. However, in terms of contrast, the dedicated PET provides a better result for the smallest spheres and similar for the largest. This result is a direct consequence of the enhanced spatial resolution of the prostate-dedicated PET system. The final test was to acquire data with patients with diagnosed PCa. The clinical data that we showed in this work had two hotspots with high radiotracer concentration at the prostate region. A CT image was used as an attenuation map and the images co-registration were carried out with the ITK software [130]. Despite both hotspots are resolved by the dedicated scanner, the image quality is degraded due to multiple factors. First, the activity outside the FOV produces random events that blur the image. The second one is the lack of accuracy in the co-registration of the PET and the CT images. An increase of the axial FOV would help to improve the image quality of the dedicated system. Nevertheless, the cost will increase. Nevertheless, this system is still working and ready to be used with more patients. We expect to improve patient co-registration and the data storage capabilities to palliate the aforementioned problems.

The other clinical project described in this thesis refers to a heart PET, a national project named CardioPET. The system aimed to improve the spatial resolution in the heart area, while patient was under stress conditions. A multi-panel PET system was implemented to place the detector modules close to the patient. We have concluded earlier that is mandatory an accurate time resolution because TOF algorithms are essential to palliate the lack of angular information of open PET geometry systems. Therefore, for this project we made use of pixelated crystal arrays coupled 1 to 1 to SiPM. Detector panels were composed by 4 × 6 blocks, each of 8 × 8 elements of 3 × 3 × 10 mm^3 LYSO scintillator crystals polished and treated with ESR material. SiPM of 3 × 3 mm^2 were utilized. In this prototype, we have not access to the DOI information but reached a CTR timing resolution of 238 ps. Also, the crystal size was reduced in comparison with the prostate-dedicated PET from 15 mm to 10 mm, enhancing the time resolution, at the cost of some system sensitivity. However, energy resolution was improved to 11%. A PET with 4 panels was built and tested. In the first simulation tests, two panels were separated 28 cm whereas the other two 38 cm, see Figure 58.

The two PET panels were modelled with simulations and experimentally built. We tested the NEMA protocol. The experimental sensitivity varies as expected as the sodium source moves along the axis that join both panels. Nevertheless, the simulated sensitivity exceeds the experimental values, as it happens in all studied prototypes. This might happen, most likely, due the lack of some data bandwidth limitations in the experimental case not considered properly during the simulations. Spatial resolution was estimated with the same source that we have employed for the sensitivity part, this time moving it in the radial Y axis. With 10 iterations, we have reproduced the elongation of the source in the simulation, resulting in a radial spatial resolution below 2 mm for all the Y axis. However, the performance for the transaxial X axis worsens the resolution to 5 mm. We also evaluated the NECR rates, simulated and experimentally, with the two panels. Once again, even that the curves reproduce a similar behavior, simulated values exceed the experimental estimation.

Another challenge in this project was the implementation of a motion tracking system. We employed the MAF techniques for this task. A 16 Megapixels optical camera was installed 1 meter above the scanner. Two ARUCO markers, with 6 × 6 pixels each, were used to register their space coordinates every 0.1 seconds, achieving spatial resolutions below 1 mm. This motion information was included in the MAF algorithm during the reconstruction process so that every time a movement was registered a different LM file was generated. Each LM file is a different frame so at the end of the process all the frames are corrected considering the camera motion output. The camera and MAF algorithm were tested with sources moving at different

speeds. In general, we found good results, but as the speed increases the camera is less accurate to track the motion and the spatial resolution worsens.

In this thesis we have also extensively worked in a pre-clinical system in a collaboration with the University of Virginia [132]. Monolithic crystals present some advantages over pixelated configuration. We have studied a PET configuration to increase the sensitivity and a spatial resolution of a PET scanner for mice imaging based on single annular LYSO block. Several simulation and experimental tests were carried out with such pre-clinical PET design. This scanner had similar dimensions than the Albira PET system commercialized by Bruker, but the novelty relies in the single monolithic block with cylindrical shape and, thus, there are not gaps between detector modules. With this premise, two different prototypes were proposed and tested (both from the simulation and experimental point of view). The first one has a small axial FOV extension, and the scanner external surface was facetted. The idea of this design is to easily integrate existing SiPM array technology. This prototype had all their surfaces black painted, with the exception of the facets where the SiPM were coupled. In order to avoid light truncation and to improve impact detectability, consecutive SiPM arrays were read for each impact. Even that CoG algorithms show no truncation in the transaxial axis, the registered light distributions showed residual tales caused by the facet junctions (change of angle). The smaller aperture of the scanner and the particular crystal geometry made mandatory a good DOI resolution. The spatial resolution was determined around 1.3 mm on average with a spherical source. NECR rates were found similar both in the simulations and experimental data. An experimental NECR peak at 0.3 mCi with almost 50 kcps.

A second edgeless prototype has been recently built and tested, with the aim to eliminate the irregular scintillation light distributions [131]. Herein, the gamma ray exit surface was cylindrical (no facets). This prototype is expected to be used for preclinical research and further experimental characterization. Still the energy performance showed a DOI dependency, that is calibrated. We simulated a small spherical source (0.25 mm diameter) moving across the radial axis, and we have measured the total counts that fit in the 30% photopeak. The normalization map was obtained by simulating a solid cylinder filled with ^{18}F. Setting a voxel dimensions of 0.5 × 0.5 × 0.5 mm^3, with 10 iterations using the MLEM algorithm, the radial spatial resolution at the CFOV converges to 0.6 mm. The lack of gaps between detectors, and the energy calibration according to DOI information, allows the system to reach a spatial resolution close to the positron range. Parallax error correction results in a system spatial resolution below 2 mm for all the transaxial FOV. The main disadvantage of this system is the pileup generated by measuring multiple SiPM arrays at the same time. This effect worsens for high activities.

Therefore, the maximum NECR value, for a 30% energy window, was found at 100 µCi. Notice nevertheless that this value is comparable to other pre-clinical scanners. It would be mandatory to study this pile-up effect for fully cylindrical clinical scanners to evaluate the data loss.

As a summary of performance, we would like to show a comparison of the performance of the clinical prototypes CardioPET (only 2 panels) and PROSPET3 with other scanners and a WB-PET [140]; a brain PET-Hat system [138], the heart Attrium PET [66], and the breast PET scanner MAMMI [139].

PET Scanners	Dimensions (mm^3)	Spatial Resolution cFOV (mm)	Sensitivity (%)
PROSPET3	410 × 410 × 50	1.7	1.50
CardioPET (2P)	280 × 100 × 150	1.5	0.70
Attrius PET	780 × 780 × 123.6	5.8	5.40
Mammi	170 × 170 × 40	1.8	1.00
WB-PET	Multiple Organs	5.0	≈ 1.00

6. CONCLUSIONS

Molecular imaging techniques can map biomarkers distribution within the human body, differently from anatomical images provided by Magnetic Resonance or Computed Tomography. This feature makes the molecular imaging techniques very useful for the medical diagnostic and therapy assessment. Among the rest of molecular imaging techniques, PET presents advantages such as a higher sensitivity and specificity. Nevertheless, PET systems are, in general, more expensive than SPECT scanners so many hospitals cannot afford them. Reducing the total number of detectors is one way to decrease the total cost. Organ-dedicated PET scanners are implemented using a smaller number of detectors and placed closer to the patient body or organ under study. Therefore, the sensitivity is preserved or improved, reducing moreover production cost, when compared to Whole-Body PET systems. Furthermore, this kind of scanners present other advantages, such as the portability and the reduction of injected dose to the patient, and radiation exposure of the clinical personnel. In order to get the detectors close to the organ, some configurations with different technologies have been simulated and tested.

The prostate PET scanner developed within this thesis, underwent several design iterations. The idea for this project was to implement detectors based on monolithic scintillators, since they exhibit good intrinsic spatial resolution, and the good energy performance achieved due to the retroreflector layer. However, the use of these crystals was not the optimal solution due to the

lack of a time resolution in the range of 200-300 ps. After two conceptual designs based on PET panels without TOF, the 24 detector modules were arranged in a single ring configuration, reducing as much as possible the diameter of the scanner. Its reduced size and geometry might allow one to perform in vivo biopsies guided using molecular imaging. Regarding sensitivity and NECR studies, we have noticed a remarkable difference between the simulated and experimental data. Most likely, the acquisition system of the prototype should be improved in future iterations to minimize some data losses. The study we carried out with a patient, was affected by radiation that comes outside the FOV. Nevertheless, in terms of spatial and contrast recovery we have registered very promising results using phantoms.

Pixelated crystal arrays show a better performance in terms of time resolution, which is mandatory for TOF algorithms, so we made use of this kind of crystals coupled 1 to 1 with SiPM for the CardioPET prototype. By using four panels instead of two, the solid angle permit to mitigate the open ring artifacts even without TOF. The spatial resolution was improved compared to commercial scanners, as well as the sensitivity and the NECR rate. In order to correct the patient motion, a MAF algorithm was implemented and tested with the CardioPET, but also with the PROSPET3 ring configuration. ARUCO markers proved to be a good solution to register the motion with an external optical camera.

We proposed a ring scanner for pre-clinical imaging composed by a single monolithic LYSO detector. Due to the absence of gaps between detectors, this novel geometry allows one to increase the total sensitivity. The typical drawback of monolithic detectors is the light truncation at the edges. However, with the continuous ring, this effect is solved and there exists no compression in the transaxial axis, improving therefore the spatial resolution. The first prototype had planar facets in the external surface of the scintillator. Thus, light distributions were slightly different in comparison with conventional monolithic detectors because some tails are generated due to the joints at the facets. This effect produced some artifacts in the light distributions, challenging the impact identification. A second prototype with ful cylindrical geometry has been recently simulated and experimentally tested. This time, light distributions were more similar to conventional monolithic detectors. The total sensitivity registered in simulations is superior to other pre-clinical scanners. The spatial resolution, obtained after OSEM reconstructions, converges to the physical limit of the positron range. Furthermore, DOI correction allows to preserve a very good spatial resolution within the entire FOV. Nevertheless, reading multiple SiPM arrays at the same time leads to pile-up effects. For this reason, NECR peak was found at 100 uCi, which is lower than other scanners.

Before this thesis research, several organ-dedicated PET systems, mainly brain and breast scanners, were investigated by other groups [66]. We focused our research in the prostate and the heart organs trying to emulate the good performance by the use of novel geometries, such as a multi panel system, and novel technology as the one employed in the pre-clinical design. Organ dedicated PET scanners are in general more economical than WB-PET systems and present some advantages, such as a higher sensitivity and spatial resolutions. However, they present some drawbacks such as the radiation that comes outside the FOV. Nevertheless, introducing new technologies that improves spatial, energy and time resolution, as well as new reconstruction algorithms that can deal with non-conventional geometries, these drawbacks can be palliated.

7. BIBLIOGRAPHY

[1] NEUBAHUER, S.; et al (2014). "*Nuclear medicine and molecular imaging*". Revista Médica Clinica Condes 24(1), pp. 157-168.

[2] OSBORN, E.A.; et al (2014). *"Molecular Imaging: Concepts and Applications in CardioVascular disease"*. Elsevier Inc.

[3] PYSZ, M.A.; et al (2010). "*Molecular Imaging: Current Status and Emergencies Strategies".* Clinical Radiology 65(7): pp. 500-516. DOI: 10.1016/j.crad.2010.03.011.

[4] ABRANTES, A.; et al (2009). "*An insight into tumoral hypoxia: The radiomarkers and clinical applications"*. Oncology Reviews 3(1): pp. 3-18. DOI: 101007/s12156-009-0001-z.

[5] TRUJILLO, J.; et al (2017). *"Generadores de biomarcadores: Una solución para lograr la masificación del PET/CT en Latinoamérica"*. Alasbimm Journal, ISSN: 0717 – 4055.

[6] LUQUE-MICHEL, E.; et al (2019). "*Co-encapsulation of superparamagnetic nanoparticles and doxorubicin in PLGA nanocarriers: Development, characterization and in vitro antitumor efficacy in glioma cells*". European Journal of Pharmaceutics and BioPharmaceutics, Vol. 145, pp. 64-75. DOI:10.1016/j.ejpb.2019.10.1004.

[7] MORITZ, F.K.; HRICAK, S. and LARSON, S.M (2012). "*Molecular imaging for personalized cancer care".* Molecular Oncology Vol. 6, Issue 2, pp. 182 – 195. DOI:10.1016/j.molonc.2012.02.005.

[8] MALOTH, K. and UGRAPPA, S. (2014). "*Radioiosotopes: An overview".* International Journal of Case Reports and Images 5(9), pp. 604–609. DOI: 10.5348/ijcri-201457-RA-10012.

[9] TRUSELL, H.J. (1981). "*Processing of X – Ray Images".* Proceedings of the IEEE, Vol. 69, No. 5, pp. 615-627. DOI 10.1109/PROC.1981.12029.

[10] RUBIN, G.D. (2014). "*Computed Tomography: revolutionizing the practice of medicine for 40 years".* Radiology 273(2 Suppl), pp. 45 – 74. DOI: 10.1148/radiol.14141356.

[11] JAVIDI, B.; et al (2013). "*3D Imaging and visualization: An overview of recent advantages".* 12th Workshop on Information Optics (WIO), pp. 1-3. DOI: 10.1109/WIO.2013.6601236.

[12] SMITH-BINDMAN, R.; et al (2009). *"Radiation Dose Associated with Common Computed Tomography Examinations and the Associated Lifetime Attributable Risk of Cancer".* Archives of Internal Medicine, 169(22), pp. 2078-2086. DOI: 10.1001/archinternmed.2009.427.

[13] JAIN, R. (2011). "*Perfusion CT Imaging of Brain Tumors: An Overview".* American Journal of Neuroradiology, 32 (9), pp. 1570-1577; DOI: https://doi.org/10.3174/ajnr.A2263.

[14] YU, L. (2009). "*Radiation Dose Reduction in Computed Tomography: techniques and future perspective*". Imaging Med. 2009;1(1):65-84. DOI:10.2217/iim.09.5

[15] EDELMAN, R.A. (2014). "*The History of MR Imaging as Seen through the Pages of Radiology".* Radiological Society of North America Radiology 273(2 Suppl), pp. 181-200. DOI: 10.1148/radiol.14140706.

[16] SUNDARAM, M. and MCLEOD, M. (1990). "*MR imaging of tumor and tumorlike lesions of bone and soft tissue*". American Journal of Roentgenol 155(4), pp. 817-824. DOI: 10.2214/ajr.155.4.2119115. PMID: 2119115.

[17] SCHENK, J.F.; et al (1995). "*Superconducting Open-Configuration MR Imaging System for Image-guided Therapy".* Radiology; 195: pp. 805-814. DOI: 10.1148/radiology.195.3.7754014.

[18] TAKAHASHI, M.; UEMATSU, H. and HATABU, H. (2003). "*MR imaging at high magnetic fields".* European Journal of Radiology, Vol. 46, Issue 1, pp. 45-52.

[19] MATTHEW, M. and DOIRON, A. (2018). "*Gold Nanoparticles as X-Ray, CT, and Multimodal Imaging Contrast Agents: Formulation, Targeting, and Methodology".* Advanced Nanomaterials for Biological Applications. DOI: https://doi.org/10.1155/2018/5837276.

[20] DONG XIAO, Y.; et al (2016). *"MRI contrast agents: Classification and application"*. International Journal of Molecular Medicine. Vol. 38 Issue 5. DOI: 10.3892/ijmm.2016.2744.

[21] PERERA PINTADO, A.; et al (2017). *"SPECT/CT: main applications in nuclear medicine".* Nucleus, No.62.

[22] MAGDY, M.K.; et al (2011). "*Molecular SPECT Imaging: An Overview".* International Journal of Molecular Imaging, Article ID 796025. DOI: 10.1155/2011/796025.

[23] ADAK, S.; et al (2012). "*Radiotracers for SPECT imaging: current scenario and future prospects*". Radiochimica Acta 100, pp. 95-107. DOI: 10.1524/ract.2011.1891.

[24] MADSEN, M.T. (2007). "*Recent Advances in SPECT Imaging*". Journal of Nuclear Medicine; 48(4), pp. 661-673. DOI: 10.2967/jnumed.106.032680.

[25] www.nist.gov

[26] LIU, C.; et al (2015). *"A performance comparison of novel cadmium-zinc-telluride camera and conventional SPECT/CT using anthropomorphic torso phantom and water bags to simulate soft tissue and breast attenuation".* Annals of Nuclear Medicine. 29(4): pp. 342-350. DOI: 10.1007/s12149-015-0952-z.

[27] VAN AUDENHAEGE, K.; et al (2015). "*Review of SPECT collimator selection, optimization, and fabrication for clinical and preclinical imaging*". Medical Physics, 42(8), pp. 4796–4813. DOI: 10.1118/1.4927061.

[28] HUTTON, B.F. (2014). "*The origins of SPECT and SPECT/CT".* European Journal of Nuclear Medicine and Molecular Imaging. 41 Suppl 1, pp. 3-16. DOI: 10.1007/s00259-013-2606-5.

[29] LIMA, R.F.; et al (2003). "*Incremental value of combined perfusion and function over perfusion alone by gated SPECT myocardial perfusion imaging for detection of severe three-vessel coronary artery disease*". Journal of the American College of Cardiology Vol. 42, Issue 1, pp. 64-70. DOI: 10.1016/s0735-1097(03)00562-x.

[30] SILVERMAN, D. (2004). *"Brain 18F-FDG PET in the Diagnosis of Neurodegenerative Dementias: Comparison with Perfusion SPECT and with Clinical Evaluations Lacking Nuclear Imaging".* Journal of Nuclear Imaging, 45, pp. 594–607.

[31] GENC, A. (2016). *"Ultrasound imaging in the general practitioner's office – a literature review".* Journal of Ultrasonography, 16(64), pp. 78–86.

[32] KROPOTOV, J.D. (2016). "*Chapter 1.4 - Positron Emission Tomography".* Functional Neuromarkers for Psychiatry. Applications for Diagnosis and Treatment, pp. 27 – 30.

[33] STAUSS; J.; et al (2008). "*Guidelines for 18F-FDG PET and PET-CT imaging in pediatric oncology".* European Journal of Nuclear Medicine and Molecular Imaging, 35(8), pp. 1581-1588. DOI: 10.1007/s00259-008-0826-x.

[34] GRASSI, I.; et al (2015). "*The clinical use of PET with ^{11}C – acetate".* American Journal of Nuclear Medicine and Molecular Imaging, 2(1), pp. 33-47.

[35] JODAL, L.; LOIREC, C. and CHAMPION, C. (2014). "*Positron range in PET imaging: non-conventional isotopes*". Physics in Medicine and Biology, IOP Publishing, 59, pp. 7419 - 7434. DOI: 10.1088/0031-9155/59/23/7419.

[36] RAHMIM, A. and ZAIDI, H. (2008). "*PET versus SPECT: strengths, limitations and challenges".* Nuclear Medicine Communications, 29, pp. 193–207. DOI: 10.1097/MNM.0b013e3282f3a515.

[37] CHENG, D.; et al (2010). "*A comparison of 18F PET and 99mTc SPECT imaging in phantoms and in tumored mice*". Bioconjugate Chemistry, 21(8), pp. 1565–1570. DOI: 10.1021/bc1001467.

[38] SHUKLA, A.K.; KUMAR, U. (2006). "*Positron emisión tomography: An overview".* Journal of Medical Physics. 31(1), pp. 13–21. DOI: 10.4103/0971-6203.25665.

[39] BAILEY, D. L. and MEIKLE S.R. (1994). "*A convolution-subtraction scatter correction method for 3D PET*". Physics in Medicine and Biology, 39, 411. DOI: 10.1088/0031-9155/39/3/009.

[40] BRASSE, D.; et al (2005). "*Correction Methods for Random Coincidences in Fully 3D Whole-Body PET: Impact on Data and Image Quality*". Journal of Nuclear Medicine; 46, pp. 859 – 867.

[41] MELCHER, C.L. (2000). "*Scintillation Crystals for PET"*. Journal of Nuclear Medicine; 41, pp. 1051-1055.

[42] ODDSTIG, J.; et al (2019). "*Comparison of conventional and Si-photomultiplier-based PET systems for image quality and diagnostic performance"*. BioMed Central Medical Imaging 19, Article Number: 81.

[43] NAGARKAR, V.V.; et al (2004). "*A High Efficiency Pixelated Detector for Small Animal PET*". IEEE Transactions on Nuclear Science, 51(3). DOI: 10.1109/TNS.2004.829750.

[44] CHERRY, S.R.; et al (2012). "*Physics in Nuclear Medicine".* Book, 4th Edition.

[45] FEDOROV, A.; KORZHIK, M. and PANOV, V. (2005). "*Double-end readout of Lu-based scintillation pixels in Positron Emission Tomography*". Nuclear Instruments and Methods in Physics Research Section A. Accelerators Spectrometers Detectors and Associated Equipment 537(1), pp. 331-334.

[46] MARCINKOWSKY, R.; et al. (2012). "*Performance of Digital Silicon Photomultipliers for Time-of-Flight PET scanners".* IEEE Nuclear Science Symposium Conference Record. DOI: 10.1109/NSSMIC.2012.6551644.

[47] GONZALEZ, A.J.; et al (2016). *"A PET Design Based on SiPM and Monolithic LYSO Crystals: Performance Evaluation".* IEEE Transactions on Nuclear Science, Vol. 63, No. 5, pp. 2471-2477, DOI: 10.1109/TNS.2016.2522179.

[48] GONZALEZ-MONTORO, A.; et al (2018). "*Detector block performance based on a monolithic LYSO crystal using a novel signal multiplexing method"*. Nuclear Instruments and Methods in Physics Research Section A: Accelerators, Spectrometers, Detectors and Associated Equipment. Vol. 912, pp. 372 – 377.

[49] LAMPROU, E.; et al (2020). "*Exploring TOF capabilities of PET detector blocks based on large monolithic crystals and analog SiPMs*". European Journal of Medical Physics. Vol. 70, pp. 10-18.

[50] GONZALEZ-MONTORO, A.; et al (2019). "*Novel method to measure the intrinsic spatial resolution in PET detectors based on monolithic crystals*". Nuclear Instruments and Methods in Physics Research Section A, Vol. 920, pp. 58-67.

[51] MOHAMMADI, I.; et al (2019). "*Minimization of parallax error in positron emission tomography using depth of interaction capable detectors: methods and apparatus*". Biomedical Physics and Engineering Express 5 062001.

[52] LEWELLEN, T.K.; MIYAOKA, R.S. and KOHLMYER, S.G. (1992). "*Improving the performance of the SP-3000 PET detector modules*". IEEE Transactions on Nuclear Science, Vol. 39, No. 4, pp. 1074-1078. DOI: 10.1109/23.159762.

[53] GONZALEZ-MONTORO, A.; et al (2021). *"Evolution of PET Detectors and Event Positioning Algorithms Using Monolithic Scintillation Crystals*". IEEE Transactions on Radiation and Plasma Medical Sciences, Vol. 5, No. 3, pp. 282-305. DOI: 10.1109/TRPMS.2021.3059181.

[54] GONZALEZ-MONTORO, A.; et al (2017). "*Performance Study of a Large Monolithic LYSO PET Detector With Accurate Photon DOI Using Retroreflector Layers*". IEEE Transactions on Radiation and Plasma Medical Sciences, Vol. 1, No. 3, pp. 229-237. DOI: 10.1109/TRPMS.2017.2692819.

[55] SANCHEZ, F.; et al (2013). "*ALBIRA: a small animal PET/SPECT/CT imaging system*". Medical Physics 40(5):051906. DOI: 10.1118/1.4800798.

[56] GSELL, W.; et al (2020). "Characterization of a preclinical PET insert in a 7 tesla MRI scanner: beyond NEMA testing". Physics in Medicine and Biology 65(24):245016. DOI: 10.1088/1361-6560/aba08c.

[57] GAUDIN, É.; et al (2021). "*Performance evaluation of the mouse version of the LabPET II PET scanner*". Physics in Medicine and Biology 66(6):065019.

[58] BRIX, G.; et al (1997). "*Performance evaluation of a whole-body PET scanner using the NEMA protocol. National Electrical Manufacturers Association".* Journal of Nuclear Medicine 38(10), pp. 1614-1623. DOI: 10.1088/1361-6560/abd952.

[59] WERNER, M.K.; SCHMIDT, H. and SCHWENZER, N. (2012). "*MR/PET: A New Challenge in Hybrid Imaging".* American Journal of Roentgenology, 199, pp. 272-277. DOI: 10.2214/AJR.12.8724.

[60] AMBROSINI, V.; et al (2012). "*PET/CT imaging in different types of lung cancer: An overview*". European Journey of Radiology. Vol. 81, Issue 5, pp. 988-1001. DOI: 10.1016/j.ejrad.2011.03.020.

[61] KINAHAN, P.E.; et al (1998). "*Attenuation correction for a combined 3D PET/CT scanner".* Medical Physics 25. DOI: 10.1118/1.598392.

[62] SHAH, J. (2018). "*Hybrid MR-PET Imaging. Systems, Methods and Applications*". Royal Society of Chemistry.

[63] LUCAS, A.J.; et al (2006). "*Development of a combined microPET-MR system*". Technology in Cancer Research and Treatment 5(4), pp. 337-341. DOI: 10.1177/153303460600500405.

[64] Del Guerra, A.; et al (2011). "*Silicon Photomultipliers (SiPM) as novel photodetectors for PET*". Nuclear Instruments and Methods in Physics Research Section A 648, pp. 232-235. DOI:10.1016/j.nima.2010.11.128.

[65] KARLBERG, A.M.; et al (2016). "*Quantitative comparison of PET performance—Siemens Biograph mCT and mMR*". European Journal of Nuclear Medicine and Molecular Imaging, Physics. 3: 5. DOI: 10.1186/s40658-016-0142-7.

[66] GONZALEZ, A. J.; et al (2018). "*Organ-Dedicated Molecular Imaging Systems*". IEEE Transactions on Radiation and Plasma Medical Sciences, vol. 2, no. 5, pp. 388-403. DOI: 10.1109/TRPMS.2018.2846745.

[67] LI, M.; YOCKEY, B. and ABBASZADEH, S. (2020). "*Design Study of a Dedicated Head and Neck Cancer PET System*". IEEE Transaction on Radiation and Plasma Medical Sciences, Vol. 4, No. 4.

[68] PENG, H. and LEVIN, C. (2010). "*Design study of a high-resolution breast-dedicated PET system built from cadmium zinc telluride detectors*". Physics in Medicine and Biology 55(9), pp. 2761–2788. DOI: 10.1088/0031-9155/55/9/022.

[69] SURTI, S. and KARP, J. (2016). *"Advances in time-of-flight PET".* Physica Medica: PM: an International Journal Devoted to the Applications of Physics to Medicine and Biology: Official Journal of the Italian Association of Biomedical Physics (AIFB), 32(1), pp. 12-22. DOI: 10.1016/j.ejmp.2015.12.007.

[70] AHMED, A.M.; TASHIMA, H. and YAMAYA T. (2018). "*Investigation of spatial resolution improvement by use of a mouth-insert detector in the helmet PET scanner*". Radiological Physics and Technology Vol. 11, pp. 7–12. DOI: 10.1007/s12194-017-0425-2.

[71] TASHIMA, H. and YAMAYA T. (2016). "*Proposed helmet PET geometries with add-on detectors for high sensitivity brain imaging*". Physics in Medicine and Biology 61(19), pp. 7205-7220. DOI:10.1088/0031-9155/61/19/7205.

[72] MICHELLE, C.; et al (2004). "*Properties of LYSO and recent LSO scintillators for phoswich PET* detectors". IEEE Transactions on Nuclear Science, Vol. 51, No. 3, pp. 789-795. DOI: 10.1109/TNS.2004.829781.

[73] LECOQ, P. (2017). *"Pushing the Limits in Time-of-Flight PET Imaging*". IEEE Transactions on Radiation and Plasma Medical Sciences, Vol. 1, No. 6, pp. 473-485. DOI: 10.1109/TRPMS.2017.2756674.

[74] https://eljentechnology.com/products/plastic-scintillators/ej-232-ej-232q

[75] KONSTANTINOU, G. (2022). "*Metascintillators for Ultrafast Gamma Detectors: A Review of Current State and Future* Perspectives". IEEE Transactions on Radiation and Plasma Medical Sciences, Vol. 6, No. 1, pp. 5-15. DOI: 10.1109/TRPMS.2021.3069624.

[76] AGOSTINELLI, S.; et al (2003). "*Geant4—a simulation toolkit*". Nuclear Instruments and Methods in Physics Research Section A: Accelerators, Spectrometers, Detectors and Associated Equipment, Vol. 506, Issue 3, pp. 250 – 303.

[77] JAN, S.; et al (2004). "*GATE: a simulation toolkit for PET and SPECT*". Physics in Medicine and Biology 49(19), pp. 4543-4561. DOI: 10.1088/0031-9155/49/19/007.

[78] KOMAROV, S.A.; et al (2010). "Compton Scattering in Clinical PET/CT With High Resolution Half Ring PET Insert Device". IEEE Transactions on Nuclear Science 57(3), pp. 1045–1051. DOI: 10.1109/TNS.2010.2046754.

[79] GATE Users Guide v8.0. Available in http://www.opengatecollaboration.org/

[80] HERRAIZ, V.E.; et al (2013). "*Improved dead-time correction for PET scanners: application to small-animal PET".* Physics in Medicine and Biology 58, pp. 2059- 2072. DOI: 10.1088/0031-9155/58/7/2059.

[81] GERMANO, G. and HOFFMAN E. (1990). "*A study of data loss and mispositioning due to pileup in 2-D detectors* in PET". IEEE Transactions on Nuclear Science, Vol. 37, No. 2, pp. 671-675, DOI: 10.1109/23.106696.

[82] https://www.crystals.saint-gobain.com/sites/imdf.crystals.com/files/documents/bgo-material-data-sheet.pdf

[83] https://www.crystals.saint-gobain.com/sites/imdf.crystals.com/files/documents/lyso-material-data-sheet.pdf

[84] https://www.crystals.saint-gobain.com/sites/hps-mac3-cma-crystals/files/2021-10/BC490-Data-Sheet.pdf

[85] https://www.hamamatsu.com/resources/pdf/ssd/s13361-3050_series_kapd1054e.pdf

[86] GUNDACKER, S.; et al (2020). "*Experimental time resolution limits of modern SiPMs and TOF-PET detectors exploring different scintillators and Cherenkov emission".* Physics in Medicine and Biology 65 025001. DOI: 10.1088/1361-6560/ab63b4.

[87] TAO, L.; et al (2020). "*Deep learning based methods for gamma ray interaction location estimation in monolithic scintillation crystal detectors*". Physics in Medicine and Biology 65 115007. DOI: 10.1088/1361-6560/ab857a.

[88] TONG, S.; ALESSIO, A. and KINAHAN, P. (2010). "*Image reconstruction for PET/CT scanners: past achievements and future challenges*". Imaging in Medicine 2(5), pp. 529–545. DOI: 10.2217/iim.10.49.

[89] DEFRISE, M.; KINAHAN, P. and MICHEL, C. (2005). "*Image Reconstruction Algorithms in PET".* In book: Positron Emission Tomography, pp.63-91.

[90] PRATX, G.; et al (2006). "*Fully 3-D List-Mode OSEM Accelerated by Graphics Processing* Units". 2006 IEEE Nuclear Science Symposium Conference Record, pp. 2196-2202, DOI: 10.1109/NSSMIC.2006.354350.

[91] FAHEY, F.H. (2002). "*Data acquisition in PET imaging*". Journal of Nuclear Medicine Technology 30(2), pp. 39-49.

[92] REINDERS, A.T.S.; et al (2002). "*Iterative versus filtered backprojection reconstruction for statistical parametric mapping of PET activation measurements: a comparative case study*". Neuroimage. 15(1), pp. 175-81. DOI: 10.1006/nimg.2001.0963.

[93] ORTUÑO, J.E. (2008). "*Reconstrucción de Imágenes de Tomografía por Emisión de Positrones de Alta Resolución mediante Métodos Estadísticos"*. Doctoral thesis. Escuela Técnica Superior de Ingenieros de Telecomunicación, Universidad Politécnica de Madrid.

[94] SLOMSKI, A.; et al (2014). "*3D PET image reconstruction based on Maximum Likelihood Estimation Method (MLEM) algorithm*". Bio-Algorithms and Med-Systems 10(1), pp. 1-7. DOI: 10.1515/bams-2013-0106.

[95] ORTUÑO, J.M.; et al (2006). "*3D-OSEM iterative image reconstruction for high-resolution PET using precalculated system matrix*". Nuclear Instruments and Methods in Physics Research A 569, pp. 440–444.

[96] MERLIN, T.; et al (2018). "*CASToR: a generic data organization and processing code framework for multi-modal and multi-dimensional tomographic reconstruction*". Physics in Medicine and Biology 63(18):185005. DOI: 10.1088/1361-6560/aadac1.

[97] CHANG Y.; et al (2018). "*Plant-Specific Modular PET: Data Processing with CASToR and Performance Evaluation*". IEEE Nuclear Science Symposium and Medical Imaging Conference Proceedings (NSS/MIC), pp. 1-3. DOI: 10.1109/NSSMIC.2018.8824574.

[98] SALVADORI, J.; et al (2020). *"Monte Carlo simulation of digital photon counting PET".* European Journal of Nuclear Medicine and Molecular Imaging, Physics 7:23. DOI: https://doi.org/10.1186/s40658-020-00288-w.

[99] RANKINE, L.J.; WILSON, J. and TURKINGTON, T. (2012). "*Investigation of four phantoms for PET normalization*". 2012 IEEE Nuclear Science Symposium and Medical Imaging Conference Record (NSS/MIC), pp. 3548-3550. DOI: 10.1109/NSSMIC.2012.6551812.

[100] CHEN, Y. and AN, K. (2017). *"Attenuation Correction of PET/MR Imaging"*. Magnetic Resonance Imaging Clinics of North America, 25(2), pp. 245–255. DOI: 10.1016/j.mric.2016.12.001.

[101] RATIB, O.; et al (2010). "*Whole Body PET-MRI scanner: First experience in oncology"*. Journal of Nuclear Medicine, 51.

[102] LERCHER, M.J. and WIENHARD, K. (1994). "*Scatter correction in 3-D PET*". IEEE Transactions on Medical Imaging, 13(4), pp. 649-57. DOI: 10.1109/42.363103.

[103] BRASSE, D.; et al (2005). "*Correction Methods for Random Coincidences in Fully 3D Whole-Body PET: Impact on Data and Image Quality*". Journal of Nuclear Medicine 46, pp. 859 – 867.

[104] VANDENBERGUE, S.; et al (2016). "*Recent developments in time-of-flight PET*". European Journal of Nuclear Medicine and Molecular Imaging, Physics 3:3. DOI: 10.1186/s40658-016-0138-3.

[105] JAKOBY, B.W.; et al (2011). "*Physical and clinical performance of the mCT time-of-flight* PET/CT scanner". Physics in Medicine and Biology 56(8), pp. 2375-2389. DOI: 10.1088/0031-9155/56/8/004.

[106] NEMA NU 2 2012. Performance Measurements of Positron Emission Tomographs (PET). Published by: National Electrical Manufacturers Association.

[107] NEMA Standards Publication Nu 4 – 2008. *Performance Measurements of Small Animal Positron Emission Tomographs.* Published by: National Electrical Manufacturers Association.

[108] NEMA Standards Publication NU 2 – 2001. *Performance Measurements of Positron Emission Tomographs.* Published by: National Electrical Manufacturers Association.

[109] NEMA Standards Publication NU 2-2018. *Performance Measurements of Positron Emission Tomographs (PET).* Published by: National Electrical Manufacturers Association.

[110] MEIKLE, S.R.B. (2005). "*Quantitative Techniques in PET*". In: Bailey D.L., Townsend D.W., Valk P.E., Maisey M.N. (eds) Positron Emission Tomography. Springer, London. https://doi.org/10.1007/1-84628-007-9_5.

[111] http://www.gco.iarc.fr/today/ datasources-methods.

[112] SMITH, J.A.; et al (1997). *"Transrectal ultrasound versus digital rectal examination for the staging of carcinoma of the prostate: results of a prospective multi-institutional trial".* Journal of Urology, 157(3):902. DOI: 10.1016/S0022-5347(01)65079-1.

[113] SMEENGE, M.; et al (2012). *"Role of transrectal ultrasonography (TRUS) in focal therapy of prostate cancer: report from a consensus panel".* BJU International, pp. 110–942.

[114] GARZÓN GARCÍA, J.R.; et al (2018). *"68Ga-PSMA PET/CT in prostate cancer".* Revista Española de Medicina Nuclear e Imagen Molecular (English Edition). Vol 37. No. 2, pp. 130–138. DOI: 10.1016/j.remn.2017.07.004.

[115] CAÑIZARES, G.; et al (2020). "*Pilot performance of a dedicated prostate PET suitable for diagnosis and biopsy guidance".* European Journal of Nuclear Medicine and Molecular Imaging, Physics 7, 38. DOI: https://doi.org/10.1186/s40658-020-00305-y.

[116] SURTI, S.; et al *(2007). "Performance of Philips Gemini TF PET/CT Scanner with Special Consideration for Its Time-of-Flight Imaging Capabilities*". Journal of Nuclear Medicine, 48 (3), pp. 471-480.

[117] LAMPROU, E.; et al (2021). "Development and Performance Evaluation of High Resolution TOFPET Detectors Suitable for Novel PET Scanners". Doctoral Thesis in Universidad Politécnica de Valencia.

[118] LAMPROU, E.; et al (2020). *"PET Detector Block with Accurate 4D Capabilities".* Nuclear Instruments and Methods in Physics Research Section A 912: pp. 132-136. DOI: https://doi.org/10.1016/j.nima.2017.11.002.

[119] LAMPROU, E.; et al (2020). *"In-depth evaluation of TOF-PET detectors based on crystal arrays and the TOFPET2 ASIC".* Nuclear Instruments and Methods in Physics Research Section A Vol. 977, 164295. DOI: https://doi.org/10.1016/j.nima.2020.164295.

[120] ULLISCH, M.G.; et al (2012). "*MR-Based PET Motion Correction Procedure for Simultaneous MR-PET Neuroimaging of Human Brain*". PLOS ONE 7(11): e48149. DOI: 10.1371/journal.pone.0048149.

[121] MANBER, R.; et al (2016). "*Joint PET – MR respiratory motion models for clinical PET motion correction".* Physics in Medicine and Biology. 61(17): pp. 6515-6530. DOI:10.1088/0031-9155/61/17/6515.

[122] ROMERO-RAMIREZ, F.J.; MUÑOZ-SALINAS, R. and MEDINA-CARNICER, R. (2018). "*Speeded up detection of squared fiducial markers*". Image and Vision Computing, Vol. 76, pp. 38-47, ISSN 0262-8856. https://doi.org/10.1016/j.imavis.2018.05.004.

[123] ZHOU, W.V.; et al (2009). "Compensation for lost events in LOR rebinning motion correction for PET"). IEEE Nuclear Science Symposium Conference Record (NSS/MIC), pp. 3140-3145.

[124] PICARD, Y and THOMPSON, C.J. (1997). *"Motion correction of PET images using multile acquisition frames*". IEEE Transactions on Medical Imaging, Vol. 16, pp. 137-144. DOI: 10.1109/42.563659.

[125] KYME, A.Z.; et al (2011). "*Optimized motion tracking for Positron Emission Tomography Studies of Brain Function in Awake Rats".* PLOS ONE 6(7): e21727. DOI:10.1371/journal.pone.0021727.

[126] ESPINÓS, H.; et al (2021). "*Simulation Study of a Frame-Based Motion Correction Algorithm for Positron Emission Imaging".* Sensors (Basel); 21(8): 2608. DOI: 10.3390/s21082608.

[127] CRESSON, L.F.; et al (2007). "*List-mode based reconstruction for respiratory motion correction in PET using non-rigid body transformations*". Physics in Medicine and Biology Vol.52, Issue 17, pp. 5187-5204. DOI: 10.1088/0031-9155/52/17/006.

[128] CAÑIZARES, G. (2019). "*Motion Correction of Multi-Frame PET Data*". IEEE Nuclear Science Symposium and Medical Imaging Conference (NSS/MIC), pp. 1-4. DOI: 10.1109/NSS/MIC42101.2019.9059930

[129] GONZALEZ-MONTORO, A.; et al (2017). "*Highly improved operation of monolithic BGO-PET blocks".* Journal of Instrumentation 12(11):C11027-C11027. DOI:10.1088/1748-0221/12/11/C11027.

[130] CHENG, J.C. and LAFOREST, R. (*2013). "Using ITK to obtain motion transform in anatomically guided PET motion correction for simultaneous PET/MR".* IEEE Nuclear Science Symposium and Medical Imaging Conference (NSS/MIC), pp. 1-5. DOI: 10.1109/NSSMIC.2013.6829252.

[131] FREIRE, M.; et al (2021). "*Experimental validation of a rodent PET scanner prototype based on a single LYSO crystal tube"*. IEEE Transactions on Radiation and Plasma Medical. DOI: 10.1109/TRPMS.2021.3124448.

[132] GONZÁLEZ, A.J.; et al (2018). *"Feasibility study of a small animal PET insert based on a single LYSO monolithic tube"*. Frontiers in Medicine 328.

[133] GENNA, S. and SMITH, A.P. (1988). "The development of ASPECT, an annular single crystal brain camera for high efficiency SPECT". IEEE Transactions on Nuclear Science, Vol. 35, No. 1, pp. 654-658, DOI: 10.1109/23.12806.

[134] WILSON, K.J.; et al (2019). "*Localization of the Lines of Response in a Continuous Cylindrical Shell PET Scanner".* Annual International Conference of the IEEE Engineering in Medicine and Biology Society. IEEE Engineering in Medicine and Biology Society, pp. 4844-4850. DOI: 10.1109/EMBC.2019.8856676.

[135] XU, J.; et al (2019). *"A preclinical PET detector constructed with a monolithic scintillator ring".* Physics in Medicine and Biology 64 155009. DOI: 10.1088/1361-6560/ab2ca4.

[136] STOLIN, A.; et al (2017). *"Preclinical positron emission tomography scanner based on a monolithic annulus of scintillator: initial design study".* Journal of Medical Imaging 4(1): 011007.DOI: 10.1117/1.JMI.4.1.011007.

[137] CAI, I.P.; ZHOU, W.P. and TANG, J. (2018). *"Growth Method Research of LYSO: Ce Single Crystal"*. Proceedings of the International Workshop on Materials, Chemistry and Engineering, pp. 685-689. ISBN: 978-989-758-346-9.

[138] YAMAMOTO, S.; et al (2011). *"Development of a brain PET system, PET-Hat: A wearable PET system for brain research"*. IEEE Transactions on Nuclear Science, Vol. 58, No. 3, pp. 668–673.

[139] MOLINER, L.; et al (2012). *"Design and evaluation of the MAMMI dedicated breast PET"*. Medical Physics, Vol. 39, No. 9, pp. 5393–5404.

[140] VANDENBERGUE, S.; MOSKAL, P. and KARP, J.S. (2020). *"State of the art in total body PET".* European Journal of Nuclear Medicine and Molecular Imaging, Physics 7:35. DOI: https://doi.org/10.1186/s40658-020-00290-2.

8. CONTRIBUTIONS

8.1. Peer-Reviewed papers:

a) CAÑIZARES, G.; et al (2020). "*Pilot Performance of a dedicated prostate PET suitable for diagnosis and biopsy guidance*". European Journal of Nuclear Medicine and Molecular Imaging, Physics 7 (1), 38. https://doi.org/10.1186/s40658-020-00305-y.

b) FREIRE, M.; et al (2021). "*Reducing Calibration Time in PET Systems Based on Monolithic Crystals*". Frontiers in Medicine, Vol. 8. DOI: 10.3389/fmed.2021.734476.

c) FREIRE, M.; et al (2021). "*Experimental validation of a rodent PET scanner prototype based on a single LYSO crystal tube"*. IEEE Transactions on Radiation and Plasma Medical Sciences. DOI: 10.1109/TRPMS.2021.3124448.

d) GONZÁLEZ-MONTORO, A.; et al (2019). *"Novel Method to measure the intrinsic spatial resolution in PET detector based on monolithic crystals"*. Nuclear Instruments and Methods in Physics Research, Section A 920, pp. 58-67. https://doi.org/10.1016/j.nima.2018.12.056.

e) MOLINER, L.; et al (2019). *"TOF studies for dedicated PET with open geometries"*. Journal of Instrumentation Vol.14. https://doi.org/10.1088/1748-0221/14/02/C02006.

f) LAMPROU, E.; et al (2020). *"PET detector block with accurate 4d capabilities"*. Nuclear Instruments and Methods in Physics Research, Section A, Vol.912, pp. 132 –136. https://doi.org/10.1016/j.nima.2017.11.002.

g) GONZÁLEZ, A.J.; et al (2018). *"Feasibility study of a small animal PET insert based on a single LYSO monolithic tube"*. Frontiers in Medicine 5:328. DOI: 10.3389/fmed.2018.00328.

h) GONZÁLEZ, A.J.; et al (2017). *"A scintillator geometry suitable for very small PET gantries"*. Journal of Instrumentation Vol.12. https://doi.org/10.1088/1748-0221/12/12/C12018.

8.2. Conference proceedings:

i) CAÑIZARES, G.; et al (2019). *"Motion Correction of Multi-Frame PET Data"*. IEEE Nuclear Science Symposium and Medical Imaging Conference (NSS/MIC), pp. 1-4.DOI: 10.1109/NSS/MIC42101.2019.9059930.

j) GONZÁLEZ-MONTORO, A.; et al (2017). "*A Method to Measure the Intrinsic Detector Resolution on Monolithic Crystals*". IEEE Nuclear Science Symposium and Medical Imaging Conference (NSS/MIC), pp. 1-3. DOI: 10.1109/NSSMIC.2017.8532948.

k) LAMPROU, E.; et al (2017). "*Progress Report for an Accurate PET Detector Based on SiPMs and the TOFPET ASIC*". IEEE Nuclear Science Symposium and Medical Imaging Conference (NSS/MIC), pp. 1-3. DOI: 10.1109/NSSMIC.2017.8533123.

l) SÁNCHEZ, S.; et al (2017). "*A Direct Ray Tracing Reconstruction Algorithm Using an Adaptive Median Filter*". IEEE Nuclear Science Symposium and Medical Imaging Conference (NSS/MIC), pp. 1-3. DOI: 10.1109/NSSMIC.2017.8533115.

m) AGUILAR, A.; et al (2017). *"Preliminary characterization of ASIC-based detectors for TOF-PET applications"*. 2016 IEEE Nuclear Science Symposium, Medical Imaging Conference and Room –Temperature Semiconductor Detector Workshop (NSS/MIC/RTSD), pp. 1-5.DOI: 10.1109/NSSMIC.2016.8069652.

n) GONZÁLEZ; A.J.; et al (2016). "*A brain PET insert MR compatible: Final design and first results*". 2016 IEEE Nuclear Science Symposium, Medical Imaging Conference and Room –Temperature Semiconductor Detector Workshop (NSS/MIC/RTSD), pp. 1-5. DOI: 10.1109/NSSMIC.2016.8069619.

o) LAMPROU, E.; et al (2018). "*TOF-PET Detectors Based on ASIC Technology and Analog SiPMs"*. 2018 IEEE Nuclear Science Symposium and Medical Imaging Conference (NSS/MIC), pp. 1-4. DOI: 10.1109/NSSMIC.2018.8824517.

8.3. Participation in conferences:

a) AGUILAR, A. (2017). *"Design concept and pilot tests of a dedicated two panels prostate PET"*. XXXVI Biennal Meeting of the Real Sociedad Española de Física. Santiago de Compostela.

b) CAÑIZARES, G. (2018). *"Insert mouse PET, for high–field MR, based on one single monolithic scintillator"*. EANM 2018, Dusseldorf.

c) CAÑIZARES, G. (2019). *"PROSPET: First tests and results"*. 6thCongreso Conjunto 22 SEFM/SEPR17, Burgos.

d) ESPINÓS, H. (2019). *"CARDIO-PET A design study of a cardiac-dedicated PET system"*. MEDAMI, Valencia.

e) CAÑIZARES, G. (2021). *"Pilot Results of Detectors Enhancing TOF and DOI Capabilities, Suitable for TB-PET."* IEEE Nuclear and Plasma Science Society.

This thesis was supported by a FPI grant under 2017-08582 reference in the PhD program: "*Programa de Doctorado en Tecnologías para la Salud y el Bienestar*" belonging to the Polytechnic University of Valencia. The grant was supported by the "*Consejo Superior de Investigaciones Científicas*" together with the "*Agencia Estatal de Investigación*" and the "*Fondo Social Europeo*".